Phase diagrams of bond and site frustrated magnetic material: Experiments and Theory

Alexander D. Beath

Department of Physics

McGill University

Montreal, Québec

CANADA

August 2007

A thesis submitted to

McGill University

in partial fulfillment of the requirements

for the degree of Doctor of Philosophy

Your file Votre référence
ISBN: 978-0-494-50776-6
Our file Notre référence
ISBN: 978-0-494-50776-6

For you, mom (Dec. 27th 1945 – Oct. 16th 2006)

Abstract

We have carried out large scale Monte Carlo simulations of site and bond frustrated Heisenberg models in order to gain insight into experimental phase diagrams on bond and site frustrated magnetic materials. In the case of site frustrated models, we find that spin glass ordering does not take place on either the simple cubic or body-centered cubic lattices which are bipartite. Instead, the model decouples into either one or two percolating clusters of ferromagnetic (antiferromagnetic) sites which order ferromagnetically (antiferromagnetically). The ordering is similar to the situation which exists when ferromagnetic and antiferromagnetic sites do not interact at all. Including an interaction between ferromagnetic and antiferromagnetic sites, to create frustration, causes the ferromagnetic (FM) and antiferromagnetic (AF) order to become mutually perpendicular while increasing both T_C and T_N. This behaviour is similar to what occurs in our experiments on site frustrated a-$(Fe_{100-x}Mn_x)_{78}Si_8B_{14}$; for this alloy ferromagnetic and *spin glass* order co-exist transverse to one another for $0.17 < x < 0.31$. Geometrical frustration likely plays a significant role in the material since the glass structure cannot support antiferromagnetic order, unlike bipartite lattices. We conjecture that the site frustrated model on the non-bipartite face-centered cubic lattice, which is geometrically frustrated with respect to AF order, produces a spin glass with sufficient randomness and would make a superior model.

In the case of bond frustrated models, we have found that the phase diagram includes *all* of the bulk phases predicted in mean field theory by Gabay and Toulouse over 25 years ago, despite the long held view that Heisenberg spin glasses do not order in three dimensions. In particular we find that the model orders ferromagnetically at small concentrations of frustration, and in all cases where ferromagnetic order occurs ($0 < x < 0.21$) there is a second low temperature transition where spin glass ordering occurs transverse to the magnetization at T_{xy}, in full agreement with our experiments on the bond frustrated alloy a-Fe_xZr_{100-x}. In addition, we find that the spin glass phase exists at finite T_{SG} for $0.21 < x \leq 0.5$ (the phase diagram is symmetrical about

x= 0.5). T_{SG} possesses a small clearly detectable concentration dependence, and we find that at $x_c = 0.21(1)$, T_C, T_{xy}, and T_{SG} merge at a multicritical point. We have followed the evolution of T_{xy} with magnetic field B for both the model and the material and we find full agreement between the two; T_{xy} is found to behave as $T_{xy}(B) = T_{xy}(0)(1 - \frac{B}{B+J})$ where J is a constant. That this particular equation, first suggested to describe experimental results, also accounts for the field dependance of T_{xy} in our bond frustrated model demonstrates that the only ingredients needed to describe the material is the presence of random competing bonds.

Résumé

Nous avons effectué des simulations de Monte Carlo à grande échelle de modèles frustrés de Heisenberg de liaison et de site afin de gagner la perspicacité dans les diagrammes de phase expérimentaux des matériaux magnétiques à sites frustrés et à liaisons frustrés. Dans le cas des modèles frustrés de site, nous constatons que l'ordre magnétique des verres de spin n'a pas lieu dans les réseaux cubiques simples ou cubique à corps centré qui sont bipartis. Au lieu de cela, le modèle se découple dans soit un ou deux faisceaux de percolation des sites ferromagnétiques (antiferromagnétique) qui exhibent un ordre ferromagnétique (antiferromagnétique). L'ordre est semblable à la situation qui existe quand les sites ferromagnétiques et antiferromagnétiques n'agissent pas l'un sur l'autre du tout. Ajouter une interaction entre les sites ferromagnétiques et antiferromagnétiques, pour créer la frustration, cause l'ordre ferromagnétique (FM) et antiferromagnétique (AFM) à devenir mutuellement perpendiculaires tout en augmentant les températures de transition ferromagnétiques (T_C) et antiferromagnétiques (T_N). Ce comportement est semblable à ce qui se produit dans nos expériences sur le a-$(Fe_{100-x}Mn_x)_{78}Si_8B_{14}$ frustré de site; pour cet alliage, l'ordre ferromagnétique et l'ordre de verre de spin co-existent transversal l'un à l'autre pour $0.17 < x < 0.31$. La frustration géométrique joue probablement un rôle significatif dans le matériaux puisque la structure de verre ne peut pas soutenir l'ordre antiferromagnétique, contrairement aux réseaux bipartis. Nous conjecturons que le modèle frustré de site sur le réseau non-biparti cubique face centrée, qui est géométriquement frustré en ce qui concerne l'ordre AF, produis un verre de spin avec un aspect aléatoire suffisant et serait un modèle supérieur.

Dans le cas du modèle de lien frustré, nous avons constaté que le diagramme de phase inclut toutes les phases en bloc prévues dans la théorie de champ moyen de Gabay et Toulouse il y a 25 ans, en dépit de la vue de longue date que les verres de spin de Heisenberg ne s'ordonnent pas en trois dimensions. En particulier nous constatons que le modèle mène à un ordre ferromagnétique à de petites concentrations de

frustration, et dans tous les cas où l'ordre ferromagnétique se produit ($0 < x < 0.21$) il y a une deuxième transition à basse température où l'ordre en verre de spin se produit transversal à la magnétisation à T_{xy}, entièrement en accord avec nos expériences sur l'alliage frustré de liaison a-Fe_xZr_{100-x}. En outre, nous constatons que la phase de verre de spin existe à T_{SG} fini pour $0.21 < x < 0.5$ (le diagramme de phase est symétrique autour de $x = 0.5$). T_{SG} possède une petite dépendance de concentration clairement discernable, et nous constatons qu'à $x_c = 0.21(1)$, T_C, T_{xy}, et T_{SG} convergent à un point multicritique. Nous avons suivi l'évolution de T_{xy} avec le champ magnétique B pour le modèle et le matériaux et nous trouvons le plein accord entre les deux; T_{xy} s'avère pour se comporter comme $T_{xy}(B) = T_{xy}(0)(1 - \frac{B}{B+J})$ où J est une constante. Que cette équation particulière, d'abord suggérée pour décrire des résultats expérimentaux, explique également la dépendance de champ de T_{xy} dans notre modèle frustré de liaison démontre que les seuls ingrédients requis pour décrire le matériaux est la présence des liens de concurrence aléatoires.

Acknowledgments

I would like to thank my supervisor, Dominic Ryan, for providing me with priceless advice and research guidance over my many years of study here at McGill. Dominic provided me with my thesis project, but also allowed me to follow many other avenues of research, for good or ill. Dominic was harsh when necessary, and set the level of expectation ever higher following even the smallest of my successes. His role as a my supervisor could not have been an easy one, and for his patience I am truely grateful. Not only a teacher and disciplinarian, Dominic is someone who I have come to view both as a friend and as a colleague.

Many thanks are also extended to Johan van Lierop and Sean Cadogan for their help during the collection of the μSR data at TRIUMF.

I would also like to thank my parents. My father Douglas Beath was instrumental in allowing me to explore my dreams unfettered; you are my hero and if I become half the father you are, I will have achieved enough in this life to be happy. My late mother, Loretta Beath, may you rest in peace, gave me my hunger for knowledge and for education. You made me realize that interest alone is reason enough to explore ones dreams. I hope I have made you proud; this thesis is dedicated to my memories of you.

The most important acknowledgement of all is reserved for the friendship and love I share with my fiancée Johanna Hume. At times I have been difficult – studying for my Ph.D. preliminary examinations comes to mind – yet your unwavering support and unconditional love continues to keep me on the correct path in difficult times. For this I thank you, my love.

I would like to thank Juan Gallego for help with the Dunedain and Shire beowulf clusters on which much of this work was accomplished. Lastly, my thanks go to Chris Voyer, fellow graduate student, who helped me in my most dire hours with the writting of this thesis.

Contents

List of Figures

List of Tables

Chapter 1

Introduction

1.1 Motivation

The study of spin glasses, sometimes referred to as magnetic glasses, attracted much attention in the 1980's as new materials were found and theoretical models were solved. However, by the latter portion of the decade it was essentially universally accepted that realistic, three dimensional, Heisenberg spin glass models did not order in three dimensions. While new Heisenberg like materials clearly showed indications of undergoing a phase transition, interest in the theoretical aspects were waning. Many continued to study Ising spin glass models, but the infinite anisotropy in the model (the spins may only point "up" or "down") means that many interesting aspects of real spin glasses cannot be studied. A prime example is transverse spin freezing: In particular, for many real systems a spin glass state is found to co-exist transverse to a long ranged and uniform magnetization below a temperature T_{xy}.

However, some workers resisted and continued to work on the problem of Heisenberg spin glasses[1, 2, 3, 4, 5, 6] claiming that the model ordered in three dimensions. Only recently has it been shown convincingly that this is actually the case[7, 8, 9, 10, 11]. These new and exciting results show that the study of Heisenberg spin glasses in three dimensions is a promising avenue of research. In particular, one would like to

know whether transverse spin freezing occurs at finite temperatures in these models as well.

1.2 Spin glasses and frustrated magnetism: A brief overview

A spin glass is by convention defined as a magnetic material which undergoes an ordering event in which the spins become locked in direction, yet the ordering is not periodic[12, 13, 14]. Magnetic glasses are analogous on some levels to structural glasses, although in the former there is ample evidence that a true finite temperature phase transition takes place for both models[7, 8, 9, 11, 15, 16] and materials[12, 14, 17]. In the latter the structural glass state is metastable only[14].

The difference between magnetic and structural glasses is attributed to the presumption that in a magnetic glass, the competing interactions are *quenched*; the interactions, frozen into the lattice, cannot adjust in order to produce a state that is periodic. In a structural glass the atoms can in principle relax such that the true ground state, the crystalline state, may be reached.

The spin glass state has peculiar magnetic characteristics such as very slow spin dynamics, memory (rejuvenation) effects, and aging effects[12, 13, 14, 17, 18], which are usually not found in periodically ordered magnets, such as conventional ferromagnets and antiferromagnets. In addition, the magnetic heat capacity shows no anomaly at the spin glass ordering temperature T_{SG}, and instead shows a rather broad hump at temperatures $T > T_{SG}$[13, 14, 17]. The heat capacity measurements all show that in the spin glass state, the materials possess an unusually large entropy, while the aging/rejuvenation experiments show that the low temperature states are highly degenerate.

These completely general features found in all real spin glasses lead one to believe that the spin glass phenomenon is caused by two primary factors[12, 13, 14, 17]:

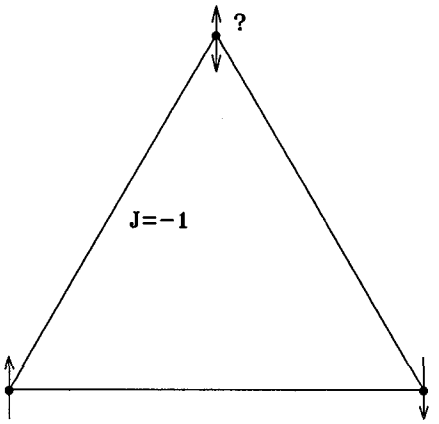

Figure 1.1: An illustration of three antiferromagnetically coupled spins which cannot simultaneously satisfy all three interactions. The top most spin, labeled with a question mark, can either point "up" or "down" if the bottom two spins are fixed to satisfy the antiferromagnetic coupling between them. This set of spins is said to be frustrated.

(i) randomness and (ii) frustration. Randomness, the first ingredient, is thought to be necessary if only because all spin glass systems contain some randomness and because no non-random models are known which capture the physics of real spin glasses. Frustration, the second ingredient, is a term used to describe a system of interactions which cannot all be satisfied simultaneously, such as the case of three antiferromagnetically coupled spins as shown in Fig. 1.1. Frustration can produce extremely high levels of ground state degeneracy, such as in the case of the triangular Ising antiferromagnet[19] or the face-centered cubic Ising antiferromagnet[20]. These two examples, however, do not form spin glass states as there is no randomness. While randomness and frustration alone cannot be sufficient conditions for the formation of a spin glass, as we shall demonstrate for a site-random model[21], these two ingredients together can produce a spin glass in sufficiently high concentrations, as we shall demonstrate for a bond-random model[11].

The mixture of randomness and frustration has led to a picture of the spin glass "free energy landscape" – or more properly an order parameter probability density

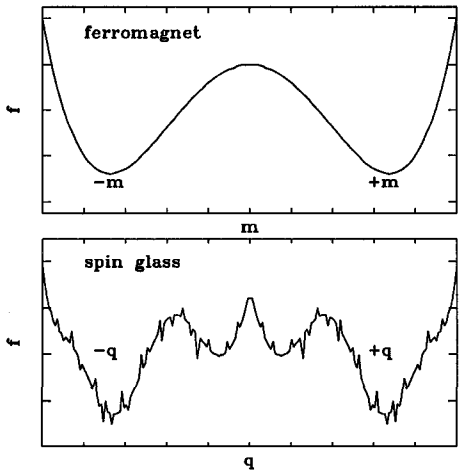

Figure 1.2: Schematic free energy landscapes for a non-frustrated ferromagnet (top) and for a frustrated spin glass (bottom). The horizontal axis is labelled by the appropriate order parameter; the magnetization m for the ferromagnet and the overlap q for the spin glass. While the ferromagnet has but two valleys corresponding to a magnetization $\pm m$, the spin glass has a rough landscape such that the system may become "trapped".

– which contains many valleys and bumps which may trap the system, leading to slow dynamics, aging and memory effects characteristic of a spin glass[14]. This idea of a rough free energy landscape is illustrated in Fig. 1.2 for both a conventional ferromagnet (top) and for a spin glass (bottom) where we have plotted a schematic free energy as a function of the appropriate order parameter; the magnetization m for the ferromagnet and the overlap q for the spin glass. In the case of a usual, non-frustrated, ferromagnet there are two minima existing at $\pm m$ below T_C, corresponding to the magnetized "up" and "down" states, each related by a global inversion of all of the spins (in this Ising like example). When ergodicity is broken below T_C the magnet will find itself trapped in one of the two minima, corresponding to $\pm m$, which allows the system to possess a non-zero magnetization. The free energy landscape for a spin glass, by contrast, is thought to be rough, containing several different local minima as well as the global minima at $\pm q$ (there may in fact be several equivalent minima not

related by a global symmetry operation, an active area of spin glass research). While ergodicity may still be broken (it must be, otherwise a finite T_{SG} has no meaning) such that only the states with either $+q$ or $-q$ are explored, this hypothetical spin glass will possess slow dynamics due to the necessity of hopping over the many free energy barriers which bound the many local minima. When out of equilibrium one expects that the rough free energy landscape to give rise to the memory and aging effects observed in spin glasses.

1.2.1 Transverse spin freezing

A most interesting feature of magnetic glasses is that, by virtue of the vector nature of the electronic spin, a spin glass state is found in the plane perpendicular to a pre-existing ferromagnetism in the concentration-temperature (x-T) phase diagrams[12, 13, 14, 17, 22, 23, 24, 25, 26, 27]. While still controversial, the existence of this mixed state appears in several spin glass materials and can be considered a precursor to the more conventional spin glass order: With decreasing T_C as a function of x the transverse spin glass temperature T_{xy} rises, and when the the two meet, only spin glass order appears below T_{SG}. Based on the mean field phase diagram of Gabay and Toulouse for a Heisenberg spin glass model[28], the destruction of the magnetization and the evolution towards a full blown spin glass are believed to be caused by a decrease in the mean ferromagnetic interaction strength and an increase in the amount of frustration. A magnetic phase diagram showing this evolution is shown in Fig. 1.3 for an amorphous $Fe_{90-x}Ru_xZr_{10}$ magnetic glass[27].

The experimental observation of a spin glass like state ordering transverse to the ferromagnetism in a-Fe_xZr_{100-x} and related alloys has led to three distinct interpretations; (i) finite antiferromagnetic clusters ordering randomly in an infinite ferromagnetically ordered matrix[29, 30, 31]; (ii) finite ferromagnetic clusters ordering randomly in an infinite ferromagnetically ordered matrix[32, 33, 34, 35, 36, 37, 38, 39]; (iii) a physical manifestation of a transverse spin glass co-existing with

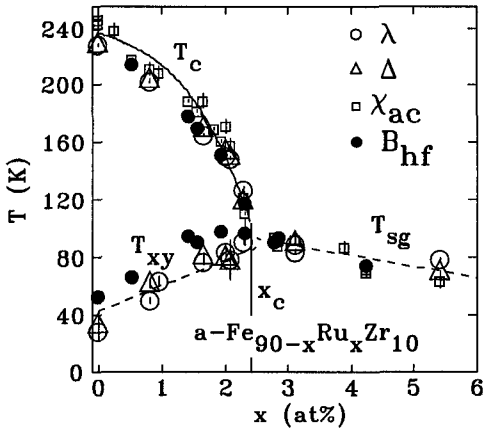

Figure 1.3: Magnetic phase diagram for a-$Fe_{90-x}Ru_xZr_{10}$ showing the Curie temperatures T_C, spin glass transition temperatures T_{SG}, and the onset of transverse spin glass order at T_{xy} as determined by μSR (λ, Δ), bulk magnetization χ_{AC}, and Mössbauer spectroscopy (B_{hf}).

ferromagnetism[22, 25, 26, 27, 40, 41, 42, 43, 44, 45] as found in the mean-field phase diagram of Gabay and Toulouse[28] (the GT phase). A principal argument against the view of transverse spin freezing being a manifestation of the GT phase is the long held conviction that in three dimensions with realistic short range interactions, Heisenberg spin glasses do not occur at finite temperatures[13, 14, 46, 47, 48]. Equivalently, it has been the conventional wisdom that the lower critical dimension of short range Heisenberg spin glasses is greater than three. Only recently, however, it has been shown that 3d Heisenberg spin glasses with short range interactions do indeed order at finite temperature[7, 8, 9, 10, 11]

The mean field phase diagram of Gabay and Toulouse[28] is reproduced in Fig. 1.4. The model studied has the Hamiltonian $H = -\sum_{ij} J_{ij}\vec{S}_i \cdot \vec{S}_j$ where S_i are three dimensional unit vectors and the sum runs over *all* pairs of spins. The interactions are taken from a Gaussian distribution of interactions with a mean bond strength $[J_{ij}] = J_0/N$ and standard deviation $[J_{ij}^2]^{1/2} = 1/\sqrt{N}$, where N is the number of spins and [ ] represents an average over disorder. In the phase diagram there are

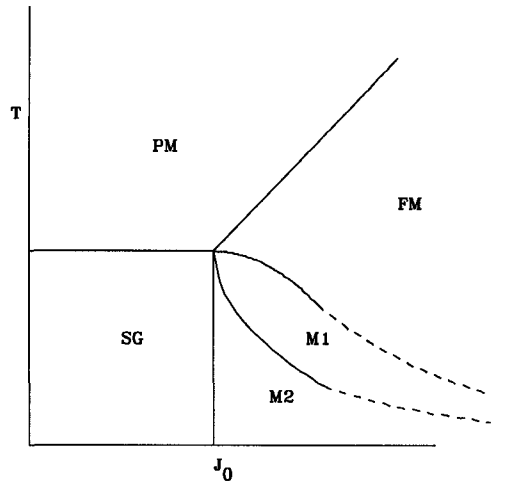

Figure 1.4: The mean field phase diagram of the bond frustrated Heisenberg model with Gaussian interactions as determined by Gabay and Toulouse in zero external field. For a description of the phases see text.

five distinct phases: paramagnetic (PM), ferromagnetic (FM), spin glass (SG), and two mixed phases, M_1 and M_2. The phase transition from FM to M_1 represents the ordering of spin glass components transverse to the magnetization[28] which we observe experimentally at T_{xy}, and which is sometimes referred to as the GT line. The second transition, from M_1 to M_2, represents the onset of replica symmetry breaking[28] and is sometimes referred to as the Almeida-Thouless (AT) line.

A transition likened to the AT line has been reported to exist[49] below T_{xy} in a-$(Fe_{1-x}Mn_x)_{75}P_{16}B_6Al_3$. Our results[23] for a-$(Fe_{1-x}Mn_x)_{78}Si_8B_{14}$ do not support this assertion; the signals used to identify the AT and GT lines in fact coincide[23] and there remains only a single transition at T_{xy}. Furthermore, it is not clear why this particular material was chosen to study the AT and GT lines. a-$(Fe_{1-x}Mn_x)_{75}P_{16}B_6Al_3$ is a *site* frustrated material and the appropriate model to study its behavior is a *site* frustrated model. The GT phase diagram, by contrast, describes a *bond* frustrated model and should be used to model *bond* frustrated materials. The AT line does not appear in the magnetic phase diagrams of bond frustrated materials either, as shown in Fig. 1.3 where only the GT line, labelled T_{xy} is observed.

Both transitions, FM to M_1 at T_{GT} (or T_{xy}) and M_1 to M_2 at T_{AT}, have specific forms for their dependence in an externally applied magnetic field B within mean field theory. The GT-line is predicted to scale at small fields as

$$T_{GT} \propto T_0 \left(1 - A_{GT} B^2\right) \qquad B \to 0 \tag{1.1}$$

with T_0 being the value of T_{xy} in zero field, and A_{GT} a constant. Thus, mean field theory predicts that $T_{xy}(B)$ is concave down. The AT-line is predicted to follow a different form in small fields, namely

$$T_{AT} \propto T_0 \left(1 - A_{AT} B^{2/3}\right) \qquad B \to 0 \tag{1.2}$$

where A_{AT} is another constant. T_{AT} is concave up. In mean field theory both transitions asymptotically approach $T = 0$ exponentially in B^2;

$$T_{GT,AT} \propto \exp\left(-AB^2\right) \qquad B \to \infty \tag{1.3}$$

with A being another constant.

None of these forms however captures the behavior we observe in our experiments on the field dependence of T_{xy} for a-Fe_xZr_{100-x}. Instead, it is found[44, 45] that the function

$$T_{xy}(B) = T_{xy}(0)\left(1 - \frac{B}{B+J}\right) \tag{1.4}$$

accurately represents the reduction of T_{xy} with increasing B which we confirm for four different samples over a range of fields in which T_{xy} decreases by a factor of four. In Fig. 1.5 we show the decrease of T_{xy} with increasing B as determined in our μSR experiments on a-$Fe_{93}Zr_7$ and compare it to Eqn. 1.1, Eqn. 1.2, and Eqn. 1.4 (Eqn. 1.3 is clearly seen to fail). Only Eqn. 1.4 shown by the solid line in Fig. 1.5 is consistent with the data.

Mean field theory fails to predict the functional form of $T_{xy}(B)$. This failure is not surprising since mean field theory describes models above their upper critical dimension, and the upper critical dimension of Heisenberg spin glass models are certainly greater than three[8, 9, 13, 14]. In our Monte Carlo simulations of the three

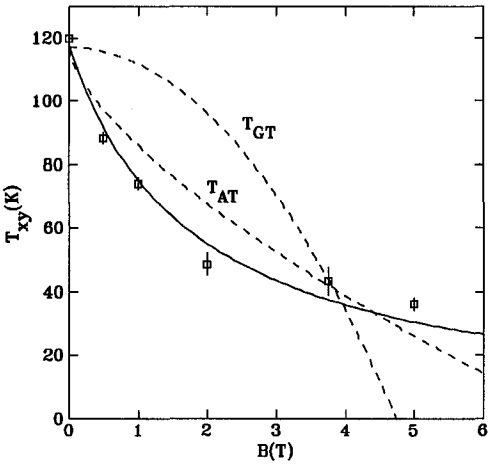

Figure 1.5: The decrease of T_{xy} with an increasing applied magnetic field B as determined from the peak location in the fluctuation rate λ observed in μSR experiments. The solid line is a fit to Eqn. 1.4 while the dashed lines correspond to the GT line (Eqn. 1.1) and the AT line (Eqn. 1.2). The GT line and the AT line have been scaled so as to pass through the data point at $B = 3.75$ Tesla.

dimensional bond frustrated Heisenberg model, we also find $1/B$ scaling of $T_{xy}(B)$ over a range of fields where T_{xy} drops by about a factor of five. The agreement between simulation and experiment gives strong evidence that the form of the magnetic phase diagrams of alloys such as a-Fe_xZr_{100-x} is controlled solely by randomness and frustration, as these are the only ingredients introduced into the model.

1.3 Site versus bond frustration

In real materials, frustration can be introduced in two distinct ways. The most popular theoretical models used to study short range spin glasses introduce the frustration bond wise, and we refer to models and materials which possess frustration of this type as "bond frustrated". Perhaps the best examples of bond frustrated magnets are the amorphous Fe_xZr_{100-x} alloys[25, 26]. Bond frustrated models are based on the idea, originally proposed by Edwards and Anderson[50], that the spin glass state may be described by a Hamiltonian $\mathcal{H} = -\sum_{ij} J_{ij} S_i S_j$ with classical spins S_i and S_j

interacting via a *random* bond J_{ij} which may take either a positive (ferromagnetic) or negative (antiferromagnetic) value which is fixed (quenched disorder). When the average interaction strength $< J_{ij} >= 0$ it is expected that ferromagnetic and antiferromagnetic order cannot occur[50]. Instead, the lowest temperature states are ones where the spins become frozen without periodicity, hence a spin glass. The order parameter that Edwards and Anderson proposed to measure the spin glass order[50] is known as the EA order parameter q;

$$q_i(t) =< S_i(t_0)S_i(t_0 + t) > . \tag{1.5}$$

Below the transition temperature and for long times t_0 it was proposed that q_i will take a finite value since the spin S_i at long times t will have a finite probability of being oriented in the same direction as $S_i(t_0)$.

In three dimensions with short range nearest neighbor interactions, the Ising spin glass ($S_i = \pm 1$) with a random distribution of $J_{ij} = \pm 1$ bonds was shown to order at finite $T_{SG} \sim 1.2$ as early as 1985 by Ogielski[16] using Monte Carlo simulations. Ogielski demonstrated that $q(t \rightarrow \infty) = \sum_i q_i(t)$ is strictly zero for finite lattices due to the fact that: (i) the Hamiltonian is symmetric with respect to an overall global inversion of the spins and (ii) since the Monte Carlo method is ergodic for finite lattices, meaning that all possible phases are sampled in the limit $t \rightarrow \infty$. However, it was also demonstrated that there exists a finite temperature where the time required for ergodicity to be achieved diverges with increasing system size L. Therefore, Ogielski concluded[16] that in the thermodynamic limit there exists a finite temperature T_{SG} below which ergodicity is broken, and thus a phase transition! Further Monte Carlo work on short range Ising spin glasses in three dimensions has in recent years confirmed that T_{SG} is finite for 3d Ising spin glasses with both a Gaussian distribution of bonds[51, 52, 53] and with $\pm J$ distribution of bonds[54, 55, 56]. The best results have come from Monte Carlo measurements of the spin glass correlation length by Ballesteros *et al.*[15].

The other way to make a spin glass is to mix ferromagnetic and antiferromag-

netic sites together in an amorphous solid, a good example being amorphous a-$(Fe_{1-x}Mn_x)_{78}Si_8B_{14}$ [23, 24]. Here, ferromagnetic and antiferromagnetic interactions between neighboring sites is determined by the labels of the neighboring magnetic species. We will refer to this class of spin glass models as "site frustrated". Much less theoretical work has been done on site frustrated models, despite the fact that differences between site frustration and bond frustration were expected at least 20 years ago[14] and the fact that many real spin glasses are actually site frustrated. Early mean field results of a site frustrated model introduced indicated that a random distribution of ferromagnetic and antiferromagnetic sites could produce a spin glass[57]. However, Monte Carlo simulations of three dimensional nearest neighbor site frustrated models with Heisenberg spins are in conflict[58, 59, 60] and one would like to know whether the ordering observed in the real materials can be captured with a site frustrated model.

1.3.1 a-$(Fe_{1-x}Mn_x)_{78}Si_8B_{14}$: A site frustrated magnetic glass.

To make a site frustrated material two magnetic species are mixed at random, one of which acts ferromagnetically and the other antiferromagnetically. A good example which we study is the series of amorphous alloys a-$(Fe_{1-x}Mn_x)_{78}Si_8B_{14}$[23, 24]. The magnetic phase diagram is shown in Fig. 1.6. Here, neighboring Fe–Fe interactions are ferromagnetic and for $x < 0.17$ the material is ferromagnetic at all temperatures below T_C. Introducing Mn at low levels simply reduces the zero temperature magnetization proportional to the Mn spin, demonstrating that Fe–Mn interactions are antiferromagnetic[23, 24]. The Mn–Mn exchange interactions are also antiferromagnetic, which can be revealed by the short range antiferromagnetic correlations which develop in the transverse spin glass state[24]. Furthermore, *if* the Mn–Mn contacts were not antiferromagnetic the material would not be frustrated; Mn moments would simply orient opposite to Fe moments over the entire phase diagram, which is at odds with the experiments[23, 24]. Instead, for $0.17 < x < 0.31$ a transverse spin glass

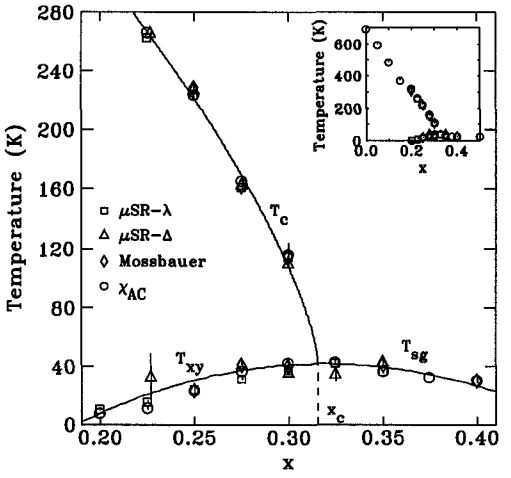

Figure 1.6: Magnetic phase diagram for a$-(Fe_{1-x}Mn_x)_{78}Si_8B_{14}$ derived from ac-susceptibility data (χ' for T_c, χ'' for T_{xy}), $< B_{hf} >$(T) from Mössbauer spectroscopy, and both Δ and λ from the ZF-μSR. Three transitions can be identified: ferromagnetic ordering at T_c, transverse spin freezing at T_{xy}, and spin glass ordering only for $x > x_c$ at T_{sg}. Note the perfect agreement between independent determinations of T_{xy}. Inset shows data for whole composition range studied.

state exists below T_{xy} which co-exists with ferromagnetic order. For $x > 0.31$ the material is a spin glass.

It is important to note that in the amorphous a-$(Fe_{1-x}Mn_x)_{1-y}G_y$ series of alloys, the glass former (G) is largely unimportant for the magnetic ordering that takes place. The overall similarity between the phase diagrams of a-$(Fe_{1-x}Mn_x)_{75}P_{16}B_6Al_3$ [61, 62, 63, 64, 65], a-$(Fe_{1-x}Mn_x)_{75}P_{15}C_{10}$ [66], a-$(Fe_{1-x}Mn_x)_{77}Si_{10}B_{13}$ [67], and a-$(Fe_{1-x}Mn_x)_{78}Sn_2Si_6B_{14}$ [24] all demonstrate that it is the antiferromagnetic character of Mn which dominates the magnetic response while the glass former is largely irrelevant.

Based on extensive Monte Carlo simulations[21, 68, 69], Mössbauer spectroscopy[23, 24] and μSR measurements[23] we conclude that the transverse spin glass state in this material is predominantly made up of Mn. While the magnetic phase diagram of this site frustrated alloy appears similar to that of the bond frustrated alloys, the physics

governing the phase diagram as well as the phases themselves are quite different. In the bond frustrated material a-$Fe_{90-x}Ru_xZr_{10}$ alloys, only Fe carries a magnetic moment and the magnetic phase is distributed uniformly over the sample. By contrast, in the site frustrated material the ferromagnetic order is associated with Fe moments while the transverse spin glass and spin glass phases are associated with Mn moments.

1.3.2 A simple models for site-frustrated materials

To study the behavior of site frustrated materials we consider a three dimensional classical Heisenberg model with the Hamiltonian

$$\mathcal{H} = -\sum_{<ij>} J_{ij}\vec{S}_i \cdot \vec{S}_j \tag{1.6}$$

where the sum runs over all nearest neighbor bonds J_{ij}. The distribution of bonds in site frustrated models can be expressed as

$$J_{ij} = J_{FF}x_ix_j + J_{AA}(1-x_i)(1-x_j) + J_{FA}[x_i(1-x_j) + x_j(1-x_i)] \tag{1.7}$$

where $x_i = 1$ if site i is occupied by a F (ferromagnetic) site and $x_i = 0$ if site i is occupied by an A (antiferromagnetic) site. For random F/A occupancy, the probability of site i being F type $P(x_i = 1) = (1-x)$ and the probability of site i being A type $P(x_i = 0) = x$. Our site frustrated model corresponds to the choice

$$J_{FF} = -J_{AA} = -J_{FA} = 1. \tag{1.8}$$

The interactions $J_{ij} = +1$ ($J_{ij} = -1$) correspond to ferromagnetic (antiferromagnetic) bonds. We have chosen J_{FA}=-1 since in our experimental work[23, 24] on a-$(Fe_{1-x}Mn_x)G$, bulk magnetization, Mössbauer spectroscopy, and μSR measurements all show that for small x, the Mn moments orient opposite to the Fe rich FM bulk. However, the phase diagram is invariant with respect to the sign of J_{FA} for bipartite lattices and so this choice of sign is unimportant. We have considered three different lattice types, simple cubic (sc), body-centered cubic (bcc), and face-centered cubic

(fcc) with linear dimension L containing $N{=}L^3$, $N{=}2L^3$, and $N{=}4L^3$ sites respectively, with periodic boundary conditions and L even. The fcc lattice is not bipartite though, and so the phase diagram is much more complex as it is not symmetrical about $x = 0.5$. We have not endeavored to measure the antiferromagnetic order in the fcc version of the model, although this is a very promising avenue for future work.

We have also considered a related (and trivial) non-frustrated model with

$$J_{FF} = -J_{FA} = 1 \quad \text{and} \quad J_{FA} = 0. \tag{1.9}$$

This model describes a network of ferromagnetic clusters and antiferromagnetic clusters which do no interact. Consequently, the model possesses no frustration for bipartite lattices. The ordering which occurs for this non-frustrated model is easily discerned from the theory of dilute magnetism where finite temperature ordering takes place when a percolating cluster of sites forms, provided that the pure model ($x = 0, 1$) orders as well. The phase diagrams for this model is illustrated in Fig. 1.7(a) for sc and bcc lattices.

The first to study the site frustrated model, to the best of our knowledge, was Aharony[70] who used renormalization group techniques. His phase diagram for bipartite lattices, shown in Fig. 1.7(a) is similar to ours (see Fig. 4.1(a) and Fig. 4.1(b)), in that a tetracritical point bounds a mixed phase consisting of coexisting FM and AF order. The FM+AF mixed phase, it is concluded, consists of FM order perpendicular to AF order. This is precisely what we observe.

Further work[71], however, cast doubt on his original result. It was concluded that the phase diagram may instead be of the type shown in Fig. 1.7(b). It is important to note that in this work a true site frustrated model was not being considered. Instead, the site frustrated model was considered to be equivalent to the bond frustrated model, apart from short range correlations which were deemed unimportant for the long range ordering that takes place. Within mean field theory, the phase diagram of this bond frustrated model is now well understood[28] and has already been shown in Fig. 1.4. *If* the bond and site frustrated models were gauge equivalent, as presumed,

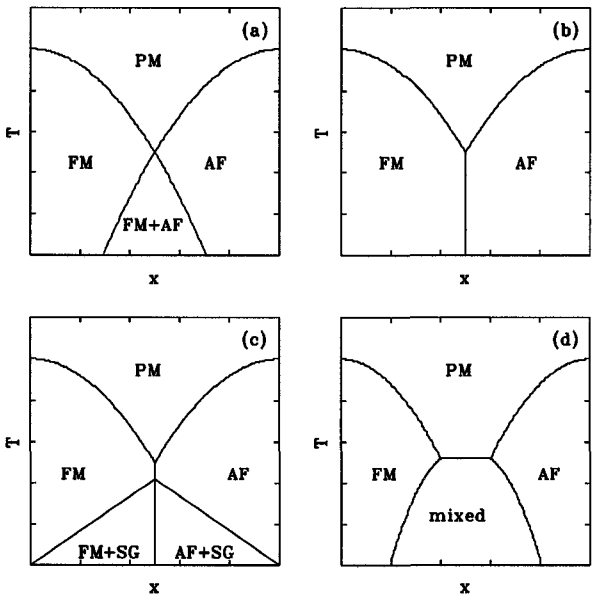

Figure 1.7: Conjectured phase diagrams for the site frustrated model. (a) Phase diagram as originally given by Aharony[70]. FM and AF refer to ferromagnetic and antiferromagnetic order respectively, while PM is the paramagnetic (disordered) phase. Our work reveals this to be the correct phase diagram for bipartite lattices. (b) Phase diagram postulated by Fishman and Aharony[71]. (c) The phase diagram of the site frustrated model as determined by the Monte Carlo simulations of Bekhechi and Southern[60]. (d) Phase diagram which would result in three dimensions were the site frustrated model gauge equivalent to the bond frustrated model, based on our results for the bond frustrated Heisenberg model[11]

then the phase diagram of the site frustrated models in three dimensions would appear as in Fig. 1.7 (c). In this case, the model would never have a true spin glass phase for at all concentrations there would be either ferromagnetic or antiferromagnetic order. However, there would also be a line of transitions at T_{xy} where spin glass ordering takes place transverse to the FM or the AF order. The site frustrated model, however, is not equivalent to a bond frustrated model and the physics is fundamentally different.

The best results for the site frustrated Heisenberg model have been obtained from Monte Carlo simulations[21, 58, 59, 60, 68, 69, 72], yet the authors disagree in their interpretations of the phase diagram. Two studies[58, 60] claim that a mixed non-collinear phase, similar to spin glass order, exists in the vicinity of $x = \frac{1}{2}$. Bekhechi and Southern[60] claimed that the tetracritical point, where $T_C(x) = T_N(x)$, does not exist and instead there exists a regime $0.52 < x < 0.48$ where $T_C(x) = T_N(x)$, illustrated in Fig. 1.7 (d). On the other hand, we[68] and others[59] have claimed that the mixed phase is bounded by a tetracritical point and that the AF and FM ordering vectors are mutually perpendicular. In addition, it has been reported[59, 60] that the ferromagnetic transition belongs to the Heisenberg universality class for small x, and that with increasing x the universality class of the transition changes, in contradiction to the Harris criterion[73]. Resolving the different interpretations is important since one would like to identify the minimal physics necessary to understand the phase diagrams of real materials.

1.3.3 a-Fe_xZr_{100-x}: A bond frustrated magnetic glass

Unlike site frustrated materials, the amorphous alloys[26] a-Fe_xZr_{100-x} are bond frustrated. Here the competing random exchange interactions arise from the distance dependence of the direct Fe–Fe exchange couplings together with the glassy distribution of nearest neighbor distances inherent to the glass structure. The magnetic phase diagram, shown in Fig. 1.8, is nearly the same as for the a-$Fe_{90-x}Ru_xZr_{10}$ magnetic phase diagram (Fig. 1.3) except that beyond $x \sim 93$, where one expects a spin

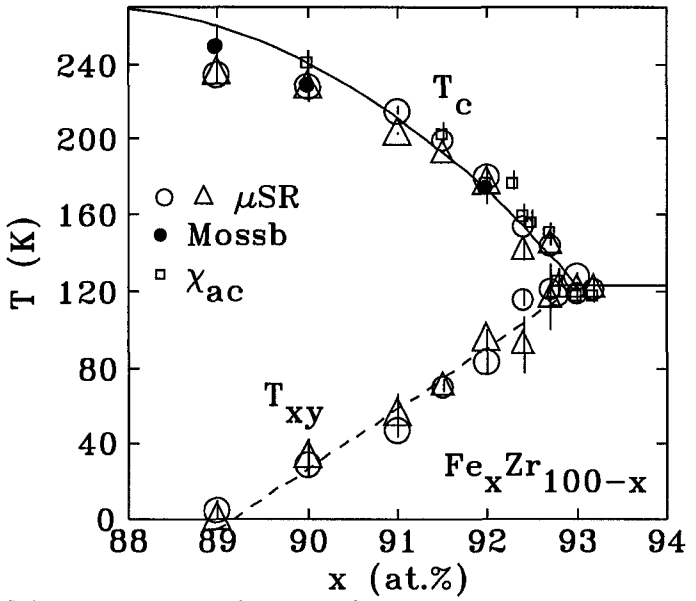

Figure 1.8: Magnetic phase diagram for a-Fe_xZr_{100-x} showing the Curie temperatures T_C, spin glass transition temperatures T_{SG}, and the onset of transverse spin glass order at T_{xy} as determined by μSR (λ, Δ), bulk magnetization χ_{AC}, and Mössbauer spectroscopy (B_{hf}).

glass phase, the material can no longer be made. In any case, the phase diagram, previously described for the Ru doped version, is typical of many spin glass materials, and shows the same structure as the GT phase diagram, except that the AT line is not observed in the experiments.

One feature which makes the a-Fe_xZr_{100-x} series of alloys an excellent material in order to study the physics of frustrated magnetism is that the material is one of the most well characterized experimental realizations of a classical Heisenberg ferromagnet with competing exchange interactions[39, 74, 75, 76, 77, 78]. Furthermore, it has also been demonstrated that the exchange interactions are of the nearest neighbor variety[39]. The concept of universality is prominent in modern statistical physics; belonging to a particular universality class requires that the magnetic moments in the material possess certain symmetries. For a material to belong to the three dimensional Heisenberg universality class requires that the magnetic moments in the

material be three dimensional with negligible anisotropy of the uni-axial (Ising universality class) or planar (xy universality class) variety[79]. Since a-Fe_xZr_{100-x} belongs to the Heisenberg universality class and the exchange interactions are short range, we can with confidence model its magnetic response with a classical Heisenberg model with nearest neighbor interactions in the hope that we may recover the behavior of the material.

1.3.4 A simple model for bond-frustrated materials

To model the magnetic behavior of such an alloy we study the a well known variant of the Edwards Anderson model[50], the three dimensional ±J bond frustrated Heisenberg model[5, 6, 7, 8, 9, 10, 11, 46, 47, 48, 80, 81]. The bond frustrated Heisenberg model that we study here has the Hamiltonian

$$\mathcal{H} = -\sum_{<i,j>} J_{ij}\mathbf{S}_i \cdot \mathbf{S}_j - B_z \sum_i \vec{S}_i \cdot \hat{z} \tag{1.10}$$

where the sum runs over all pairs of nearest neighbor, unit vector, classical Heisenberg spins, $\mathbf{S}_i$, residing on a three dimensional simple cubic lattice of linear dimension L with periodic boundary conditions. The field B_z, if present, is directed along the $\hat{z}$ axis. The exchange interactions J_{ij} for spin glass models are usually taken either from a Gaussian distribution with mean J_0 and unity variance[7, 8, 9, 28, 46, 47, 48], or in our case a $\pm J$ distribution[5, 6, 15, 68, 80, 81] with probability

$$P(J_{ij} = +1) = 1 - x \qquad \text{and} \qquad P(J_{ij} = -1) = x. \tag{1.11}$$

Our choice of the $\pm J$ distribution is motivated by the fact that for $x = 0$ the model is free of both disorder and frustration, and reduces to the well understood Heisenberg ferromagnet with $T_C = 1.4429(1)$[82, 83].

While it has long been thought that the model does not possess a finite temperature transition in three dimensions[13, 14, 46, 47, 48] it has been suggested that chiral degrees of freedom associated with handedness of the rotation of the spins do

order at finite temperature[1], even though the spins themselves do not order at finite temperature. Monte Carlo simulations have been performed that claim to support a finite temperature ordering of the spin chiralities[2, 3] with no finite temperature ordering of the spins. One of the main arguments given in these works is that the EA order parameter q (Eqn. 1.5) generalized for Heisenberg spins goes to zero in the limit of long times at all temperatures. As discussed in section 1.3, this does not mean that the model does not order at a finite temperature transition since q necessarily goes to zero in the limit of long times for finite lattices. Indeed, in 2003 Lee and Young showed that for a three dimensional Heisenberg spin glass with a Gaussian distribution of bonds the spins do in fact order at the same finite temperature as the chiralities[7] and that Heisenberg spin glasses undergo a finite temperature phase transition in three dimensions.

Chapter 2

Experiments

In this chapter we describe the experiments conducted on the site frustrated material a-$(Fe_{1-x}Mn_x)_{78}Si_8B_{14}$ and the bond frustrated material a-$Fe_{100-x}Zr_x$. In the first section we briefly review the main experimental techniques used: Mössbauer spectroscopy and muon spin relaxation (μSR). Excellent reviews of Mössbauer spectroscopy[84, 85] and μSR technique[85, 86, 87] exist, and so we do not give a detailed description here. Instead, we provide a brief introduction to both methods so that the reader may follow our experiments and the results derived from them.

The main difference between the two experimental techniques is that in our Mössbauer experiments we obtain the average static hyperfine magnetic field at the Fe site, $< B_{hf} >$, which is primarily due to the ordering of Fe moments, while in our μSR experiments we obtain the average static magnetic field at the muon site, Δ, which is sensitive to the ordering of both Fe and Mn moments. The difference is particularly revealing in the case of the site frustrated alloy where the two signals do not track together in temperature, unlike bond frustrated materials, and serves to demonstrate that the ordering at T_{xy} in site frustrated materials is primarily associated with antiferromagnetic Mn sites. In addition to the static magnetic fields Δ, μSR yields the *dynamic* relaxation rate of the muon, λ, caused by temporal fluctuations of the magnetic field. Thus, the two methods give complementary information

on the static magnetic fields in the sample, while μSR also gives information about the dynamics of the magnetic fields in the sample.

In the second and third sections we give the results of our experiments in a site frustrated material and a bond frustrated material respectively. For the site frustrated material we have determined the zero field phase diagram over a wide composition regime. Our results are in agreement with our expectations arising from both prior experimental work[61, 62, 63, 64, 65, 66, 67, 88] and from our simulations of site frustrated models[21, 68, 69]. For the bond frustrated material, the zero field phase diagram is already known in great detail[25, 26]. In order to gain further insight into the magnetic behavior of the material we have determined the dependence of T_{xy} on an externally applied magnetic field. The field dependence found for four different compositions agrees with the functional form given in Eqn. 1.4, as well as our Monte Carlo simulations of the three dimensional bond frustrated Heisenberg model, long argued to capture the physics of transverse spin freezing in bond frustrated materials.

2.1 Experimental Methods

2.1.1 The ^{57}Fe Mössbauer effect in magnetic glasses

A free nucleus undergoing nuclear decay from energy E_2 to E_1 will emit a photon with energy E_γ less than energy difference, $\Delta E = E_2 - E_1$, of the initial and final nuclear states due the recoil of the nuclei. The energy of the photon is given by $E_\gamma = \Delta E - \frac{1}{2}Mv^2$, where M is the mass of the atom which recoils with a velocity $v = -p_\gamma/M$, and where $p_\gamma = E_\gamma/c$ is the momentum of the photon. The recoil energy is just $E_R = E_\gamma^2/2Mc^2$.

By symmetry, the same free nucleus in state E_1 may also absorb a photon with energy $\Delta E + E_R$, exiting the nuclei into the state with energy E_2. If excited nuclei are used as a source, and ground state nuclei as absorber, resonant absorption may take place as shown in Fig. 2.1 by the overlap region of the energy probabilities, each

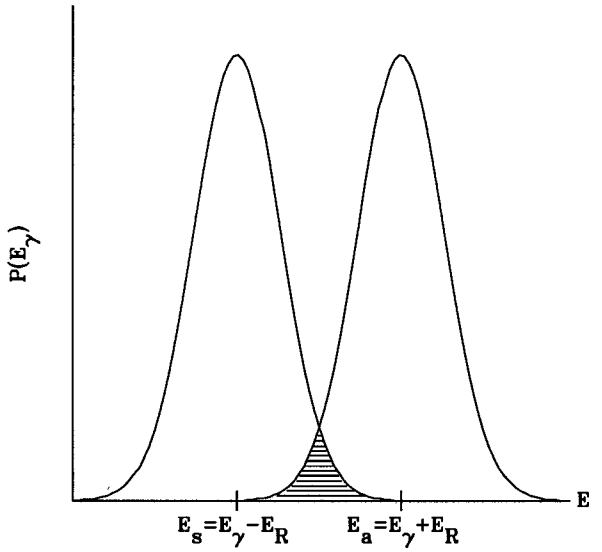

Figure 2.1: The energy probability from the source at energy E_s and the for the absorber at energy E_a. Both probability densities are spread due to the random thermal motion of the atoms in the solid (Doppler effect). In the region where the overlap of the two probabilities occur (hatched), resonant absorption may occur.

spread in energy due to random thermal motion of the nuclei. However, the overlap region is in reality extremely small and resonant absorption is not readily observed for free nuclei.

Mössbauer[89], however, realized that if the source and absorber were in the form of a solid, than the recoil energy may be taken up by the crystal as a whole. In this case E_R will be zero, since $Mc^2 \gg E_\gamma$ when M is the mass of the crystal, and recoil free emission and absorption may take place.

If now identical nuclei are used as source and absorber in different crystal structures, then the different environments presented to the nuclei will alter the nuclear energy levels. In a Mössbauer experiment, the source photons are Doppler shifted, and when the energy of the Doppler shifted photon coincides with the energy of a nuclear transition in the absorber, resonant absorption may take place. Measurement of the photons energy where resonant absorption occurs allows one to determine the shift in energies produced by the interactions between the nuclei and crystal structure.

The Doppler shift energy ΔE is given by $\Delta E = \frac{v}{c}E_\gamma$ where v is a small velocity of the order of mm/sec., obtained by attaching the source onto a commercially available mechanical drive. Scanning through energies is accomplished by varying the drive velocity. Data collection is performed with electronics which bins the detected photons not absorbed by the sample according to the velocity of the drive.

In our ^{57}Fe Mössbauer experiments, the source is ^{57}Co**Rh**. The ^{57}Co source decays predominantly by electron capture into the $I = \frac{5}{2}$ excited state of Fe. Subsequent decay of this $I = \frac{5}{2}$ state populates the $I = \frac{3}{2}$ state, which finally decays into the $I = \frac{1}{2}$ ground state along with the emission of the 14.4 keV gamma ray used in our ^{57}Fe Mössbauer experiments.

The absorbers used in our Mössbauer experiments are the ^{57}Fe nuclei which make up much of the site and bond frustrated materials we study. Due to electric quadrupole interactions and the Zeeman effect, the ground states and the excited states of the nucleus can experience a splitting of their energy levels. The $I = \frac{1}{2}$ ground state may be split due to a magnetic field (Zeeman effect), while the $I = \frac{3}{2}$ excited state may be split by both an electric quadrupole interaction and a magnetic field.

In the case of a quadrupole interaction, the excited $I = \frac{3}{2}$ state will split into two energy levels corresponding to $m_I = \pm\frac{1}{2}$ and $m_I = \pm\frac{3}{2}$ ($I = \frac{1}{2}$ states do not couple to electric field gradients). The energy difference between the two states is $\Delta E = eQV_{zz}/2$ where Q is the nuclear quadrupole moment of the $I = \frac{3}{2}$ state and V_{zz} is the principal axis of the electric field gradient at the nuclear site[84, 85]. Thus, in the presence of an electric field gradient two Mössbauer lines will be observed as illustrated in Fig. 2.2(a).

In the presence of a hyperfine magnetic field B_{hf}, the $I = \frac{1}{2}$ ground state energy is split into two energy states ($m_I = +\frac{1}{2}, -\frac{1}{2}$) while the $I = \frac{3}{2}$ excited state is split into four energy states ($m_I = +\frac{3}{2}, +\frac{1}{2}, -\frac{1}{2}$, and $-\frac{3}{2}$), as illustrated in Fig. 2.2(b). This is the Zeeman splitting. Since transitions are only allowed for $\Delta m = 0, \pm 1$, there are

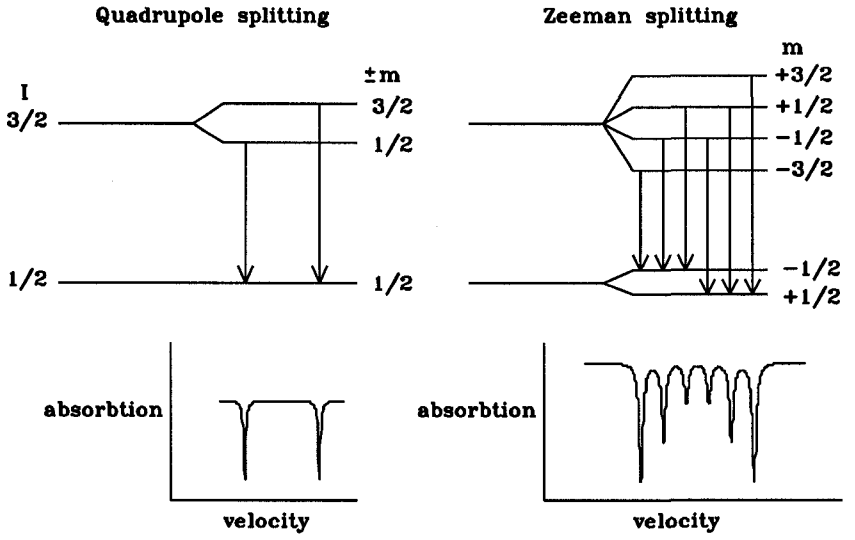

Figure 2.2: ^{57}Fe Mössbauer spectra for a pure quadrupole interaction (left) and for a pure Zeeman interaction (right).

six allowed transitions each with different energies[84, 85]. It can be shown[84, 85] that the line intensities are related to one another by the ratios $3:2:1:1:2:3$ for outer:middle:inner:inner:middle:outer respectively for polycrystalline samples. The transition energies are

$$\hbar\omega = \hbar\omega_0 - \left(\frac{\mu_e}{I_e}m_e - \frac{\mu_g}{I_g}m_g\right)B_{hf} \tag{2.1}$$

where the subscripts refer to the excited state (e) and the ground state (g), $\mu_{e,g}$ are the nuclear magnetic moments in the e and g states, and $\hbar\omega_0$ is the unshifted energy difference (14.4 keV) between the e and g states. The resonant velocities, v_{res}, where absorption occurs is

$$v_{res} = -\frac{c}{\hbar\omega_0}\left(\frac{\mu_e}{I_e}m_e - \frac{\mu_g}{I_g}m_g\right)B_{hf}. \tag{2.2}$$

In addition to the quadrupole splitting and the Zeeman splittings, there is the isomer shift which reflects differences between the electron density at the nuclear site between the source and absorber[84, 85]. The isomer shift gives rise to an offset of the spectrum away from the zero velocity of the Doppler shift and is easily accounted for.

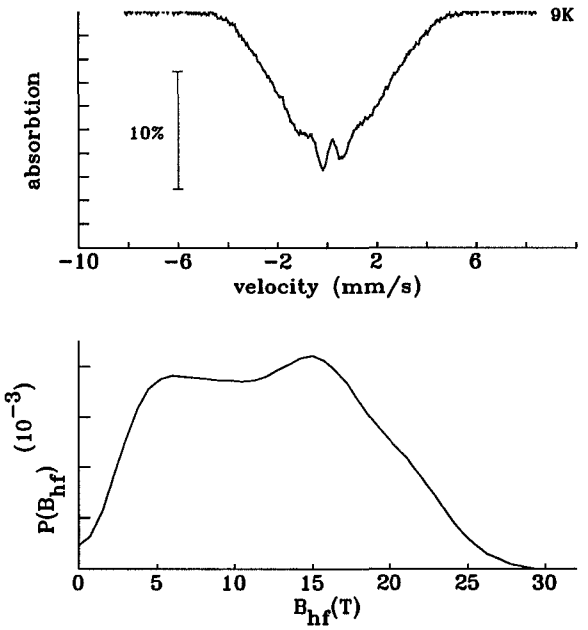

Figure 2.3: (top) Mössbauer spectrum for a-$(Fe_{0.725}Mn_{0.275})_{78}Si_8B_{14}$ at $T = 9K$, well below T_C and T_{xy}. Errors are of the order of the width of the fitted line (solid) using Window's method. The fit provides the distribution of hyperfine fields seen at the nuclei (bottom).

In a glassy, disordered sample which has a distribution of static, frozen, moments one expects that a distribution of magnetic fields will be present. So rather than a six line spectrum being observed one expects instead to have a distribution of six line spectra corresponding to the different fields at the Fe sites. We thus fit our Mössbauer spectra using Window's method[90] where the distribution of hyperfine fields $P(B_{hf})$ is written as

$$P(B_{hf}) = \sum_n a_n[cos(n\pi B_{hf}/B_{max}) - (-1)^n] \tag{2.3}$$

where B_{max} is a limiting maximum field. A sample spectrum for a-$(Fe_{72.5}Mn_{27.5})_{78}Si_8B_{14}$ at $T = 9K$ is shown in Fig. 2.3(top) along with the resulting $P(B_{hf})$ found using a standard non-linear least squares fitting routine. In the fits we have used between 8 and 10 Fourier components, and we have assumed a linear relationship between the Isomer shift and the average magnetic hyperfine field in order to account for the slight asymmetry in the spectra. The quadrupole shift is set to zero because in our

samples we can safely assume that the principal axes of the electric field gradients are uncorrelated with the direction of the magnetic field at the nuclear sites. If this is the case, the effect of the quadrupole splitting is to give rise to an apparent broadening of the spectra away from the experimentally limited linewidth of 0.13 mm/s.

2.1.2 μSR methods for magnetic glasses

In a μSR experiment, a spin polarized beam of positive muons are implanted into a sample. Due to the positive charge, the muons enter as interstitials. The presence of a local magnetic field, B_{loc}, at the muon site causes the muon to precess, a fact on which the entire μSR technique rests. For a frame of reference where the muon is polarized along the $\hat{z}$ direction, and with B_{loc} at an angle θ to the $\hat{z}$ direction, the polarization $A_z(t)$ will evolve according to[85, 87]

$$A_z(t) = \cos^2\theta + \sin^2 cos(\omega t) \tag{2.4}$$

where $\omega = 2\pi\nu_\mu = \gamma_\mu B$ and γ_μ =851.6 Mrad$\cdot$ s$^{-1}\cdot$ T^{-1}. When the muon decays, its decay positron is directed preferentially along the muons polarization and is detected with counters placed in the forward (F) and backward (B) directions. In a μSR experiment one follows the time dependence of the muon polarization by measuring the asymmetry,

$$A(t) = \frac{F - B}{F + B} \tag{2.5}$$

which gives information about the static and dynamic magnetic fields at the muon sites.

For a magnetic sample in zero field, there will be a distribution of local fields at the muon sites. In this case one expects that the distribution of local fields can be written as

$$D(B_{loc}) = \left(\frac{\gamma_\mu}{\sqrt{2\pi}\Delta}\right)^3 \prod_{\alpha=x,y,z} \exp\left(-\frac{\gamma_\mu^2 B_{loc,\alpha}^2}{2\Delta^2}\right). \tag{2.6}$$

were $\alpha = x, y, z$ are the three Cartesian components and $\Delta^2/\gamma_\mu^2 =< B_x^2 >=< B_y^2 >=< B_z^2 >$. Averaging of the polarization $A_z(t)$ over the distribution $D(B_{loc})$

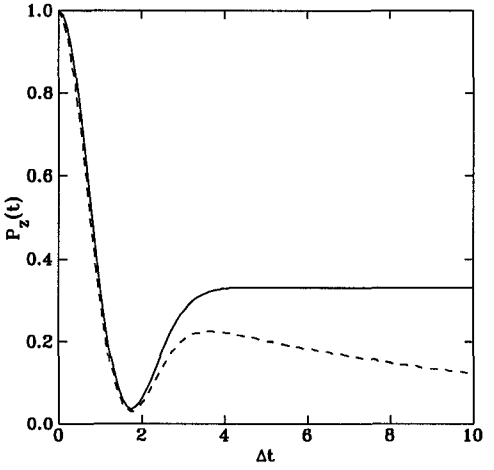

Figure 2.4: The Kubo-Toyabe (KT) function $A_z^{KY}(T)$ given in Eqn. 2.7 (solid line). The combined static KT term with exponential relaxation given in Eqn. 2.9 (dashed line).

yields the famous Kubo-Toyabe[91, 92] (KT) function;

$$A_z^{KT}(t) = \frac{1}{3} + \frac{2}{3}(1 - \Delta^2 t^2) \exp\left(-\frac{1}{2}\Delta^2 t^2\right). \tag{2.7}$$

The KT function has a very distinct line shape as shown in Fig. 2.4. There is a minimum around $\Delta t = \sqrt{3}$, and at late times the KT function saturates at $\frac{1}{3}$, representing the fact that on average $\frac{1}{3}$ of B_{loc} is parallel to the muons polarization and therefore does not cause the muon to precess.

In a real experiment, temporal fluctuations of the local fields causes an exponential dephasing of the muon polarization. The dephasing of the muon polarization is usually accounted for[86, 87] by an exponential relaxation;

$$A_z^{dyn}(t) = A_0 \exp(-\lambda t) \tag{2.8}$$

where λ is an effective relaxation rate. When both static order and dynamic dephasing occurs, the asymmetry is a product of the static KT function, Eqn. 2.7, and the dynamic dephasing term, Eqn. 2.8,

$$A_z(t) = A_z^{KT}(t) \cdot A_z^{dyn}(t). \tag{2.9}$$

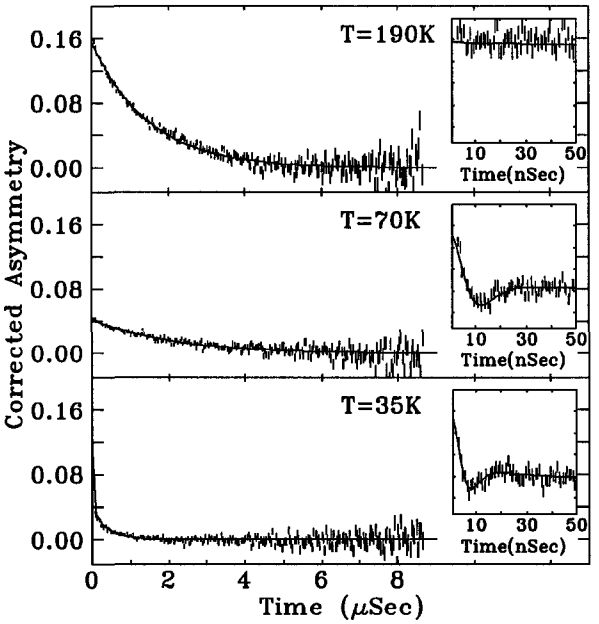

Figure 2.5: Zero field μSR data for a$-(Fe_{0.725}Mn_{0.275})_{78}Si_8B_{14}$ measured above T_C (190 K) showing only exponential relaxation, in the ordered region above T_{xy} (70 K) showing both exponential and K-T contributions, and just below T_{xy} (35 K) showing both contributions but a faster exponential relaxation due to the fluctuations associated with transverse spin freezing. Insets at each temperature show the early-time behavior. Solid lines are fits described in the text.

We emphasize that while this product function gives an excellent description of the time evolution of the muon's asymmetry in our experiments, it is only an approximation[87]. However, when either $\Delta \gg \lambda$ or $\Delta \ll \lambda$, the product function, Eqn. 2.9, is expected[87] to fit the data remarkably well.

A typical exponential decay above T_C, where $\Delta = 0$, is shown in Fig. 2.5 for the a-$(Fe_{1-x}Mn_x)_{78}B_8Si_{14}$ with x=0.275 at T=190 K. Below T_C we observe KT relaxation ($\lambda \sim 0$), as shown in the inset to the 35 K data in Fig. 2.5. The presence of a static component also accounts for the apparent loss of initial asymmetry on cooling through T_C (compare the main curves at 190 K and 70 K in Fig. 2.5) as two thirds of the muon polarization is lost in the first 30 ns. In cases where both static order

and fluctuations are present in zero external field (close to, but below, T_C, and also around T_{xy}), we observe a decay according to Eqn. 2.9.

In the presence of an external magnetic field B along the muon's initial polarization, the KT function is altered. In this case the expression for the distribution of local fields must include B, and Eqn. 2.6 becomes[93]

$$D(B_{loc}) = \left(\frac{\gamma_\mu}{\sqrt{2\pi}}\Delta\right)^3 \exp\left(-\frac{\gamma_\mu^2(B_z - B)^2}{2\Delta^2}\right) \prod_{\alpha=x,y} \exp\left(-\frac{\gamma_\mu^2 B_\alpha^2}{2\Delta^2}\right) \tag{2.10}$$

where again we have $\Delta^2/\gamma_\mu^2 =< B_x^2 >=< B_y^2 >=< B_z^2 >$. Averaging Eqn. 2.4 with the distribution given in Eqn. 2.10 yields a complicated formula[93] for the static relaxation;

$$A_z^{KT}(t) = 1 - \frac{2\Delta^2}{\omega_0^2}(1 - \exp(-\frac{1}{2}\Delta^2 t^2)\cos(\omega_0 t)) + \frac{2\Delta^4}{\omega_0^3}\int_0^t \exp(-\frac{1}{2}\Delta^2\tau^2)\sin(\omega_0\tau)d\tau, \tag{2.11}$$

where $\omega_0 = \gamma_\mu B$. In the limit of late times t, the static asymmetry approaches a value larger than the zero field result $A_z^{KT}(\infty) = \frac{1}{3}$ (see Eqn. 2.7), and with increasing B the late time recovery approaches unity.

In practice, a large magnetic field causes the KT minimum to sharpen and to move to earlier times[44]. The amplitude of the dip (see Fig. 2.4) is also reduced, and in the limit of infinite external field the dip is eliminated entirely. In our experiments, the static KT contribution was only resolved in zero field. In a magnetic field the characteristic dip and recovery occur near or inside our timing window, and could not be reliably resolved. For this reason we only observe the exponential dynamic dephasing of the muon asymmetry. Thus, we have fit our in field μSR data to Eqn. 2.8 only, and have ignored the KT contribution which cannot be resolved.

Zero-field μSR (ZF-μSR) and longitudinal field μSR (LF-μSR) measurements were made on the M20 beamline at TRIUMF. Sample temperature was controlled between 5 K and 300 K in a conventional He-flow cryostat. The magnetic field was set to better than 1 μT using a three-axis flux-gate magnetometer. Longitudinal fields of up to 5.5 T were provided by a superconducting solenoid. Histograms containing

$\sim 4\times 10^7$ events were acquired with a timing resolution of 0.781ns. The relative efficiency of the forward and backwards detectors was determined from the late-time data near T_C where the dynamic relaxation rate is the fastest, and the muons are fully depolarized quite early in the measuring window of ~ 10 μs. Under these conditions, any observed asymmetry between the forward and backward counters reflects unavoidable differences in the detector efficiencies (sensitivity, gain, energy thresholds and geometrical factors are all significant contributors), which can therefore be measured and corrected for. The time dependence of this corrected asymmetry was then fitted using a conventional non-linear least-squares minimization routine.

2.2 a-$(Fe_{1-x}Mn_x)_{78}Si_8B_{14}$: A site frustrated magnetic glass.

2.2.1 Motivation

The alloy a-$(Fe_{1-x}Mn_x)_{78}Si_8B_{14}$ is a well characterized site frustrated magnetic glass which shows both pure spin glass ordering, as well as ferromagnetism. In the range $0.17 < x < 0.31$, spin glass order co-exists transverse to the magnetization below T_{xy}. These conclusions have been reached from bulk magnetization, ac susceptibility, and Mössbauer spectroscopy[23, 24, 61, 62, 63, 64, 65, 66, 67].

However, a recent μSR study[49] limited to a single composition claimed that the peak in the fluctuation rate λ and the increase in static order Δ did not coincide at T_{xy}, and therefore the two signals represent distinct magnetic transitions. The result was interpreted as an experimental observation of the seperate GT and AT lines predicted in the mean field theory of bond frustrated Heisenberg models[28], as discussed in the introduction. In order to check these claims, we have carried out an in depth analysis of ZF-μSR data across the entire phase diagram with *nine* concentrations. Our results indicate that the location of the peak in λ and the location

of the break in slope of Δ coincide[23], in contrast to the claims of others[49]. These two markers of T_{xy} also agree with T_{xy} derived from ac-susceptibility and Mössbauer data, and we find no evidence to support the scenerio where two transitions occur below T_C; there is only one transition at T_{xy}.

In addition, since ^{57}Fe Mössbauer spectroscopy measures the magnetic field at the iron site, which primarily consists of fields contributed by the iron atom, while μSR measures the field at the muon site, which has contributions from all of its magnetic neighbours, these two complementary but different measures of the internal magnetic fields can give insight into the ordering occurring at T_{xy}. In particular, our simulations of site frustrated model[21] show that the ordering is different from bond frustrated models[11]. The ordering which occurs at T_{xy} in site frustrated materials should be predominantly associated with antiferromagnetic Mn moments, while in bond frustrated materials the ordering is uniform. This distinction shows that bond frustrated models are inappropriate for the study of these site frustrated materials.

2.2.2 Experimental methods

Ingots of a-$(Fe_{1-x}Mn_x)_{78}Si_8B_{14}$ were prepared by arc-melting appropriate amounts of the pure elements (Fe 99.97%, Mn 99.99%, Si 99.9999% and B 99.5%) under Ti-gettered argon. These were then melt-spun in 40 kPa helium using a wheel speed of 55 m/s to obtain the metallic glass samples. For $x \leq 0.20$, meter-length ribbons $\sim$1 mm wide were obtained, however as the Mn content increased, the material became increasingly fragile and the ribbons were formed in shorter pieces. By $x = 0.35$, millimeter flakes dominated production. Cu-K_α x-ray diffraction on an automated powder diffractometer was used to confirm the absence of crystalline contamination from all materials used in the measurements presented below. Bulk magnetic characterization (magnetization and ac-susceptibility) was carried out on a commercial extraction magnetometer (Quantum Design PPMS). Data at 5 K in fields of up to 9 T (Fig. 2.6) show the rapid destruction of the magnetization as the Mn content is

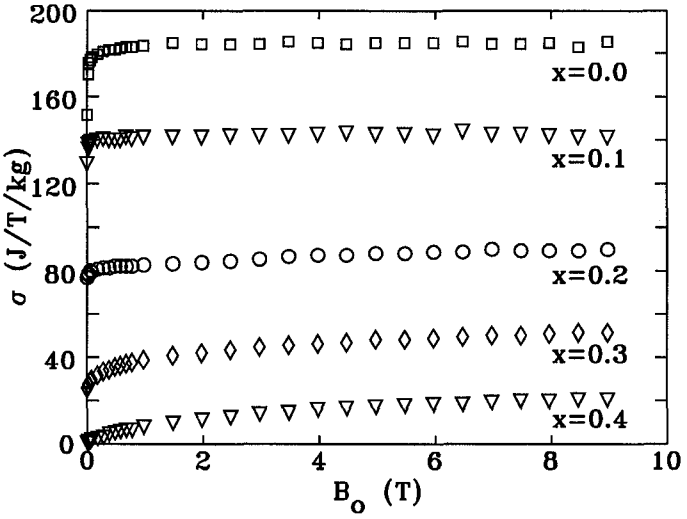

Figure 2.6: Magnetization curves for several representative samples of a-$(Fe_{1-x}Mn_x)_{78}Si_8B_{14}$ measured at 5 K.

increased. Susceptibility measurements in a drive field of 1 mT at 377 Hz were used to follow the rapid decline in T_C that is also caused by the Mn doping. The divergence of the in-phase signal (χ') was used to identify T_C, while a clear peak in the out-of-phase (loss) response (χ'') provided an initial marker for T_{xy}. Some typical data are shown in Fig. 2.7. Ordering temperatures for those alloys with T_C above 290 K ($x \leq 0.2$) were measured using a Perkin-Elmer thermogravimetric analyzer (TGA–7).

Mössbauer measurements were made on a constant acceleration spectrometer with a 1GBq ^{57}Co**Rh** source, calibrated using an $\alpha-$Fe foil. Samples were mounted in a vibration-isolated closed-cycle refrigerator for spectra at temperatures down to 8 K. The spectra were fitted using Window's method[90], as described previously, to obtain average hyperfine fields ($< B_{hf} >$) as a function of temperature. Typical spectra obtained at 8 K are shown in Fig. 2.8. The data shows a rapid destruction of $< B_{hf} >$ at the iron site with increasing Mn content.

For our ZF-μSR measurements, samples with $x \leq 0.15$ consisted of ~15 layers of ribbons clamped between copper rings to give thicknesses of 170–200 mg cm^{-2} over a 16 mm diameter active area. For $x \geq 0.20$, the material was crushed and

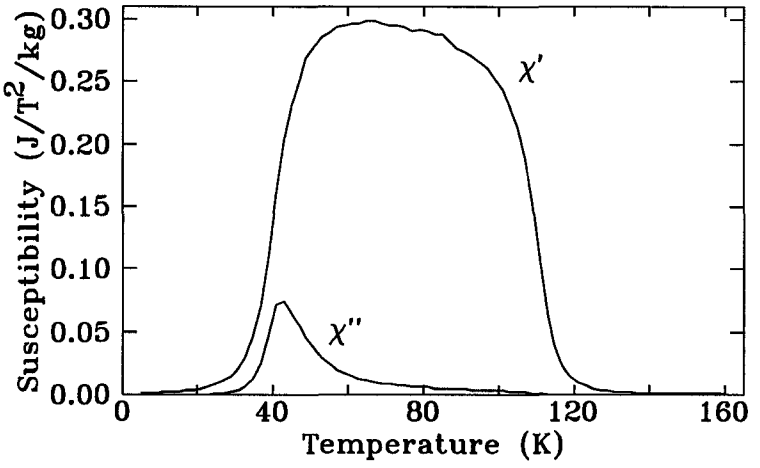

Figure 2.7: AC-susceptibility curves for a$-(Fe_{0.70}Mn_{0.30})_{78}Si_8B_{14}$ showing both the in-phase response (χ') used to obtain T_C and the peak in the out-of-phase signal (χ'') used to determine T_{xy}.

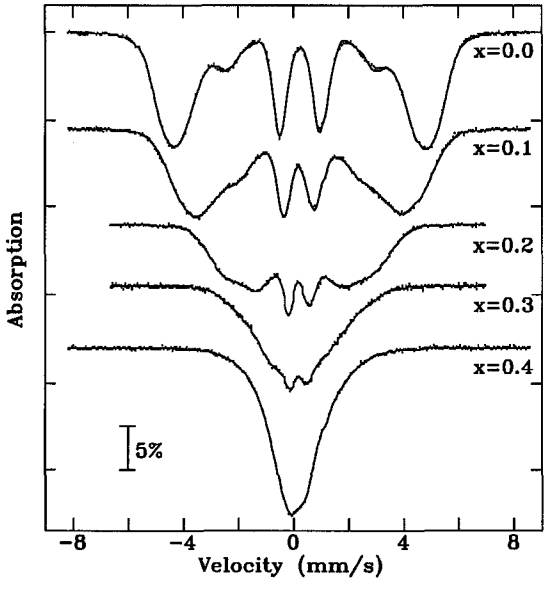

Figure 2.8: ^{57}Fe Mössbauer spectra of several a-$(Fe_{1-x}Mn_x)_{78}Si_8B_{14}$ samples measured at 8 K. Solid lines are fits described in the text.

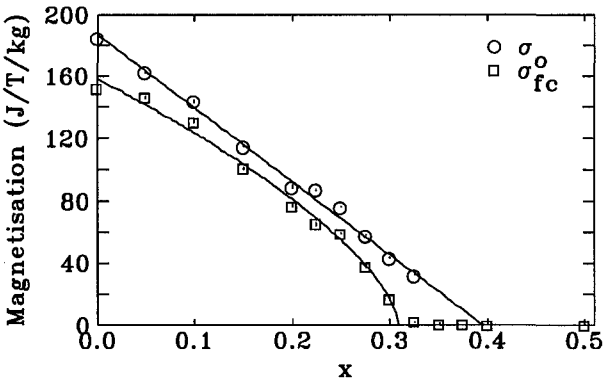

Figure 2.9: Saturation magnetization derived from data in fields of 9 T (○) and field-cooled magnetization (□) obtained by cooling from above T_C to 5 K in a field of 10 mT. The collapse of σ_{fc} suggests that the critical composition for the loss of ferromagnetic order lies at x=0.31. Lines are guides to the eye.

approximately 1 g was mounted between a 99.99% pure silver foil and a 10 μm Kapton sheet within a copper ring. A pure silver (99.99%) mask prevented stray muons from striking any of the mounting hardware.

2.2.3 Results and discussion

Numerical simulations[21, 58, 72] indicate that the initial decline in the magnetization with Mn-doping is due to the ordering of the moments antiparallel to the ferromagnetic iron matrix. Following a procedure used earlier[88], the decline in the saturation magnetization in Fig. 2.9 can be analyzed to yield an average Mn moment of $3.1(1)\mu_B$, consistent with earlier work on this system[88]. Furthermore, the magnetization observed following field cooling to 5 K in 10 mT(Fig. 2.9) also shows a rapid decline with increasing x, going to zero just above x = 0.30. A power-law fits the observed dependence quite well, suggesting that the magnetization tracks an order parameter and that ferromagnetic order is lost entirely at a critical doping level (x_c) of 0.306(6). Beyond this composition, the system is a spin glass.

The temperature dependence of the average hyperfine field (< B_{hf} >(T)) shown

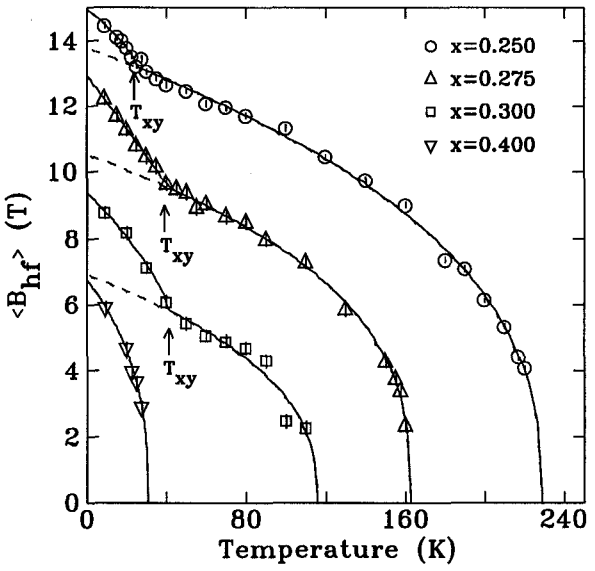

Figure 2.10: Temperature dependence of the average hyperfine field ($< B_{hf} >$(T)) for several a-$(Fe_{1-x}Mn_x)_{78}Si_8B_{14}$ samples around $x_c = 0.31$. The break in slope is a clear marker of the increased static order at T_{xy}. Dotted lines show continuation of fits from above T_{xy}.

in Fig. 2.10 exhibits a clear break in slope at T_{xy} for x = 0.25, 0.275 and 0.30, outside this range T_{xy} is either absent ($x > x_c$, or $x < 0.20$) or the contribution to $< B_{hf} >$ from the transverse spin components is too small to be reliably distinguished by this technique (x = 0.20 and 0.225). This same behavior will be seen later in analyzing the static contribution to the μSR data. The observation of two clear transitions at x = 0.30, and only one at x = 0.325, places x_c between these two concentrations, in full agreement with the estimate derived from analysis of the field-cooled magnetization data. Fitting $< B_{hf} >$(T) to a sum of two power-law functions allows us to extract estimates for T_C and T_{xy}. The density of points used around T_{xy}, and the high statistical quality of the spectra (see Fig. 2.8) are both essential for the T_{xy} estimate to be stable. Remarkably, the values for T_{xy} derived from Mössbauer are in good agreement with those derived from χ'' above (see Fig. 1.6 and Table 2.2), suggesting that the dynamic loss feature seen in the susceptibility is indeed closely associated with the onset of static transverse order. This agreement at three compositions does

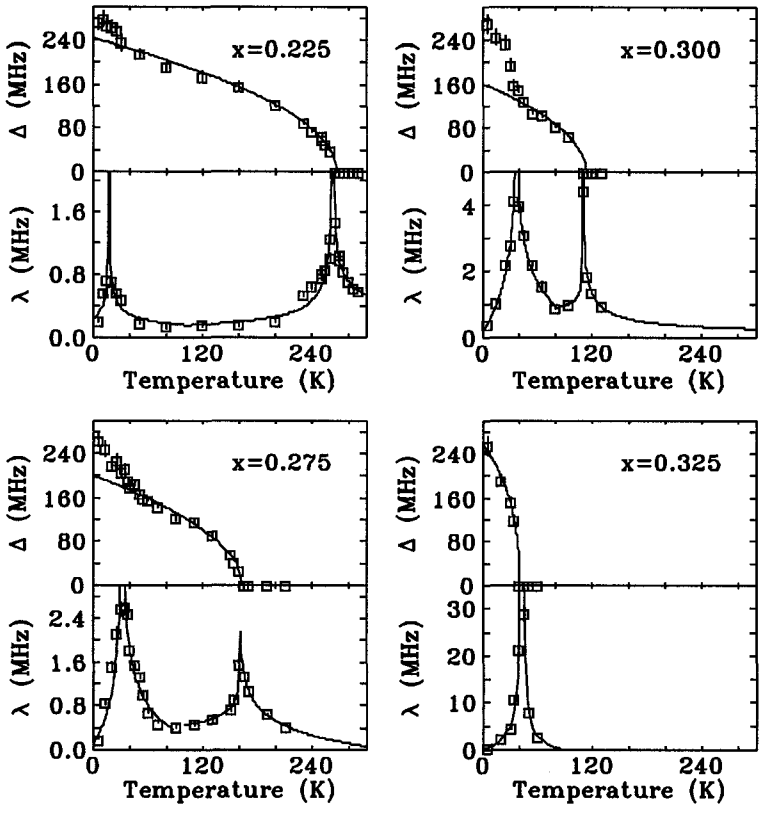

Figure 2.11: Temperature dependence of the static (Δ) and dynamic (λ) signals from ZF-μSR for several a-$(Fe_{1-x}Mn_x)_{78}Si_8B_{14}$ alloys. In every case, the increase in static order (at T_C, T_{xy} or T_{SG}) is associated with a peak in the fluctuation rate. It is important to note though that while the fluctuation rate λ is divergent at T_C, at both T_{SG} and T_{xy} we only observe a Gaussian like peak.

not support the earlier claim of distinct static (T_K) and dynamic (T_F) events below T_C[49].

Fitting the μSR data using Eqn. 2.9 yields the temperature dependences of the static relaxation rate (Δ), a measure of the static field seen by the muons, and the dynamic fluctuation rate (λ) which tracks the fluctuations in the field at the muon sites. These fits are summarized in Fig. 2.11 for four samples. The changeover from two transitions to one clearly occurs between x = 0.30 and x = 0.325, again placing x_c in this range. Only a single transition is seen for the x=0.350 sample as it is beyond x_c

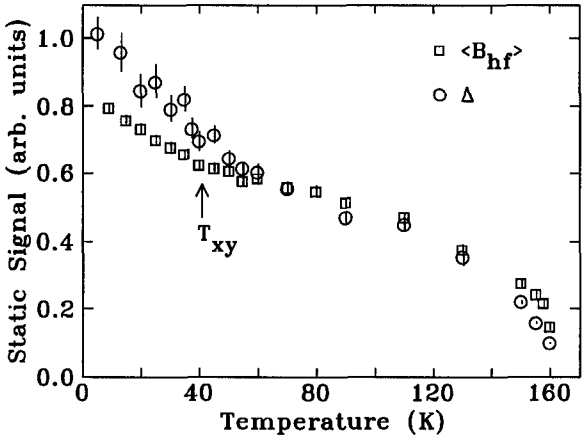

Figure 2.12: Comparison of static order signals from Mössbauer spectroscopy (< B_{hf} >) and ZF-μSR (Δ) for a–$(Fe_{0.725}Mn_{0.275})_{78}Si_8B_{14}$. The data have been normalized to agree above T_{xy} in order to compare the change and signal stability below T_{xy}.

and is therefore a spin glass. The four samples $0.225 \leq x \leq 0.30$ each exhibit two distinct peaks in λ(T). The higher temperature peak is associated with the onset of a non-zero static contribution and thus clearly corresponds to T_C, while the lower peak is aligned with the break in the slope of Δ(T) and therefore marks the freezing of the transverse spin components at T_{xy}. As the Mn content is reduced, the contribution of the transverse spin components to the total ordered moment declines, so that the increase in Δ below T_{xy} becomes difficult to localize reliably. Even with the high density of points apparent in Fig. 2.11, the error on T_{xy} at x=0.225 is about 16 K, however the derived value is fully consistent with the two dynamic determinations. At x = 0.20, only the fluctuation peak at T_{xy} was detected.

Fig. 2.12 shows a direct comparison between $<B_{hf}>$(T) and Δ(T) for a-$(Fe_{0.725}Mn_{0.275})_{78}Si_8B_{14}$ normalized to agree above T_{xy}. Both show a clear increase at T_{xy} confirming that they are each sensitive to the increased static order associated with the freezing of the transverse spin components. While there is a significant rise in < B_{hf} >(T) at T_{xy}, the change in the ZF-μSR data is much larger. This is to

be expected as the Mössbauer measurement is dominated by the effects of the iron moment, while the muons will be affected equally by Mn and Fe moments. Indeed, in the a$-Fe_{90-x}Ru_xZr_{10}$ system[27], where only iron moments are involved in the ordering, $< B_{hf} >$(T) and Δ(T) track together over the whole temperature range. However, the greater sensitivity of the ZF-μSR data comes with increased noise. As a time-domain technique, μSR is at its best in small fields. Large static fields drive the signal into very early times where resolution and timing issues eventually dominate the analysis. These effects are clearly illustrated by the scatter apparent below T_{xy}. By contrast, an energy-domain technique like Mössbauer spectroscopy works better in high fields and yields a more stable, albeit less marked, increase below T_{xy}.

The transition temperatures deduced from the ac-susceptibility data (χ' for T_C, χ'' for T_{xy}), $< B_{hf} >$(T) from Mössbauer spectroscopy, and both Δ and λ from the ZF-μSR data are summarized in the phase diagram shown in Fig. 1.6, and are tabulated in Tables 2.1, 2.2, and 2.3. Manganese doping has a severe effect on the magnetic ordering of this system, driving T_C down from 695 K at x = 0 (inset to Fig. 1.6), to ~40 K at $x_c = 0.31$. A power-law fit to the form expected from the theory of dilute magnetism[94]

$$T_C(x) = a\left(\frac{x_c - x}{x_c}\right)^{\phi} \tag{2.12}$$

does not fit the composition dependence of T_C particularly well, and extrapolating T_C to zero yields a rather poor estimate for the critical composition of $x_c = 0.33 \pm 0.02$. This failure is not unexpected, as the FM–SG boundary is *not* marked by $T_c \rightarrow 0$, but rather by $T_c \rightarrow T_{xy}$. Indeed, a power-law fit to the modified form

$$T_C(x) - T_{xy}(x_c) = a\left(\frac{x_c - x}{x_c}\right)^{\phi} \tag{2.13}$$

is far superior, and yields $x_c = 0.309 \pm 0.004$, in perfect agreement with $x_c = 0.306 \pm 0.006$ derived earlier from field-cooled magnetization data.

The excellent agreement between T_C values derived from χ', Mössbauer spectroscopy and ZF-μSR, coupled with consistent T_{SG} values obtained above x_c, pro-

Table 2.1: Curie temperatures T_C (Kelvin) for a-$(Fe_{1-x}Mn_x)_{78}Si_8B_{14}$ as determined by magnetometry (χ_{AC}), Mössbauer spectroscopy ($< B_{hf} >$), and μSR (Δ and λ). Note that T_C for $x < 0.2$ was determined using a Faraday balance.

x	χ_{AC}	$< B_{hf} >$	Δ	λ
0.000	692(2)	—	—	—
0.050	599(3)	—	—	—
0.100	492(3)	—	—	—
0.150	377(2)	—	—	—
0.200	323(3)	314(12)	—	323(3)
0.225	266(2)	264(1)	266(1)	263(1)
0.250	224(2)	229(1)	227(1)	224(1)
0.275	166(2)	162(1)	163(1)	162(1)
0.300	116(2)	115(8)	110(3)	11591)

vides strong evidence that the analysis and transition assignments are correct and self-consistent. However, it is the behavior at T_{xy} that is the primary focus of this work. Only for x≥0.2 do we see a second transition below T_C, a result that is in full accord with numerical simulations[21, 58, 72]. There is excellent agreement between T_{xy} values derived from the various techniques. For x = 0.275 and 0.300, we have four independent determinations of T_{xy} that agree to better than 5 K. The static, dynamic and loss signatures of T_{xy} are in perfect agreement, with no systematic bias apparent in any of the measurements. While at x = 0.250, static data from Mössbauer, and dynamics from both λ(T) and χ'' are in complete agreement. By x = 0.225, the change in the static order at T_{xy} is too small for its onset to be reliably determined from $< B_{hf} >$(T) and the estimate from Δ(T) exhibits a substantial (~50%) uncertainty. However the ZF-μSR fluctuation peak, and the maximum in the χ'' loss signal are still clear and coincident.

Table 2.2: Transverse spin glass transition temperatures T_{xy} (Kelvin) for a-$(Fe_{1-x}Mn_x)_{78}Si_8B_{14}$ as determined by magnetometry (χ_{AC}), Mössbauer spectroscopy ($< B_{hf} >$), and μSR (Δ and λ).

x	χ_{AC}	$< B_{hf} >$	Δ	λ
0.200	8.4(1)	—	—	11(1)
0.225	11.6(9)	—	33(16)	16(1)
0.250	23.8(2)	24(4)	30(8)	24(1)
0.275	36.8(4)	42(2)	41(3)	32(1)
0.300	43.0(1)	41(5)	36(2)	38(2)

Table 2.3: Transverse spin glass transition temperatures T_{xy} (Kelvin) for a-$(Fe_{1-x}Mn_x)_{78}Si_8B_{14}$ as determined by magnetometry (χ_{AC}), Mössbauer spectroscopy ($< B_{hf} >$), and μSR (Δ and λ).

x	χ_{AC}	$< B_{hf} >$	Δ	λ
0.325	43.1(2)	44(2)	35(5)	43(1)
0.350	36.8(2)	42(2)	44(2)	37(1)
0.375	32.9(2)	37(1)	—	—
0.400	30.5(3)	30(2)	—	—
0.500	29.1(4)	—	—	—

It is important to emphasize that the techniques that have been used to determine T_{xy} with such good agreement probe a very wide range of frequencies: ZF-μSR–Δ ($\sim 10^8$ Hz), $< B_{hf} >$–Mössbauer ($\sim 10^7$ Hz), ZF-μSR–λ ($\sim 10^6$ Hz) and χ'' ($\sim 10^2$ Hz), yet they yield T_{xy} values that agree within a few Kelvin for five samples that exhibit transverse spin freezing transitions at temperatures that change by more than a factor of three. Furthermore, there is no systematic frequency related trend in the T_{xy} values for a given sample. The scatter is random. A separation of T_{xy} into distinct static (T_K) and dynamic (T_F) events can therefore be ruled out. There is no evidence in our data to support the existence of a third transition below T_{xy}.

2.2.4 Conclusions

Zero-field μSR, Mössbauer spectroscopy and ac-susceptibility provide clear evidence of a single transverse spin freezing transition in the site-frustrated a-$(Fe_{1-x}Mn_x)_{78}Si_8B_{14}$ alloy system. We find no evidence for the previously reported mis-match in transition temperatures derived from dynamic and static signatures[49], nor do we see any indication of a third transition below T_C and T_{xy} which could be interpreted as the AT line appearing in the mean field phase diagram of bond frustrated Heisenberg models.

Despite the apparent similarity between the magnetic phase diagram of site frustrated a-$(Fe_{1-x}Mn_x)_{78}Si_8B_{14}$ and related alloys compared to bond frustrated a-$Fe_{90-x}Ru_xZr_{10}$ and related alloys, there does exist one important difference which is seen only by comparing the Mössbauer and μSR data. Below T_C the two signals of static magnetic order, $< B_{hf} >$ and Δ respectively, do *not* track together in these site frustrated materials. By contrast, in the bond frustrated materials the two signals do track together. Since ^{57}Fe Mössbauer spectroscopy tracks the field at the ^{57}Fe site and μSR tracks the average field at the muon site, one expects the two signals to track together if the magnetic order is uniform and not site specific. The fact that the increase in static order observed at T_{xy} as measured by the muons is larger than

that observed in Mössbauer spectroscopy in the site frustrated materials indicates that the ordering at T_{xy} is predominantly associated with Mn moments.

An interesting similarity does exist between site and bond frustrated materials; the peak in λ at T_C are very different from the peaks seen at both T_{xy} and T_{SG}. At T_C, the peak in λ is seen to diverge in bond frustrated materials while at T_{xy} and T_C only a broad maximum is observed[26, 27]. The same behavior is found by us for this site frustrated material[23]. One possible explanation for the non-divergent peak at T_{SG} and T_{xy}, first discussed in the context of the bond frustrated Heisenberg spin glass model, is that while there exists a finite temperature transition at T_{xy}[11] and T_{SG}[7, 8, 9, 10, 11], the transition may be of the Kosterlitz-Thouless (KT) type[8, 9]. The lack of a divergent peak at T_{SG} and T_{xy} may be related to the existence of this suggested KT like transition. However, since this ordering scenario cannot yet be confirmed for bond frustrated Heisenberg models[9], and since spin glass ordering in site frustrated Heisenberg models has yet to be observed, Monte Carlo data which could clarify the situation does not yet exist.

2.3 a-$Fe_{100-x}Zr_x$: a bond frustrated magnetic glass

2.3.1 Motivation

The phase diagram of a-$Fe_{100-x}Zr_x$ shown in Fig. 1.8 is typical of many partially frustrated magnetic systems. The transition at T_{xy} marks the onset of static spin glass order in the plane perpendicular to the ferromagnetic order[26]. While the ordering is in excellent agreement with 3d bond frustrated models, other models have been proposed to account for the observed phase diagram such as ferromagnetic clusters in a ferromagnetic matrix[32, 33, 34, 35, 36, 37, 38, 39] and antiferromagnetic clusters in a ferromagnetic matrix[29, 30, 31]. However, our Monte Carlo simulations of the site frustrated model show that none of these models can produce the phase diagram observed. For small concentrations of antiferromagnetic sites in the site

frustrated model, there exists finite antiferromagnetic clusters in a ferromagnetic matrix, consistent with a model of finite AF clusters in a FM matrix. Yet these finite AF clusters do not freeze[21] nor do they destroy the FM order. The second proposed model, finite FM clusters coupled to the FM matrix with frustrated ferromagnetic and antiferromagnetic bonds, is identical to the finite AF clusters coupled to a FM matrix model through a gauge transformation, as we shall discuss in Chapter 4. Therefore, this model cannot describe the ordering observed in the material either.

While the zero field phase diagram of bond frustrated materials and models are qualitatively similar (compare Fig. 1.3 and Fig. 5.1), it is not possible to quantitatively map the $x - T$ phase diagram of the simple model onto the $x - T$ phase diagram of the complex material. This is due in part to the unknown distribution of bonds and frustration in the material, but which are exactly known, and fixed, in the model. The inability to map the phase diagrams of the materials and models onto one another is also due in part to the unknown mapping of T_C, T_{SG} and T_{xy} found for our classical Heisenberg models onto those of real materials. To gain further evidence that the bond frustrated model is a good description of the magnetic ordering which takes place in the material we have measured the field dependence of T_{xy}. We do this with the expectation that the response of T_{xy} to a magnetic field should be a characteristic of the material, which can then be compared with our Monte Carlo simulations of the $\pm$J bond frustrated Heisenberg model. We find that the field dependence of T_{xy} does not agree with any of the mean field results, and instead is described by the simple equation

$$T_{xy}(B) = T_{xy}(0)\left(1 - \frac{B}{B+J}\right) \tag{2.14}$$

over a range of external fields $0 \leq$B$< 5\ T$. As will be shown in Chapter 5, the same behavior is observed for the model. This agreement provides strong evidence that the correct interpretation of the experimental results is that a-$Fe_{100-x}Zr_x$ is a realization of a bond frustrated Heisenberg magnet.

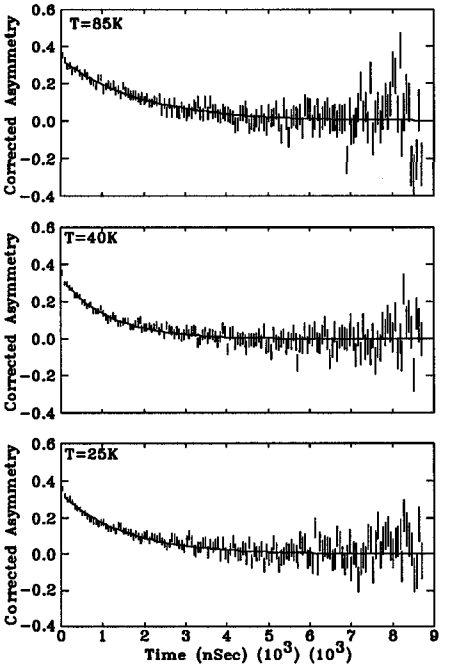

Figure 2.13: A plot showing the exponential loss of asymmetry for a-$Fe_{93}Zr_7$ in a field of 3.75 T for $T > T_{xy}$ (top), $T \sim T_{xy}$ (middle) and $T < T_{xy}$ (bottom).

2.3.2 Results and discussion

In zero external magnetic field, both T_C and T_{xy} are observable in μSR data by a peak in the fluctuation rate λ which coincides with the increase in static order Δ seen at the muon site[23, 26, 27]. The peak in λ at T_C is apparently divergent, while that at T_{xy} is well described by a Gaussian[26]. Applying an external magnetic field suppresses the height of the peak in λ and moves it to lower temperatures. We no longer resolve the KT-like dip associated with the static order at even moderate fields (B>1 T) and so we only fit the exponential dephasing of the muons polarization. Typical exponential decays are shown in Fig. 2.13.

Our results from fitting the observed asymmetry to Eqn. 2.8 are shown in Fig. 2.14 for a-$Fe_{93}Zr_7$. The suppression of the peak in λ is clear with increasing field, as well as the shift in location to lower temperatures. The lowering of the peak height with increasing field strength is known as LF-decoupling, and can readily be understood

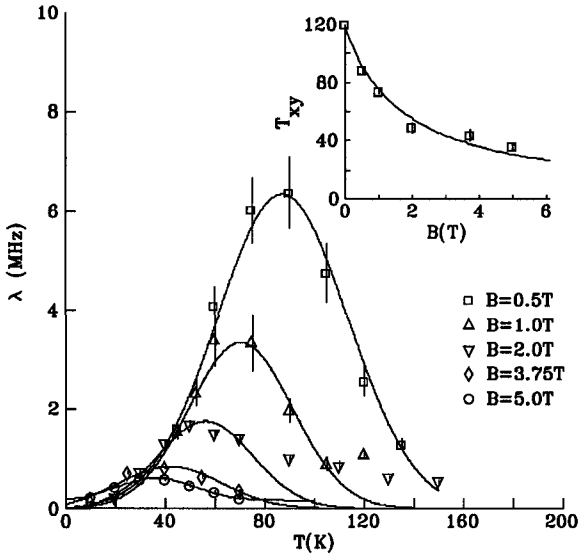

Figure 2.14: Dynamical fluctuation rate λ vs. temperature for different fields for a-$Fe_{93}Zr_7$. The inset shows the 1/B scaling of the transition temperature $T_{xy}(B)$ according to Eqn. 2.14.

as follows[95]: The applied field adds vectorially to the internal fields, and when the applied field becomes much larger than the internal field, the latter no longer have any effect. For intermediate cases, the fluctuations have a diminishing effect with increasing applied field strength since with increasing fields it becomes more difficult for the fluctuations to alter the direction of the net field.

The shift in location of the peak is plotted in the inset to Fig. 2.14 along with a fit to equation Eqn. 2.14. This is the same data which appeared in Fig. 1.5, and so we do not include the fits to the AT or GT form. As already noted, Eqn. 2.14 fits the data remarkably well.

The same effect, a reduction in T_{xy} with an increase in B, is found across the entire range of concentrations studied. The resulting curves can all be analyzed using the same functional form given in Eqn. 2.14. In Fig. 2.15 we show plots of the fitted field dependence of T_{xy} against B for the four concentrations of a-$Fe_{100-x}Zr_x$ studied, with x =7, 8, 9 and 10. All of the data shown in Fig. 2.15 are consistent with

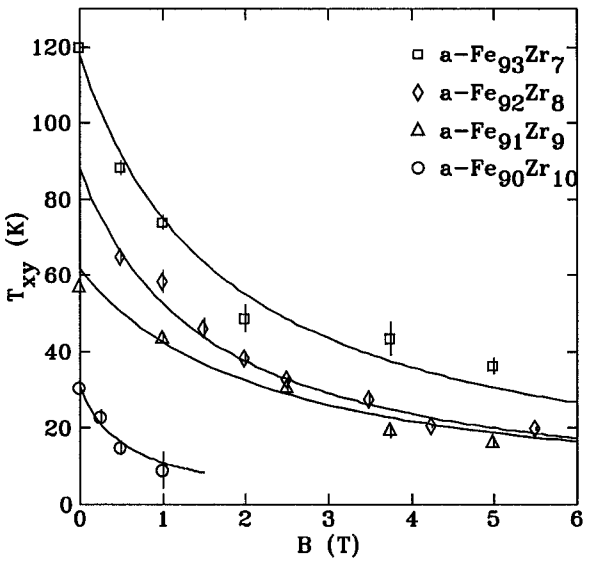

Figure 2.15: The decrease of T_{xy} with increasing B for a-$Fe_{100-x}Zr_x$ for four concentrations with x =7,8,9 and 10. All four sets of data are fitted to Eqn. 2.14.

a 1/B reduction in T_{xy} and cannot be fitted to any of the mean field expressions, in particular Eqn. 1.1, Eqn. 1.2, or the limiting high field behavior Eqn. 1.3. The consistency in behavior for four different concentrations demonstrates the occurrence of a 1/B reduction of T_{xy}.

2.3.3 Conclusions

By performing longitudinal field μSR we find that T_{xy} is reduced in a magnetic field. A reduction of T_{xy} with increasing B is expected since a magnetic field favors ferromagnetic order which will come at the expense of transverse spin glass order. Mean field theory predicts a reduction of T_{xy} which does not agree with our experiments. Instead, we find that for four different samples, measured over a broad range of fields which reduce T_{xy} by a factor of four, that T_{xy} is consistent with Eqn. 2.14.

Chapter 3

Monte Carlo Methods

In this chapter we provide details of the Monte Carlo method we have used to determine the phase diagrams for the three dimensional, nearest neighbor, site and bond frustrated Heisenberg models defined in the introduction. We first give a brief introduction of the Monte Carlo method as applied to classical spin models with Hamiltonians of the type given in Eqn. 1.6 and Eqn. 1.10. Our description of the Monte Carlo method is only brief, as the method is explained in great detail elsewhere, and we refer the reader to these titles (see Ref. [96] and Ref. [97]). We then discuss our Monte Carlo simulation methodology for the site frustrated model, and the observables we measure in order to construct the phase diagrams given in Chapter 4. In the next section we discuss our Monte Carlo simulation methodology for the bond frustrated model, and the observables we measure in order to construct the phase diagrams given in Chapter 5. In the last section we provide a brief description of standard finite size scaling techniques used to obtain the phase diagrams in the thermodynamic limit.

3.1 The Monte Carlo Method

Statistical mechanics is a branch of physics in which system with many degrees of freedom are treated at a statistical level. The framework allows thermodynamic densities to be calculated. For an equilibrium canonical ensemble, the probability of a classical system existing in some state n is proportional to the Gibbs measure

$$P_n = \exp(-\beta E_n)/\sum_n \exp(-\beta E_n) \tag{3.1}$$

where the energy E_n is the value taken by the Hamiltonian in state n, $\beta = 1/T$ the inverse temperature, and the denominator $Z = \sum_n \exp(-\beta E_n)$ is the partition function. The thermal average of an observable X, $< X >$, is then given by the average of X over all n states of the system

$$< X >= \sum_n X_n \exp(-\beta E_n)/\sum_n \exp(-\beta E_n). \tag{3.2}$$

The average can be written in a number of different ways. For instance, rather than summing over all states we could sum over all energies

$$< X >= \sum_E \overline{X(E)} g(E) \exp(-\beta E)/\sum_E g(E) \exp(-\beta E) \tag{3.3}$$

where $\overline{X(E)}$ is the average value of the observable X with energy E and $g(E)$ is the number of states with energy E. For a model with a continuum of energy states the sum becomes an integral:

$$< X >= \int_{E_{min}}^{E_{max}} g(E)\overline{X(E)} \exp(-\beta E)/\int_{E_{min}}^{E_{max}} g(E) \exp(-\beta E). \tag{3.4}$$

For many interesting problems in statistical physics the averages cannot be calculated in closed form. A variety of techniques have been developed to determine approximate solutions for thermodynamic densities, such as series expansions and the renormalization group. However, for the types of models we consider in this thesis, the best results have been obtained using the widely popular simulation technique known as the Monte Carlo method.

In a typical Monte Carlo simulation, states of the system are accessed sequentially with a probability such that the thermal average in Eqn. 3.2 may be replaced by a time average over the length of the simulation. In particular, for an importance sampling Monte Carlo algorithm we have

$$< X >= \frac{1}{M} \sum_{n=1}^{M} X_n \tag{3.5}$$

where the state n is determined from the state at $n-1$ in a predetermined way. To determine the probability of state n, importance sampling utilizes the master equation

$$\frac{\partial P_n(t)}{\partial t} = -\sum_{m \neq n} [P_n(t) W_{n \to m} - P_m(t) W_{m \to n}] \tag{3.6}$$

where P_n is the probability of being in state n at time t and $W_{n \to m}$ is the transition probability from state n to state m. Since in equilibrium we have $\frac{\partial P_n(t)}{\partial t} = 0$, we arrive at the celebrated detailed balance condition:

$$P_n(t) W_{n \to m} = P_m(t) W_{m \to m} \tag{3.7}$$

In order that the detailed balance condition produce the correct probability, Eqn. 3.1, without knowledge of the partition function we generate a new state from the old state with a probability that satisfies Eqn. 3.7. In the case of the Metropolis Monte Carlo method we choose

$$W_{n \to m} = \exp(\beta(E_m - E_n)) \qquad E_n > E_m \tag{3.8}$$

$$W_{n \to m} = 1 \qquad E_n < E_m \tag{3.9}$$

which ensures that the states of the system are chosen according to Eqn. 3.1.

A typical importance sampling Metropolis Monte Carlo method proceeds as follows: (1) The initial state of the system is chosen at random; (2) All of the spins in the system are sequentially updated (in a random order) with the probability of the update chosen according to Eqn. 3.9 at some temperature T; (3) Observables are measured and the updating proceeds from (2). One attempted update for each

lattice site, chosen at random, comprises one elementary Monte Carlo step (MCS). Average values are then obtained according to Eqn. 3.5. However, since the initial random state of the system will not be representative of a finite temperature state, a simulation carried out at a finite temperature will have to run through many equilibration steps (EQS's) prior to carrying out the thermal average in order to achieve an equilibrated state. A practical technique used here is to start at high temperatures and anneal towards low temperatures (simulated annealing).

Since the new state is determined from the old state, the new state will remain correlated with the previous state over a period of time. The number of MCS's required to generate a state uncorrelated with the previous state is known as the sample independence time[96, 98, 99]. The correlation time for a particular observable is determined from the autocorrelation function of that observable; the autocorrelation function of observable X is

$$A_X(t) = \frac{< X(t_0)X(t_0+t) > - < X(t_0) >^2}{< X^2(t_0) > - < X(t_0) >^2} \tag{3.10}$$

where $<\quad>$ represents an average over times t_0 (a thermal average). The normalization is chosen such that at $t = 0$, $A_X = 1$ while at long times $A_X(t \rightarrow \infty) = 0$. The sample independence time, τ, is given by twice the integrated autocorrelation time[98, 99] (twice the area under Eqn. 3.10). For a discrete time series evolving under stochastic dynamics, like Eqn. 3.10 determined using a Metropolis Monte Carlo algorithm, the $< A_X(t) >$ decays are given by a discrete sum of exponentials[16, 98, 99]:

$$A_X(t) = \sum_i a_i \exp(-w_i t) \tag{3.11}$$

where $w_i = 1/\tau_i$. In this case, the sample independence time is given by $\tau = \sum_i a_i \tau_i$. Typically, between two and four exponential are required to fit the autocorrelation functions presented here.

The largest τ_i is the asymptotic correlation time τ_a. τ_a is expected to diverge at a second order phase transition[96, 99] like $\tau_a \sim L^z$, where L is the linear dimension of

the system and z is a dynamical critical exponent. Equivalently, one has the standard critical slowing down associated with second order phase transitions, $\tau_a \sim t^{-z\nu}$ with $t = \frac{T-T_C}{T_C}$ the reduced temperature and ν the exponent of the correlation length. Of course, the value of z taken in a Monte Carlo simulation will depend on the particular algorithm used.

3.2 Methods and Observables for the site frustrated model

3.2.1 Monte Carlo methods for the site frustrated model

Our study of the site frustrated Heisenberg model has proceeded in two parts. In the first, we have employed a simple Metropolis Monte Carlo algorithm with simulated annealing to obtain the phase diagrams shown in Figs. 4.1 and 4.2. The system sizes studied range from $4 \leq L \leq 16$ (sc), from $4 \leq L \leq 14$ (bcc) and from $4 \leq L \leq 12$ (fcc) for the concentrations shown in the phase diagrams by open symbols. The range of system sizes for sc lattices are the same as those used in Ref. 11 and Ref. 12. For the sc and bcc lattices with J_{FA}=0 (Fig. 4.2(a) and Fig. 4.2(b)), only $x \leq 0.5$ were studied and $T_{C,N}(x>0.5)$ are obtained by symmetry. The number of Monte Carlo updates per lattice site (MCS) ranged from 5×10^3 to 5×10^6 after discarding the first 5×10^3 to 5×10^4 MCS at each T to ensure equilibration. The number of MCS is chosen such that we exceed the measured sample independence time by orders of magnitude. The large value of τ experienced when approaching $T_{C,N}$ limits the lattice sizes and the number of disorder configurations studied. In this initial survey, a minimum of 16 realizations of disorder were used to obtain configurational averages.

In order to increase L, and the number of configurations C, we must reduce τ. To do so, we have employed an over-relaxation scheme[100], where the spins evolve

according to

$$\vec{S}_i \rightarrow 2\frac{\vec{S}_i \cdot \vec{B}_i}{\vec{B}_i \cdot \vec{B}_i}\vec{B}_i - \vec{S}_i, \tag{3.12}$$

where $\vec{B}_i = \sum_j J_{ij}\vec{S}_j$ is the internal field experienced at site i due to the coupling with nearest neighbor spins $\vec{S}_j$. The effect of the over-relaxation update is to rotate the spin at site i about the field experienced at the site. Since Eqn. 3.12 leaves the energy of the system invariant, it is always a valid Metropolis Monte Carlo update. Following each Metropolis MCS we use five over-relaxation MCS's, which then comprises a single OR-MCS. The OR-MCS update has reduced τ by about a factor of 100. However, there remains a divergence of τ according to $\tau \sim L^z$ with z unaltered from the value found using only Metropolis dynamics ($z \sim 0$, $z \sim 2$, and $z \sim 3$ for $T \gg T_C$, $T \sim T_C$ and $T \ll T_C$ respectively). Over-relaxation has been found useful in studies of the site frustrated Heisenberg model[59], the bond frustrated Heisenberg model[8, 9, 11, 101] and fcc Heisenberg antiferromagnets[102].

The dramatic reduction in τ which occurs when employing the over-relaxation update is illustrated in Fig. 3.1 where we have plotted the autocorrelation function of the magnetization near T_C for MCS and OR-MCS updates. The autocorrelation function of the magnetization or staggered magnetization ($A_f(t)$ and $A_{st}(t)$ respectively) at time t is given by

$$A_{f,st}(t) = \frac{[< m_{f,st}(t_0)m_{f,st}(t_0+t) >] - [< m_{f,st} >]^2}{[< m_{f,st}^2 >] - [< m_{f,st} >]^2}, \tag{3.13}$$

where [ ] represents an average over the random distribution of sites (m_f and m_{st} are defined below) and $<\quad>$ represents a time (thermal) average. The derived integrated autocorrelation time is shown in the inset of Fig. 3.1 for $T \sim T_C$ using the OR-MCS update. (In passing, we note that the actual time dependent signal measured, $[< m_{f,st}(t_0)m_{f,st}(t_0+t) >]$, has the property that at $t = 0$ it reduces to the static measure $[< m^2 >]$, which is proportional to the disconnected susceptibility $\chi^d_{f,st}$, while at $t \rightarrow \infty$ it reduces to $[< m >]^2$, the square of the magnetization. The difference, $[< m_{f,st}^2 >] - [< m_{f,st} >]^2$ is proportional to the connected susceptibility

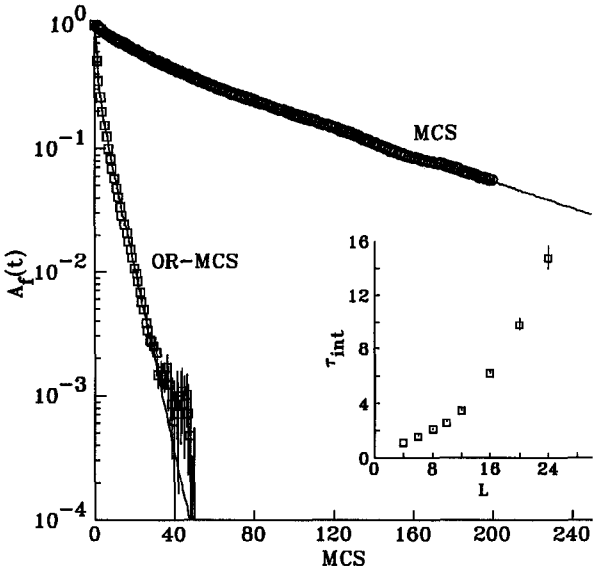

Figure 3.1: Autocorrelation function for the magnetization $A_f(t)$ (Eqn. 3.13) using Metropolis (MCS) and Metropolis plus over-relaxation (OR-MCS) dynamics for $T \sim T_C$ ($L = 10$, $x = 0.45$ for the sc lattice). The inset shows the integrated integrated autocorrelation time at $T = 0.95$ ($T \sim T_C$) using over-relaxation plus Metropolis dynamics.

$\chi^c_{f,st}$. Therefore, the magnetization and susceptibilities can be determined entirely by measuring time dependent autocorrelation functions.)

The OR-MCS update has enabled us to equilibrate larger sc lattices with $4 \leq L \leq 24$. The number of configurations used at each x and L is listed in Table 3.1. The number of OR-MCS used here ranges from 5×10^2 at high temperatures to 5×10^4 at low temperatures, after discarding between 5×10^2 to 5×10^3 OR-MCS to ensure equilibration. Again, the number of OR-MCS is chosen to be much larger than any measured sample independence time.

Two characteristics of the $A_{f,st}(t)$ decays have been extensively checked to ensure that our results are both equilibrated and representative of the limit $t \to \infty$. Equilibrium requires that the $A_{f,st}(t)$ decays are independent of the origin of time. For selected concentrations and temperatures we have verified that the decays are repeatable, and thus equilibrated, by measuring $A_{f,st}(t)$ while varying the number

Table 3.1: Number of disorder configurations (C) used for each concentration (x) and system size (L) for sc lattices using the OR-MCS Monte Carlo update as explained in the text.

L	x =0.10	0.20	0.30	0.35	0.40	0.45	0.49	0.50
4	200	200	200	200	200	1600	1600	1600
6	200	200	200	200	200	872	592	962
8	200	200	200	200	200	976	800	560
10	200	200	200	200	200	976	403	520
12	200	200	200	200	200	744	208	728
16	200	200	200	200	200	400	240	299
20	200	200	200	200	200	400	240	286
24	256	244	224	184	208	288	234	240

of discarded MCS's (or OR-MCS's) prior to the measurement. Indeed, accurate measurement of $A_{f,st}(t)$ requires that the number of MCS's exceeds τ by orders of magnitude which essentially guarantees this result. To ensure our results are equilibrated at each temperature we discard several τ's worth of MCS's (or OR-MCS's) prior to our measurements.

Second, to check that our results are representative of the long time limit, we have compared our results when varying the numbers of MCS's or OR-MCS's updates. The $A_{f,st}(t)$ decays provide a measure of τ for the *scalar* quantity $m_{f,st}$ while our demonstration, presented later, that the FM and AF order are mutually perpendicular requires us to exceed τ for the *vector* quantities $\vec{m}_{f,st}$. Since τ for vector order parameters is much larger than for scalar order parameters, the long times necessary to demonstrate that the FM order and AF order are perpendicular also allows us to compare $m_{f,st}$ measured in typical simulations (with $\sim 5 \times 10^4$ MCS's) to that measured in a very long and atypical simulation (with $\sim 5 \times 10^6$ MCS's). The

comparison confirms that exceeding τ by orders of magnitude yields results that are characteristic of the limit $t \rightarrow \infty$.

3.2.2 Observables for the site frustrated model

The most important quantities we measure are powers of the finite lattice magnetization and staggered magnetization. At time t, the instantaneous values of the n^{th} power of the magnetization or staggered magnetization, m_f and m_{st}, are

$$\begin{aligned} m^n_{f,st} &= ((N^{-1}\sum_i L^i_{f,st}S^x_i)^2 + (N^{-1}\sum_i L^i_{f,st}S^y_i)^2 \\ &\quad + (N^{-1}\sum_i L^i_{f,st}S^z_i)^2)^{n/2} \end{aligned} \tag{3.14}$$

where x, y, z denote Cartesian components and $L^i_{f,st}$ is an operator with the symmetry of the ferromagnetic or antiferromagnetic state. We have not made an attempt to measure the AF order for the fcc lattice, which is more complex than the AF order in bipartite lattices[20, 102, 103, 104, 105]. Average values are obtained by averaging over time $< >$ and disorder $[\ ]$ to yield $[< m^n_f >]$ and $[< m^n_{st} >]$. For brevity, we will henceforth refer to $[< m_{f,st} >]$ as $m_{f,st}$ with the understanding that averages over time and disorder have been taken.

Other quantities of interest are the connected ferromagnetic and antiferromagnetic susceptibilities, χ^c_f and χ^c_{st}, given by

$$\chi^c_{f,st} = N\beta[< m^2_{f,st} > - < m_{f,st} >^2] \tag{3.15}$$

which exhibits a peak at a size dependent pseudo-transition temperature $T_{C,N}(L)$, and is therefore useful for determining the real transition temperature using finite size scaling techniques described later. We also measure the disconnected ferromagnetic and antiferromagnetic susceptibilities, χ^d_f and χ^d_{st}, given by

$$\chi^d_{f,st} = N\beta[< m^2_{f,st} >]. \tag{3.16}$$

The disconnected susceptibility has the same scaling behavior as the connected susceptibility, but does not display a peak. We have also measured the Binder cumulant for the ferromagnetic and antiferromagnetic state, $B_{f,st}$, given by

$$B_{f,st} = \frac{1}{2}(5 - 3\frac{[< m_{f,st}^4 >]}{[< m_{f,st}^2 >]^2}) \tag{3.17}$$

which is helpful in locating T_C and T_N. The normalization is chosen such that $B_{f,st}$=0 at T=∞ and, in the case of the pure (x=0, 1) models, $B_{f,st}$=1 at T=0.

3.3 Methods and Observables for the bond frustrated model

3.3.1 Monte Carlo methods for the bond frustrated model

To determine the phase diagram of the bond frustrated model we have[11] studied the model using the same hybrid Monte Carlo algorithm that combines Metropolis with over-relaxation techniques. For the simulations performed in a magnetic field, we must include the external field in the calculation of the internal field B_i appearing in Eqn. 3.12. We begin each simulation in the paramagnetic state where the sample independence times are of the order unity and anneal towards low temperatures. Following each Metropolis Monte Carlo update (one attempted spin update/lattice site) we use five over-relaxation updates which again comprises a single Monte Carlo step (OR-MCS).

The correlation times for the magnetization at $x = 0.15$ are shown in Fig. 3.2 for both the Metropolis algorithm with and without over-relaxation. At this concentration of antiferromagnetic bonds, the model is ferromagnetic below $T_C = 0.601(3)T_C(x = 0)$ with transverse spin glass order below $T_{xy} = 0.216(6)$ (see Fig. 5.1). We have measured the correlation times for both the vector quantity $\vec{m}_f$ and the scalar m. Autocorrelation functions for the scalar magnetization calculated using our hybrid

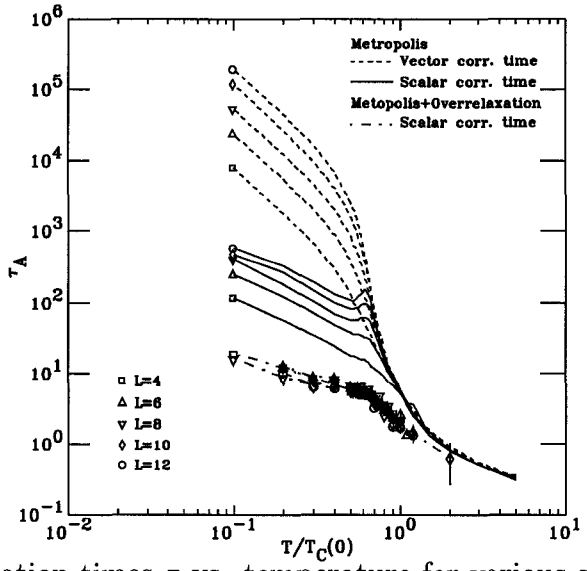

Figure 3.2: Correlation times τ vs. temperature for various small system sizes using both the Metropolis algorithm and a hybrid algorithm as discussed in the text for the bond frustrated Heisenberg model at $x = 0.15$.

algorithm are shown in Fig. 3.3 for temperatures above, near, and below T_C. Using the conventional Metropolis algorithm we find that for $T \gg T_C$, τ_A is a constant of the order one for both the scalar and vector quantities. At T_C $\tau_A \sim L^z$, with $z \sim 2$ as found for the pure Heisenberg model[99]. For $T \ll T_C$ we find that $\tau_A \sim L^3$. Below T_C the vector quantity magnetization $\vec{m}$ relaxes much slower than the scalar magnetization m. There is a peak in τ_A for the scalar magnetization which is associated with the ferromagnetic ordering which takes place at T_C, and which emerges with increasing L. This dynamical relaxation peak can loosely be associated with the peak in the muon spin relaxation rate occurring at T_C in our μSR experiments.

The use of over-relaxation has a much more dramatic effect on the correlation times for the bond frustrated model than for the site frustrated model. As shown in Fig. 3.2, over-relaxation appears to completely eliminate the critical slowing down for the scalar quantity, and makes τ_A independent of L except at the lowest temperatures.

The correlation time for the vector quantity $\vec{m}$ is not shown in Fig. 3.2 when using over-relaxation as the relaxation is too fast to be interesting. Since the Hamiltonian

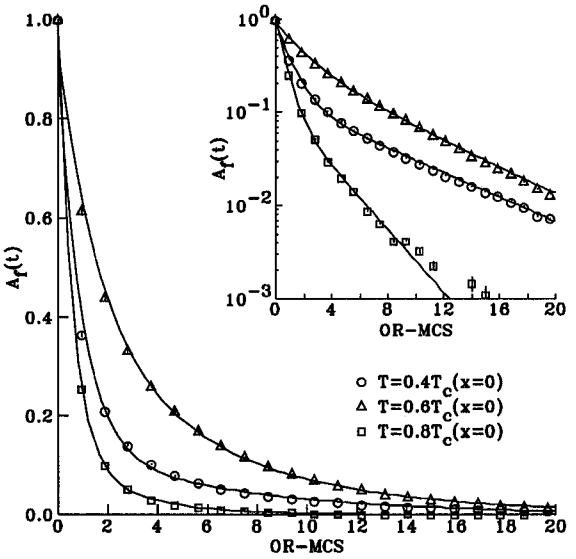

Figure 3.3: Autocorrelation functions for the magnetization $A_f(t)$ (Eqn. 3.13) for the bond frustrated model with a concentration x=0.15, and where $T_C \sim 0.6T_C(x = 0)$. $A_f(t)$ is shown for temperatures below T_C ($T = 0.4T_C(x = 0)$), near T_C ($T = 0.6T_C(x = 0)$), and above T_C ($T = 0.8T_C(x = 0)$).

in zero field is rotationally invariant, $< \vec{m} >= 0$ for an ergodic simulation. The Metropolis algorithm acting alone requires huge numbers of MCS's in order to observe $< \vec{m} >= 0$ because following every MCS the magnetization is only rotated by a small amount. Over-relaxation, by contrast, rotates every spin by the largest amount possible with respect to the field acting at the site. Consequently, over-relaxation also rotates the magnetization quickly producing $< \vec{m} >= 0$ in short simulation times. For this reason we have not endeavored to measure the correlation time for this quantity.

To determine the paramagnetic to ferromagnetic phase boundary for the bond frustrated Heisenberg model, we have proceeded in two steps. First, the phase boundary was determined approximately from the scaling of the peak location of χ_f^c and the maximum slope of B_f using $4 \leq L \leq 20$ and between 16 and 100 bond configurations. We then proceeded to determine the phase boundary using a different method, namely the crossing of the ξ/L curves (ξ is the correlation length to be defined below). To determine the ferromagnetic correlation length, we have used 500

independent bond configurations ([ ]) and a maximum of 4×10^4 OR-MCS, chosen to correspond to $\sim$ 500 independent thermal (< >) configurations, after discarding enough OR-MCS's to ensure equilibration, typically 1000 OR-MCS's.

In the case of spin glass order, we have not made measurements of the various autocorrelation functions. The reason for this omission is that accurate measurements of the autocorrelation functions for a particular observable is in fact more difficult than measuring the observable itself. For spin glasses, the observables used to determine the phase diagram are much more difficult to measure than, for example, the scalar magnetization. As such, it is simply not practical to determine sample independence times and asymptotic correlation times for the most important spin glass quantities we measure, namely the spin glass correlation length, given current computing facilities. Our results though indicate that the sample independence times are not prohibitively large, except at very low temperatures where it is obvious we have fallen out of equilibrium.

To verify that our measurements of spin glass observables are in equilibrium for each choice (T,L,x) we have calculated thermal and bond averages with a logarithmically increasing numbers of OR-MCS's, after discarding the same number of OR-MCS's prior to the average. If we exceed the relevant sample independence time by orders of magnitude, we expect that observables will be independent of the number of OR-MCS's. In the spin glass regime of the phase diagram we have used between 300 and 10^5 OR-MCS's to compute thermal averages (<>), followed by 100 bond configurations to compute disorder averages ([ ]). In the ferromagnetic regime we have used between 300 and 10^4 OR-MCS's for thermal averaging and 500 bond configurations for disorder averaging. The bond configurations were chosen independently for each choice of the number of Monte Carlo steps giving a total 400 to 600 bond configurations for $x > 0.2$ (paramagnetic to spin glass phase boundary) and 2000 bond configurations for $x \leq 0.2$ (ferromagnetic to spin glass phase boundary).

After having determined the zero field phase diagram, we have measured T_{xy} as a

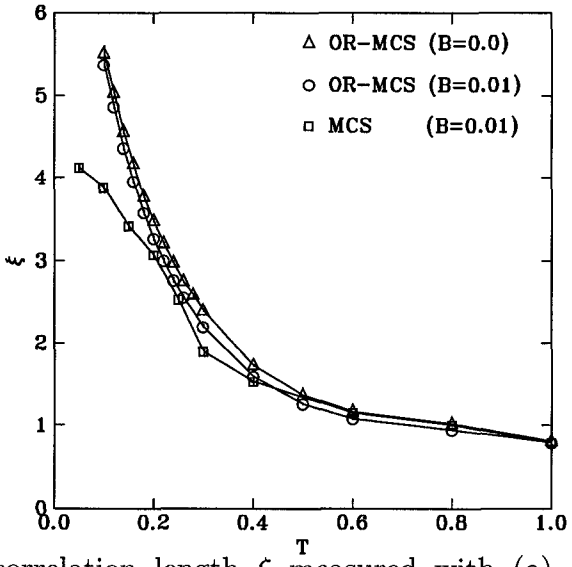

Figure 3.4: The correlation length ξ measured with ($\circ$) and without ($\Box$) over-relaxation at $x = 0.15$ and $L = 10$ and in a field $B = 0.01$. For comparison we show the results at $x = 0.15$ and $L = 10$ with $B = 0$ ($\triangle$). The MCS's and OR-MCS's is the same in both cases, namely 10^4. A lack of equilibration is clearly observed for the simulations which do not employ an over-relaxation update.

Table 3.2: Number of disorder configurations (C) used for each field (B) and system size (L) at $x = 0.15$ using the OR-MCS Monte Carlo updates.

L	B =0.01	0.03	0.10	0.30	0.60	1.00
4	500	500	500	500	500	500
6	500	500	500	500	500	500
8	500	500	500	500	500	500
10	500	400	500	480	64	500
12	280	128	242	160	94	60

function of the external magnetic field. Based upon our results for the zero field phase diagram, we have used 10^3 OR-MCS's to ensure equilibration. We then measure observables for using 10^3 OR-MCS's for $T > 2T_{xy}$ and 10^4 OR-MCS's for $T < 2T_{xy}$. We have checked in selected cases that the number of Monte Carlo updates is sufficient by repeating our measurements at the lowest temperatures where one expects τ to be largest. Furthermore, we checked that over-relaxation was indeed reducing τ by first performing simulations with solely Metropolis dynamics followed by measurements using over-relaxation and Metropolis dynamics. A typical measurement of the transverse spin glass correlation length measured with and without over-relaxation is shown in Fig. 3.4 in a field $B = 0.01$. As we shall show in Chapter 5, $B = 0.01$ is a small field and has a relatively small effect on ξ. For comparison, we also show in Fig. 3.4 the zero field ξ determined in our simulations using a much more rigorous equilibration test.

We have determined $T_{xy}(B)$ for six different fields ranging from $B = 0.01$ to $B = 1.0$, at $x = 0.15$. The number of configurations used to determine $T_{xy}(B)$ is shown in Table 3.2. Our goal is to have 500 configuration of disorder for each T, L, B, but at the time of writing, a small minority of the simulations have yet to finish.

3.3.2 Observables for the bond frustrated model

In prior Monte Carlo work on the bond frustrated model[80], the magnetization and transverse spin glass order parameters were calculated from time averages of the spin components; that is

$$\vec{m}_i = \frac{1}{M}\sum_{t=1}^{M} \vec{S}_i(t) \tag{3.18}$$

was used to measure the total magnetization

$$m_f = N^{-1}|\sum_{i=1}^{N} \vec{m}_i| \tag{3.19}$$

where M is the number of Monte Carlo updates. However, both Eqn. 3.18 and Eqn. 3.19 must be zero for an ergodic simulation of a rotationally invariant Hamiltonian. Despite this result, a finite magnetization was measured in these studies[80] demonstrating that their simulations were not ergodic. The reason a finite magnetization is measured can be easily understood by appealing to Fig. 3.2; when M exceeds τ by several orders of magnitude, $\vec{m}_i$ defined in Eqn. 3.18 will be consistent with zero. To demonstrate this one measures the autocorrelation function $A_{\vec{m}} =< \vec{m}(t_0)\cdot\vec{m}(t_0+t) >$ which as we have previously noted approaches $< \vec{m} >^2$ in the limit $t \rightarrow \infty$. Below T_C, τ becomes large for $\vec{m}$ because the direction taken by the magnetization wanders slowly; when M is much less than τ one observes a "freezing" and Eqn. 3.19 becomes non-zero. In the limit of very long simulations it is possible to see this very slow relaxation of the vector magnetization by measuring its autocorrelation function, as pointed out by Matsubara[81]. To measure ferromagnetic order we instead measure the scalar quantity given in Eqn. 3.14 which is insensitive to global rotations of the vector magnetization.

A similar problem exists in this early work for their definition of the transverse spin glass order parameter q_{xy}. The definition appearing in Ref. [80] is

$$q_{xy} = N^{-1}\sum_i [\vec{m}_i - (m_i \cdot \hat{z})\hat{z}]^2 \tag{3.20}$$

where the z axis is defined as the direction taken by the "spontaneous magnetization" calculated with Eqn. 3.19. Clearly, the same issues which plague the measurement of the magnetization will occur for this definition of the transverse spin glass order.

It is possible to measure spin glass order by measuring the autocorrelation function. For an Ising spin glass, one considers the autocorrelation function of the Edwards Anderson order parameter q, namely

$$q(t) = \sum_{t_0} \left(|\sum_i S_i(t_0) S_i(t_o + t)| \right) \tag{3.21}$$

One must take the absolute value prior to summing over all initial times t_0 since, as was shown by Ogielski[16], after long periods of time the spin system experiences global flips where all of all the spins invert, which without taking the absolute value would render Eqn. 3.21 zero. In the limit $t \to \infty$, Eqn. 3.21 approaches the EA order parameter q (Eqn. 1.5), and is strictly non-zero at finite temperatures for finite lattices. However, the simulation time required to measure the long time limit of $q(t)$ for spin glasses makes this method impractical.

Another way to measure spin glass order in an Ising spin glass is to simulate two identical replicas of the model, α and β, and to calculate the overlap

$$q = N^{-1} |\sum_i S_i^\alpha S_i^\beta|. \tag{3.22}$$

Since the two replicas are simulated independently, Eqn. 3.22 is just the $t = \infty$ limit of Eqn. 3.21, which eliminates the need to record spin configurations for each time step in a Monte Carlo simulation.

For a Heisenberg spin glass, things are more complex due to the vector nature of the spins. The spin glass order parameter is constructed[7] by calculating the overlap tensor at site i

$$q_{i,\mu\nu} = S_{i,\mu}^\alpha S_{i,\nu}^\beta \tag{3.23}$$

where $\mu, \nu = x, y, z$ are the three Cartesian components of the vector spin $\vec{S}$. To make a useful order parameter we sum over all of the spins for each of the nine $q_{i,\mu\nu}$

and calculate

$$q_{\mu\nu} = \sum_i q_{i,\mu\nu}. \tag{3.24}$$

The total overlap is then obtained in a similar fashion as for the magnetization;

$$q = (\sum_{\mu,\nu=x,y,z} q_{\mu\nu}^2)^{1/2} \tag{3.25}$$

which is the *scalar* spin glass order parameter for three component Heisenberg spins. At high temperatures where the spins are random and uncorrelated between the replicas each component of $q_{\mu\nu}$ will be zero, while in an ordered state where the spins in each replica are in the same state up to an overall rotation of the spins, q approaches a constant. Of course we must also average over time and disorder to obtain $[< q >]$.

While measures of spin glass order are useful, the best way to determine the phase boundaries are by measuring the appropriate correlation length[7, 8, 9, 10, 11, 15, 101]. The principal quantities we measure to do this are wave vector dependent susceptibilities $\chi(\mathbf{k})$ from which we determine the correlation length[7, 8, 15] using the definition

$$\xi = \frac{1}{2\sin(|\mathbf{k}_{min}|/2)} \left\{ \frac{[< \chi(0) >]}{[< \chi(\mathbf{k}_{min}) >]} - 1 \right\}^{\frac{1}{2}} \tag{3.26}$$

where $\mathbf{k}_{min} = (2\pi/L, 0, 0)$ is the minimum wave vector allowed by our choice of boundary conditions (periodic). In a ferromagnetic phase $\chi(\mathbf{k})$ is given by

$$\chi(\mathbf{k}) = \beta N^{-1} \sum_{i,\mathbf{r}} \mathbf{S}_i \cdot \mathbf{S}_{i+\mathbf{r}} e^{i\mathbf{k}\cdot\mathbf{r}} \tag{3.27}$$

where $\beta = 1/T$ is the inverse temperature and $\mathbf{r}$ is the vector connecting spins $\mathbf{S}_i$ and $\mathbf{S}_{i+\mathbf{r}}$.

In the spin glass phase we simulate two replicas with identical bonds and compute the spin glass overlap tensor at site i, Eqn. 3.23. The wave vector dependent spin glass susceptibility is then given in terms of the overlap as:

$$\chi(\mathbf{k}) = \beta N^{-1} \sum_{\mu,\nu} \sum_{i,\mathbf{r}} q_{\mu\nu,i} q_{\mu\nu,i+\mathbf{r}} e^{i\mathbf{k}\cdot\mathbf{r}}, \tag{3.28}$$

while the spin glass order parameter is given by Eqn. 3.25

Where ferromagnetism exists, we define a transverse spin glass overlap tensor $q^{\perp}_{\mu\nu,i}$ which is the overlap of spin components at site i perpendicular to the magnetization. In terms of $\mathbf{S}^{\perp}_i = \mathbf{S}_i - \mathbf{m} \cdot \mathbf{S}_i/m$, the transverse component of $\mathbf{S_i}$, we have $q^{\perp}_{\mu\nu,i} = S^{\mu,\perp}_{i,1} S^{\nu,\perp}_{i,2}$, where $\mathbf{m}$ is the vector magnetization and m its magnitude for each replica. The definition of $\chi_{\perp}(\mathbf{k})$ is then the same as for the spin glass (Eqn. 3.28) with the replacement of $q_{\mu\nu,i}$ by $q^{\perp}_{\mu\nu,i}$. The transverse spin glass order parameter is $q_{xy} = (\sum_{\mu\nu}(q^{\perp}_{\mu\nu})^2)^{1/2}$ with $q^{\perp}_{\mu\nu} = N^{-1}\sum_i q^{\perp}_{\mu\nu,i}$.

3.4 Finite size scaling

It is well known[79] that phase transitions only occur in the thermodynamic limit $L \rightarrow \infty$. Since Monte Carlo simulations are necessarily performed on finite sized systems, one must use finite size scaling in order to extrapolate the finite sized data to the infinite volume limit where a phase transition may occur.

The principles of finite size scaling are laid down in the framework of the renormalization group, and several books exist which explain the methodology[79, 96, 97]. Here we shall only concern ourselves with the results which we use in order to extract limiting ($L \rightarrow \infty$) results.

Near a second order phase transition in zero external field the magnetization, m, and the susceptibility, χ, (we defer the definitions for the next two sections) are expected to scale as

$$m(T, L) = L^{-\beta/\nu}\mathcal{M}(tL^{1/\nu}) \tag{3.29}$$

$$\chi(T, L) = L^{\gamma/\nu}\chi(tL^{1/\nu}). \tag{3.30}$$

where $t = \frac{T-T_C}{T_C}$ is the reduced temperature, β, γ, and ν are the standard static critical exponents, and L is the linear dimension of the finite lattice. The argument of both scaling functions $\mathcal{M}$ and χ, $tL^{1/\nu}$, is arrived at by noting that near a phase transition the only relevant variable is L/ξ, with ξ the correlation length. A simple

change of variables allows one then to write $L/\xi = Lt^{-\nu}$ or, as written in Eqns. 3.29 and 3.30, $L/\xi = tL^{-1/\nu}$. The variables $L^{-\beta/\nu}$ and $L^{\gamma/\nu}$ are just the dimensions of the magnetization and the susceptibility at the critical temperature, where $t = 0$. Dimensionless quantities such as the Binder cumulant scale according to

$$B = \mathcal{B}(tL^{1/\nu}). \tag{3.31}$$

The useful quantity ξ/L, the correlation length divided by the system size, is expected to scale in the same way as the Binder cumulant, that is

$$\xi/L = \mathcal{F}(tL^{1/\nu}). \tag{3.32}$$

The main use of the Binder cumulant and ξ/L are that at T_C of a second order phase transition, both ξ/L and B are L independent which allows one to identify the transition by the crossing point for different sized lattices.

On a scaling plot, where for example one plots $mL^{\beta/\nu}$ vs. $tL^{1/\nu}$, extrema such as the peak in the susceptibility or the maximum slope of the Binder cumulant must fall onto the same place for one to observe a collapse of the data. If we identify the location of an extremum as a size dependent pseudo-transition temperature $T_C(L)$, one must have

$$T_C(L) = T_C + aL^{-1/\nu}. \tag{3.33}$$

which allows one to determine T_C at $L \to \infty$ by extrapolating the finite sizes $T_C(L)$. Of course, one must know what the exponent ν is in order for this extrapolation to work.

Chapter 4

Results and Discussion for the ±J site frustrated model

In this chapter we present the phase diagrams for the three dimensional $\pm J$ site frustrated Heisenberg model with nearest neighbor interactions, defined by Eqn. 1.6 and Eqn. 1.7 in the introduction. We have studied the model with $J_{FF} = -J_{AA} = -J_{FA} = +1$, which is frustrated as well as a variant model with $J_{FF} = -J_{AA} = +1$ and $J_{FA} = 0$ which has no frustration. We first show the phase diagrams in order to motivate the discussion prior to discussing some simple yet important gauge symmetries. We then show how we obtain the phase diagrams from our Monte Carlo data, with an emphasis on how we can rule out the phase diagram given by Bekhechi and Southern[60] which is illustrated in Fig. 1.7(d). We then discuss why the phase diagrams for site frustrated models order in the manner they do, which is related to the location of the frustration in the model. Finally, we give some concluding remarks in order to give insight into our experiments on both bond frustrated and site frustrated magnets.

4.1 Results

4.1.1 The phase diagrams

The phase diagrams for the site frustrated Heisenberg model are shown in Fig. 4.1 for the simple cubic lattice (a), body centered cubic lattice (b) and face-centered cubic lattice (c). Our phase diagram for the simple cubic lattice (sc) are somewhat different than those given in all previous Monte Carlo studies[58, 59, 60]. We find that, for the sc and bcc lattices, ferromagnetic order (FM) exists provided only that ferromagnetic (F) sites percolate while antiferromagnetic (AF) order exists provided only that antiferromagnetic (A) sites percolate. For sc and bcc lattices, where the site percolation thresholds are less than $\frac{1}{2}$, there are thus *two* identifiable percolating clusters, composed of A and F sites respectively, and in the regime where both exist they both order. For the fcc lattice, there are also two identifiable percolating clusters, but as discussed previously we have not attempted to measure the AF order and so the phase diagram for the fcc lattice lacks mixed phase.

To better understand this behavior, we show in Fig. 4.2 the phase diagrams that result when the coupling between F and A sites is made to be zero. In this case the model possesses no frustration, and can readily be understood from the theory of dilute magnetism[94]. In a nearest neighbor site dilute magnet, a random fraction of sites is removed from the lattice along with its nearest neighbor bonds. As sites are removed, the transition temperature drops continuously and meets the $T = 0$ axes at the site percolation threshold x_p ($x_p = 0.311$ for the sc lattice, $x_p = 0.245$ for the bcc lattice, and $x_p = 0.19$ for the fcc lattice[106]). Clearly, were one to consider the vacancies as a sites themselves, vacancies will percolate at $1-x_p$. Considering the sites in the dilute model to be of type F and the vacancies to be type A, while ensuring that the F and A sites do not interact by making $J_{FA} = 0$, results in the phase diagrams shown in Fig. 4.2(a) and (b), provided that $J_{FF} = +1$ and $J_{AA} = -1$. The remarkable similarity between the phase diagram of the site frustrated Heisenberg

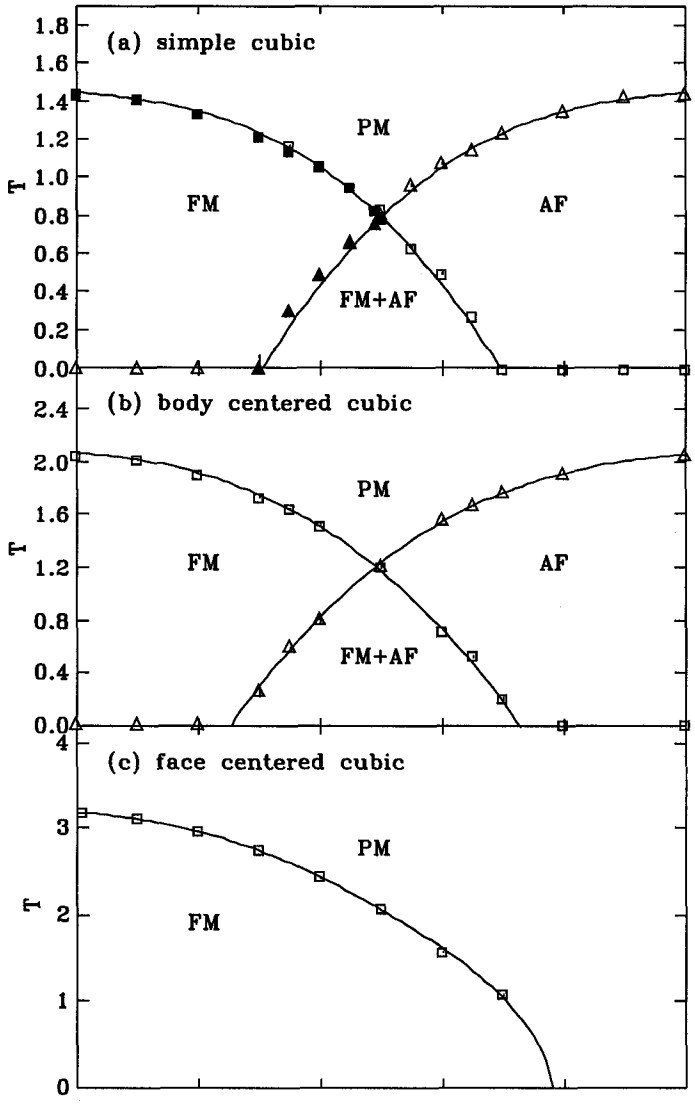

Figure 4.1: Phase diagrams of the site frustrated Heisenberg model for (a) simple cubic (b) body-centered cubic and (c) face-centered cubic lattices. Transitions marked by solid symbols in (a) are obtained with 200+ configurations of disorder, and system sizes L=4, 6, 8, 10, 12, 16, 20 and 24. Transition temperatures and errors are given in Table 4.1. Transitions marked by open symbols are obtained from 16+ configurations only, and smaller system sizes. Lines marking phase boundaries are guides to the eye.

model and this non-frustrated model serve to emphasize that the important physics at work is site percolation.

The only effect of the coupling between A and F sites, which produces the frustration, is to give rise to a planar type anisotropy which causes the lower temperature ordered phase to exist transverse to the upper temperature ordered phase: The two types of order are perpendicular. Furthermore, there is no change in the universality class of the transitions from that of the pure models at $x = 0$ and $x = 1$ which are in the Heisenberg universality class. Both Bekhechi and Southern[60] and Matsubara *et al.*[59] have reported that the model no longer remains in the Heisenberg universality class for both the upper and lower temperature transition within the mixed phase. We, however, find that all the transitions are consistent with belonging to the Heisenberg universality class. This difference is likely caused by a misidentification of the transition temperatures. Where we agree with Bekhechi and Southern that the model remains in the Heisenberg universality class we also agree on the transition temperatures. Where there is disagreement on the nature of the universality class, we do not agree with the transition temperatures of Bekhechi and Southern.

It may be expected that the planar anisotropy will change the universality class. Indeed, our finding[21], and those of others[58, 59], that the direction of the ferromagnetic order $\vec{m}_f$ and the direction of the antiferromagnetic order $\vec{m}_{st}$ are perpendicular below the lower temperature transition shows that we have $\vec{m}_f \cdot \vec{m}_{st} = 0$. The energy/spin associated with the planar anisotropy (ϵ_{anis}) likely has a form akin to $\epsilon_{anis} = (\vec{m}_f \cdot \vec{m}_{st})^2$. However, at the critical temperature of the lower temperature transition (T_N for $x < 0.5$ and T_C for $x > 0.5$) we have either $m_{st} = 0$ or $m_f = 0$ and so the anisotropy doesn't develop at the critical temperature, but below it. We expect that this is the reason the universality class does not change.

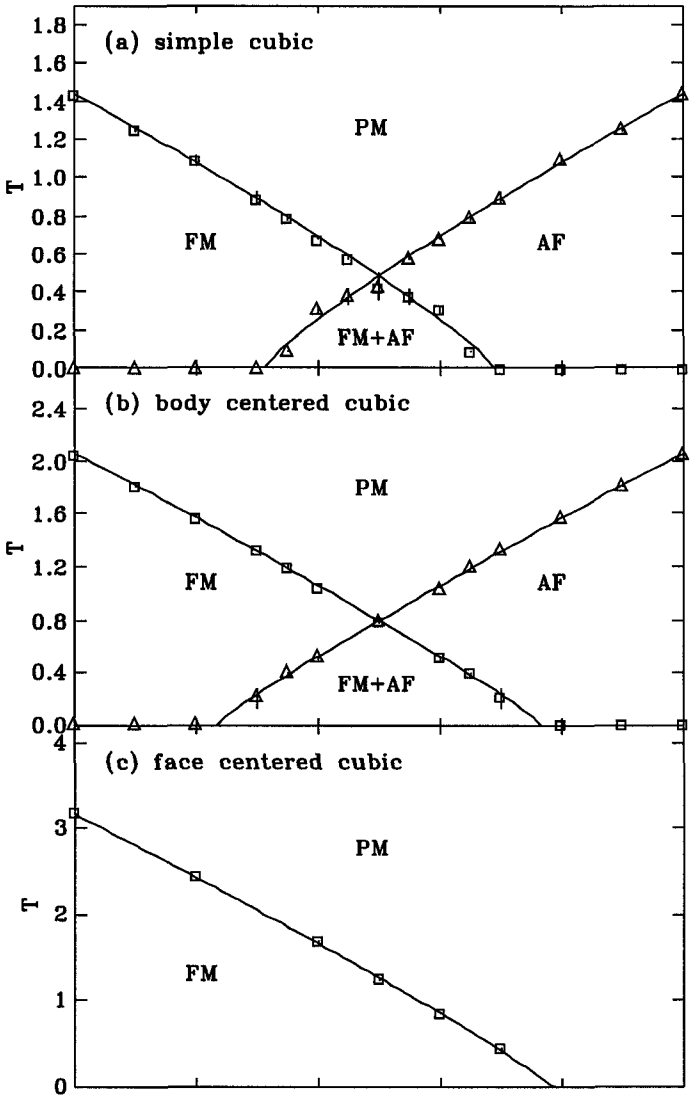

Figure 4.2: Phase diagrams of the non frustrated model with J_{FA}=0 for (a) simple cubic (b) body-centered cubic and (c) face-centered cubic lattices. The phase diagrams are, aside from a rescaling of the transition temperatures, identical to those of the site frustrated Heisenberg model shown in Fig. 4.1. Lines marking phase boundaries are guides to the eye.

4.1.2 Gauge symmetries

In the presence of a random distribution of bimodal interactions, ($J_{ij} = \pm 1$), a Hamiltonian of the type shown in Eqn. 1.6 will possess a number of useful symmetries. Frustration is the property that, given a set of spins $\{\vec{S}_i\}$ linked with a closed loop of non-zero J_{ij}, no set $\{\vec{S}_i\}$ exists which can satisfy all of the interactions J_{ij}. Frustration is measured by considering the value of the frustration function[107, 108]

$$\phi = \prod J_{ij} \tag{4.1}$$

evaluated around a plaquette – the smallest closed loop of S_i linked by non-zero J_{ij}. If $\phi < 0$ then a plaquette is frustrated while if $\phi > 0$ the plaquette is not frustrated. Since Eqn. 4.1 always contains even powers of J_{FA} for a site frustrated model, frustration is independent of the sign of J_{FA}. It follows that frustration is only present if $J_{FF} = -J_{AA}$.

Model symmetries can be found by considering a local transformation of the spin and bond variables according to[108]

$$\vec{S}_i \rightarrow -\vec{S}_i, \qquad J_{ij} \rightarrow -J_{ij} \tag{4.2}$$

where a spin at site i is inverted as well as all of the bonds J_{ij} emanating from site i. Any set of such local transformations

$$G(\{\tau_i\})[\{\vec{S}_i\};\{J_{ij}\}] = [\{\tau_i\vec{S}_i\};\{\tau_i J_{ij}\tau_j\}] \tag{4.3}$$

with τ_i=$\pm$1, called a gauge transformation, preserves both the Hamiltonian and the distribution of frustration[108]. Since the Hamiltonian is invariant under any $G(\{\tau_i\})$, the partition function and the free energy are also invariant. It follows that any pair of models with different distributions of the variables J_{ij}, yet having the same distribution of frustration, have the same phase diagram (the order parameters are, in general, different).

A first symmetry is revealed using the gauge transformation

$$G(\tau_A = \pm 1; \tau_F = \mp 1) \tag{4.4}$$

which inverts the spins of either all A or all F sites in the lattice. The bonds are transformed such that $J_{FA} \rightarrow -J_{FA}$ while both J_{FF} and J_{AA} remain invariant. Therefore, phase diagrams of site frustrated models (provided $|J_{FF}|=|J_{AA}|$) are invariant with respect to the sign of J_{FA}.

A second symmetry occurs for bipartite lattices which can be decomposed into two interpenetrating sublattices α and β, and where the nearest neighbours of sites in the α sublattice all belong to the β sublattice and vise versa. The gauge transformation

$$G(\tau_\alpha = \pm 1; \tau_\beta = \mp 1) \tag{4.5}$$

has the effect of flipping the sign of all of the bonds so that $J_{ij} \rightarrow -J_{ij}$. This is equivalent to taking a model with a concentration x of A sites ($1-x$ of F sites) and creating a model with a concentration $1-x$ of A sites (x of F sites), while also flipping J_{FA} which, as we have already shown, is irrelevant. Therefore, for bipartite lattices, the phase diagrams must be symmetrical about $x=\frac{1}{2}$.

The symmetry between ferromagnetic and antiferromagnetic models on bipartite lattices found by using the gauge transformation given by Eqn. 4.5 only applies to lattices with L even. If L is odd, as in the simulations of Matsubara *et al.*[59], then two equivalent sublattices do not exist. Indeed, in this case the staggered magnetization will possess a twist, similar to the twist observed in pure Heisenberg models with opposing surface fields[109]. For this reason, we believe the results of Matsurbara *et al.*[59] should be treated with caution.

One effect of Eqn. 4.5 is to transform the FM order parameter m_f into the AF order parameter m_{st}, and vice versa. Thus, if the model orders as a collinear FM, a collinear AF, or a mixture of the two (whose order need not be parallel) then gauge symmetry implies the following symmetry between the order parameters m_f and m_{st}:

$$m_f(x, T; J_{FA}) = m_{st}(1-x, T; -J_{FA}) \tag{4.6}$$

$$m_{st}(x, T; J_{FA}) = m_f(1-x, T; -J_{FA}) \tag{4.7}$$

for all x and T. This symmetry also applies to all higher order powers of m_f and m_{st},

and therefore the susceptibilities are also symmetric under the exchange $x \rightarrow (1-x)$, $J_{FA} \rightarrow -J_{FA}$. This symmetry persists even when the ordering does *not* consist of a mixture of collinear FM and AF order, as for example spin glass order. However, in the case of spin glass order, m_f and m_{st} would scale to zero in the limit of large L. The fact that we observe a non-zero m_f and/or m_{st} for all concentrations in the limit of large L for bipartite lattices excludes any possibility that the mixed phase is a pure spin glass phase which lacks long range periodic order.

4.1.3 Determination of the phase diagrams

To determine the form of the phase diagram, we have extracted the system-size dependent pseudo-transition temperatures $T_{C,N}(L)$ from the peak in $\chi^c_{f,st}$ and the maximum slope in $B_{f,st}$. According to finite size scaling theory, we expect that $T_{C,N}(L)$ should, for large enough L, scale according to

$$T_{C,N}(L) = T_{C,N} + aL^{-1/\nu}, \tag{4.8}$$

where ν is the exponent of the correlation length. Eqn. 4.8 allows us to locate T_C and T_N. We begin by assuming that the model remains in the Heisenberg universality class, for which the exponent ν takes the value[82, 83] ν=0.704. Scaling plots for several concentrations are shown for the sc lattice in Fig. 4.3 for both T_C and T_N. With increasing L the data begin to fall onto straight lines (see also Fig. 4.8 inset (b)), indicating that corrections to scaling are important for the smaller lattices. For $L > 8$ ($\chi^c_{f,st}$) and $L > 10$ ($B_{f,st}$) the $T_{C,N}(L)$ are linear in $L^{-1/\nu}$ and yield the same estimates for T_C and T_N within error. In the case of the pure model ($x = 0$), the asymptotic scaling regime beyond which corrections to scaling become negligible is also[82] $L \sim 10$, and so the deviations at small L are to be expected. Straight line fits for $L > 10$ yield two independent estimates for both T_C and T_N, and the weighted average of the two estimates are summarized in Table 4.1 for $x \leq 0.5$. While the estimates for T_C and T_N so obtained are our most precise results, they do depend

Table 4.1: Critical temperatures for the site frustrated Heisenberg model for the sc lattice type. Note that by symmetry $T_C(x)$=$T_N(x)$.

x	$T_C(x)$	$T_N(x)$
0.10	1.4155(6)	———
0.20	1.3389(9)	———
0.30	1.2189(7)	———
0.35	1.1420(17)	0.2980(22)
0.40	1.0546(8)	0.4862(23)
0.45	0.9491(6)	0.6576(25)
0.49	0.8259(18)	0.7536(32)
0.50	0.7804(13)	0.7794(4)

upon the assumption of universality. However, estimates found assuming universality are consistent with other estimates – in particular those found from crossings of the Binder cumulant, which make *no* reference to a particular universality class.

The analysis which led to the phase diagram shown in Fig. 4.1(a) assumed that the site frustrated Heisenberg model remains in the three dimensional Heisenberg universality class. That the transition temperatures found assuming this universality are correct is demonstrated in Fig. 4.4 where we have plotted the crossing of the Binder cumulant B_f for x=0.45. According to finite size scaling theory, $B_{f,st}$ should scale as

$$B_{f,st} = B_{f,st}(tL^{1/\nu}) \tag{4.9}$$

where t=$(T - T_{C,N})/T_{C,N}$ is the reduced temperature. Thus, a plot of $B_{f,st}$ for different L should exhibit a crossing at $T_{C,N}$. Note that the location of this crossing is independent of the universality class of the transition. The crossing near T_C=0.947(5) is clear, and agrees well with our estimate T_C=0.9491(6) found from Fig. 4.3 where we assumed that the model was in the Heisenberg universality class in order to extract

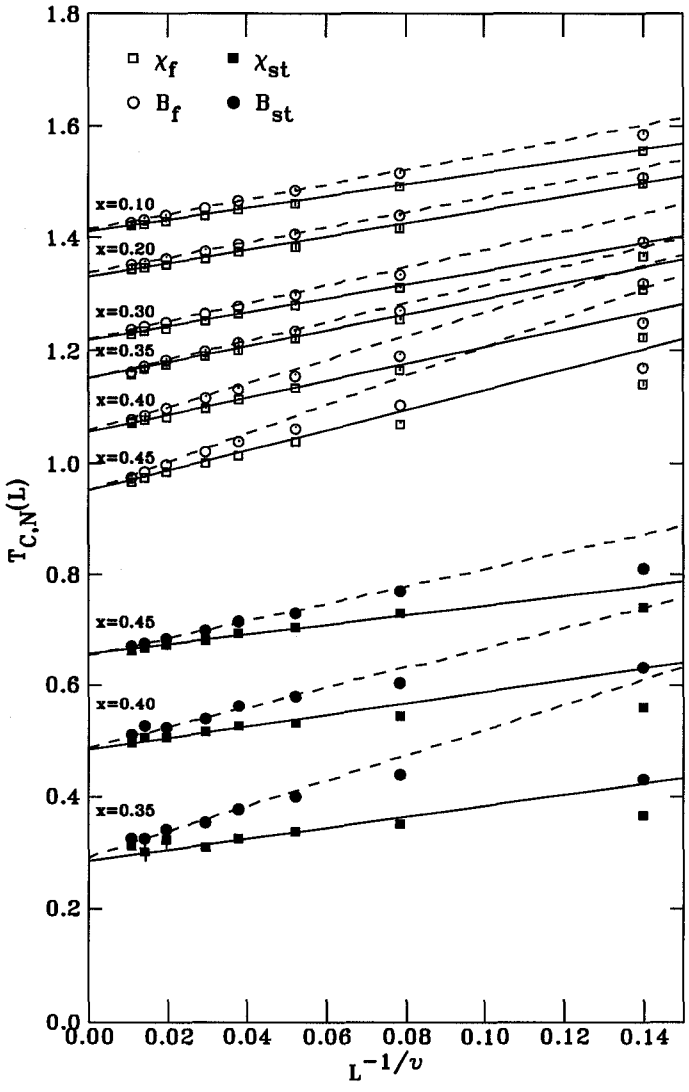

Figure 4.3: Finite size scaling of the pseudo-transition temperatures $T_C(L)$ and $T_N(L)$ for the site frustrated Heisenberg model on sc lattices. Lattice sizes L=4, 6, 8, 10, 12, 16, 20 and 24. The exponent ν=0.704 is taken for the Heisenberg universality class. Solid lines are fits, for $L > 8$, to $T_{C,N}(L)$ (Eqn. 4.8), obtained from the peak in χ^c. Dashed lines are fits, for $L > 10$, to $T_{C,N}(L)$ obtained from the maximum slope in $B_{f,st}$. Where error bars are not not apparent, they are smaller than the symbol size.

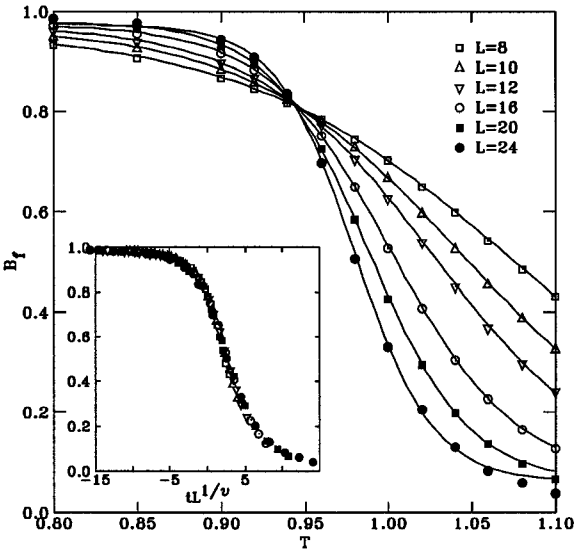

Figure 4.4: Binder cumulant B_f of the ferromagnetic order near T_C for frustrated sc lattice at x=0.45. Lines are guides to the eye. Inset shows collapse of the data according to Eqn. 4.9 using the exponent ν=0.704. Where error bars are not apparent, they are smaller than the symbol size.

T_C. Our value is both far from the earlier estimate[60] T_C= 0.925(5), and more precise. At x=0.45 they estimated[60] that $\nu\sim1$. However, as shown in the inset of Fig. 4.4, the Binder parameter scales very well using Eqn. 4.9 with ν=0.704 provided $L>8$.

More evidence to support our conjecture that the model remains within the Heisenberg universality class is found in the scaling of the order parameters and their fluctuations. Finite size scaling theory predicts that in the vicinity of $T_{C,N}$, $m_{f,st}$ and $\chi_{f,st}$ scale according to

$$m_{f,st} = L^{-\beta/\nu} M(tL^{1/\nu}) \tag{4.10}$$

$$\chi_{f,st} = L^{\gamma/\nu} X(tL^{1/\nu}) \tag{4.11}$$

for large enough L. In Fig. 4.5 we show scaling plots for $m_{f,st}$ and $\chi^d_{f,st}$ at x= 0.45, where it has been estimated[60] that $\beta/\nu\sim0.35$ and, from hyperscaling, γ/ν=2.3. In the four plots we have used the exponent ratios β/ν=0.514 and γ/ν=1.973, with ν=0.704, as found for the pure Heisenberg model[82, 83] (x=0) in three dimensions.

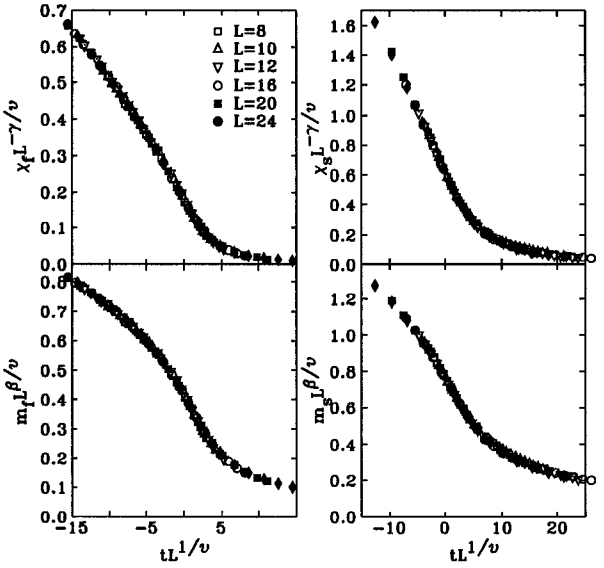

Figure 4.5: Finite size scaling collapse of m_f and χ_f^d with T_C=0.9491 and m_{st} and χ_{st}^d with T_N=0.6576 for L=8, 10, 12, 16, 20 and 24. We have used the ratios β/ν=0.514 and γ/ν=1.973 of the three dimensional Heisenberg universality class.

The values of $T_{C,N}$ are taken from our Table 4.1. The collapse is excellent for $8 \leq L \leq 24$ which strongly suggests that the transitions remain within the Heisenberg universality class.

Undoing the collapse of the x-axis shown in Fig. 4.5 provides further support that the site frustrated model remains in the Heisenberg universality class. If we plot $m_{f,st} L^{\beta/\nu}$ or $\chi_{f,st}^d L^{-\gamma/\nu}$ vs. T for different L, then Eqns. 4.10 and 4.11 predict that we should observe a crossing of the data at $T_{C,N}$ similar to that observed for $B_{f,st}$, as shown in Fig. 4.4. In Fig. 4.6 we show such plots for the ferromagnetic transition at x=0.45 – the same data used in the left panels of Fig. 4.5. A clear crossing is observed just below T=0.95.

We now turn to the form of the phase diagram near x=0.5. Aharony[70] first postulated the existence of a tetracritical point where the lines of second order phase transitions, $T_C(x)$ and $T_N(x)$, cross. The phase diagram of Nielsen *et al.*[110] also exhibits a tetracritical point, as does the phase diagram of Matsubara *et al.*[59], although in the latter case it was assumed. In contrast, it has been suggested[60]

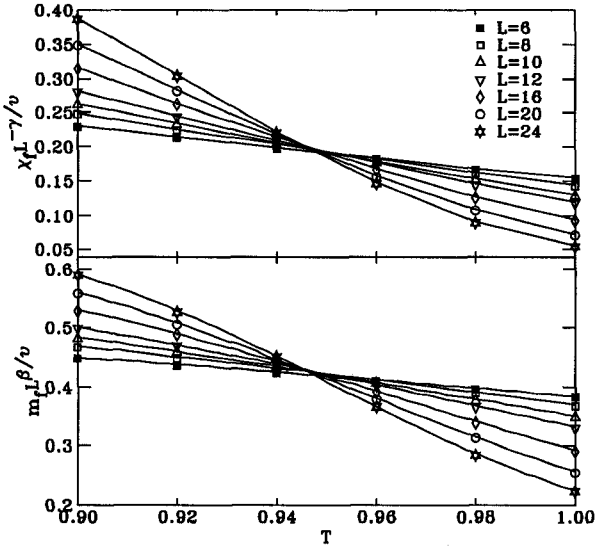

Figure 4.6: Scaling plot of $m_f L^{\beta/\nu}$ and $\chi_f^d L^{-\gamma/\nu}$ vs. temperature at x=0.45. Exponents are the same as in Fig. 4.5. A clear crossing is observed near T_C=0.9491. A further scaling the x-axis according to $tL^{1/\nu}$ results in the collapse shown in Fig. 4.5. Where error bars are not not apparent, they are smaler than the symbol size.

that the tetracritical point does not exist and instead there exists a regime from $0.48<x<0.52$ where $T_C(x)=T_N(x)$. We have reported[68] that the scaling of $T_{C,N}(L)$ according to Eqn. 4.8 at x=0.49, 0.495 and 0.5 (for $L\leq 20$ and C=100) disagrees with this conjecture. Results from this study[68] are shown in Fig. 4.7 in units of $T_C(x=0)$. Our updated results at x=0.49 and x=0.5 (with $L\leq 24$ and $C>200$), as listed in Table. 4.1, confirms that $T_C(x)\neq T_N(x)$ with the exception of x=0.5.

Further evidence in favor of a tetracritical point is provided by examining the behavior of the transition temperatures while varying the magnitude of the inter-site coupling $|J_{FA}|$. Setting $J_{FA}=0$ decouples F and A sites, giving the non-frustrated model and hence $T_C = T_N$ at $x = 0.5$ *only*. Elsewhere $T_C \neq T_N$ and the phase diagram possesses a decoupled tetracritical point at $x = 0.5$. If the ordering scenario in Ref. 12 were correct and $T_C = T_N$ at $x = 0.49$ when $J_{FA} = 1$, then T_C and T_N would evolve with increasing J_{FA} such that the two transition temperatures merged. Conversely, if the transition temperatures remain distinct, as one expects if the site

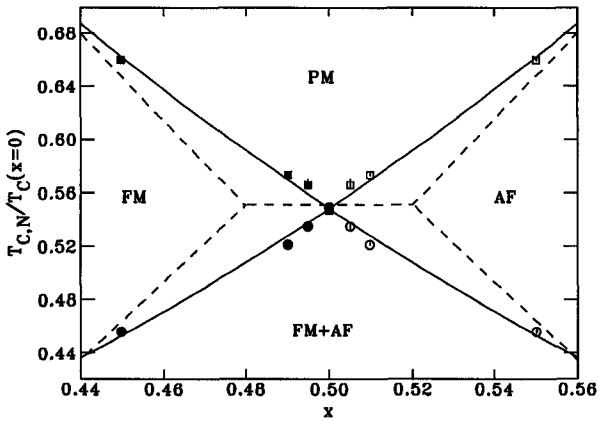

Figure 4.7: A close up view of the tetracritical point. We show T_C and T_N calculated using $L \leq 20$ averaged over 100 configurations of disorder. The data points for $x > 0.5$ are obtained by symmetry. Solid line is a schematic of the tetracritical point while dashed lines are a schematic of Bekhechi and Southerns conclusion that $T_C(x) = T_N(x)$ for $0.48 < x < 0.52$.

frustrated model possess a tetracritical point, then T_C and T_N must remain distinct as J_{FA} increases.

In Fig. 4.8 we show the evolution of both T_C and T_N at $x = 0.49$ for the sc lattice with $J_{FA} = 0, -1 - 2$ and -3. It is clear from the plot that both T_C and T_N increase with increasing J_{FA} in this regime, and that T_C is never equal to T_N. In the inset (a) of Fig. 4.8 we show the difference, $T_C - T_N$, which clearly indicates that the transition temperatures do not merge. Instead, the difference steadily *increases* (the difference between T_C and T_N is greater than 10σ). We have observed[69] the same behavior for the bcc lattice at $x = 0.4$ up to $J_{FA} = 30$. As shown in the inset (b) of Fig. 4.8, the scaling of the pseudo-transition temperatures (as in Fig. 4.3) at $x = 0.49$ with $J_{FA} = -1$ is typical of all our measurements and does not indicate anything which might suggest that $T_C = T_N$. Rather, the fits to the pseudo-transition temperatures for χ_f^c and χ_{st}^c are within error parallel, as are the fits to B_f and B_{st}. We conclude that the site frustrated model possess a tetracritical point at $x = 0.5$ and that $T_C \neq T_N$

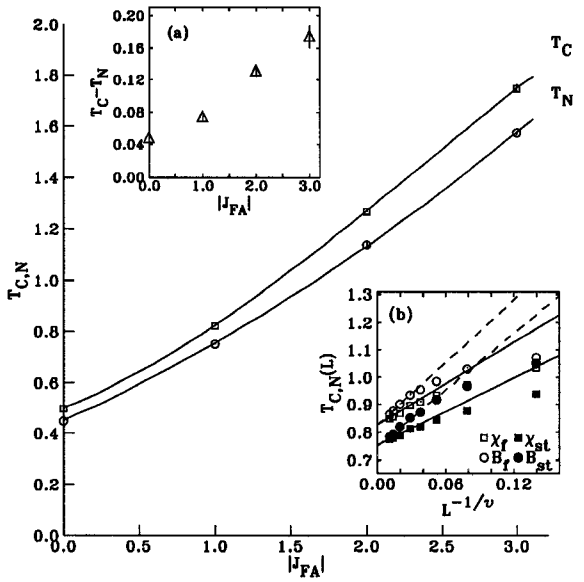

Figure 4.8: T_C and T_N vs. $|J_{FA}|$ with $J_{FF} = -J_{AA} = +1$ for the sc lattice at $x = 0.49$. Inset (a) shows the difference, $T_C - T_N$. Inset (b) shows the scaling of the pseudo-transition temperatures for $J_{FA} = -1$. Where error bars are not not apparent, they are smaler than the symbol size.

for all other x.

4.2 Discussion

4.2.1 Frustration distribution and density

To understand the phase diagrams of the site frustrated Heisenberg model it is necessary to consider both the density and the distribution of frustration within the model. The density of frustration can easily be calculated from the probability that a plaquette exists in a frustrated configuration. In Fig. 4.9 we show examples of frustrated plaquettes for a four spin plaquette, appropriate for sc and bcc lattices, and for a three spin plaquette, appropriate for fcc lattices. In the case of sc and bcc lattices, site frustrated models produce frustrated plaquettes *only* when the plaquette contains two neighboring F sites and two neighboring A sites. For fcc lattices a plaquette is frustrated when it contains either two or three A sites. The density of frustrated

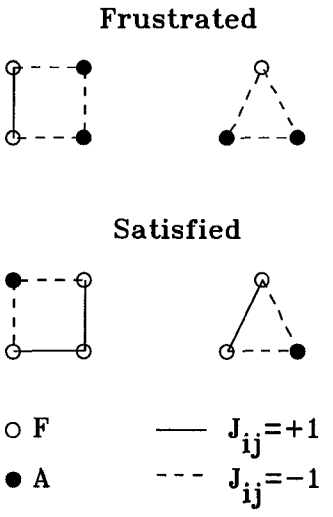

Figure 4.9: Examples of frustrated and satisfied plaquettes for the site frustrated model for a four spin plaquette geometry appropriate for sc and bcc lattices and for a three spin plaquette geometry appropriate for fcc lattices.

plaquettes, x_f, is

$$x_f = 4x^2(1-x)^2 \tag{4.12}$$

for sc and bcc lattices and

$$x_f = 3x^2(1-x) + x^3 \tag{4.13}$$

for fcc lattices. In the same way, the density of frustrated plaquette in the *bond* frustrated model is:

$$x_f = 4x(1-x)^3 + 4x^3(1-x) \tag{4.14}$$

for sc and bcc lattices, and

$$x_f = 3x(1-x)^2 + x^3 \tag{4.15}$$

for fcc lattices, where for bond frustrated models x is the concentration of antiferromagnetic bonds, while for site frustrated models x is the concentration of antiferromagnetic sites. The densities of frustrated plaquettes given by Eqn. 4.12-4.15 are plotted in Fig. 4.10.

If site and bond frustrated models were gauge equivalent, as has been previously assumed[71], then x_f would be the same for both the site frustrated model and its

gauge equivalent bond frustrated counterpart, since x_f is gauge invariant. The site frustrated model on sc and bcc lattices has a maximum of $x_f = 0.25$ and thus the assumed gauge equivalent bond frustrated model must have $x<0.08$ (or $x>0.92$), so that $x_f \leq 0.25$ (see Fig. 4.10). At this concentration of antiferromagnetic (ferromagnetic) bonds, 3d bond frustrated models are certainly ordered ferromagnets[11, 101, 111, 112] (antiferromagnets). Assuming gauge equivalence between site and bond frustrated models in three dimensions implies that the site frustrated model has a FM transition or a AF transition for all x, although the order may be hidden in the same sense that the FM order is hidden in the Mattis model. Therefore, the assumption of gauge equivalence rules out pure spin glass order as the model would possess a transition in the ferromagnetic Heisenberg universality class. The phase diagram that results from the assumption of gauge equivalence between site frustrated and bond frustrated models is illustrated in Fig. 1.7(c).

It is easy, however, to prove that site and bond frustration are *n*ot gauge equivalent on bipartite lattices. To do so consider the probability that, given a frustrated plaquette, all of the neighboring plaquettes exist in a frustrated configuration. For a bond frustrated model this probability is finite for $0<x<1$ while for site frustrated models this probability is zero for $0 \leq x \leq 1$ which is sufficient to prove that site and bond frustrated models are not gauge equivalent.

It is also interesting to note that the site frustrated model on an fcc lattice exists as an ordered ferromagnet until $x_f \sim 0.9$ ($x \sim 0.8$) while for the sc *bond* frustrated model ferromagnetism is lost by $x_f \sim 0.44$ ($x=0.208(2)$) for Heisenberg[101] spins. This serves to emphasize that the density of frustration alone is not responsible for the destruction of periodic order, but it is the distribution of the frustration which, as we have shown, is quite different for site and bond frustrated models.

For sc and bcc lattices, frustrated plaquettes exist only when a plaquette contains two neighboring F sites and two neighboring A sites. If the lattice is considered to be a collection of F and A clusters, it follows that all of the frustrated plaquettes exist on

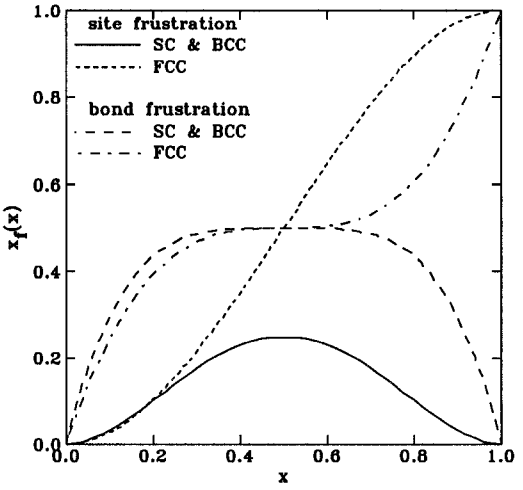

Figure 4.10: The density of frustration for site and bond frustrated models on sc, bcc and fcc lattices. Note that the density of frustration is much less for the site frustrated model on sc and bcc lattices as compared to the bond frustrated model.

the surfaces separating the clusters. Since all of the frustration exists at the interface which separates clusters of F and A sites, unsatisfied bonds are likely to also reside near that interface. Given this situation, the phase diagrams of site frustrated models (Fig. 4.1) can be expected to mimic those of the non-frustrated models (Fig. 4.2), as we have observed.

The effect of concentrating all of the frustrated plaquettes onto the surfaces separating clusters of F/A sites will be explored by considering simple Ising spins since algorithms exist for determining exact ground states. In two dimensions (2d), ground states for Ising spins with $\pm J$ interactions are determined by pairing frustrated plaquettes with a line called a dual string. Bonds traversed by the dual string are broken with the remaining bonds satisfied. It then follows that the ground state is determined by minimizing the total length of all dual strings[108].

We first consider a diagonal, (1 1), surface separating clusters of F and A sites. This configuration of bonds, shown in Fig. 4.11(a), has no frustration, and the ordering which takes place belongs to the pure, ferromagnetic, 2d Ising universality

class.

A (1 0) interface, shown in Fig. 4.11(b), while superficially similar to (1 1) interface, actually creates a configuration with an infinite number of frustrated plaquettes. The lowest energy state then consists of all F sites ordered ferromagnetically and all A sites ordered antiferromagnetically. Satisfied and unsatisfied bonds alternate along the interface leading to a two-fold degeneracy, decoupling the two regions. The orientation of the FM order is free to point up or down with respect to a fixed AF order, this effectively mimics the model where $J_{FA} = 0$.

The third configuration we consider is two frustrated plaquettes separated by a finite distance shown in Fig. 4.11(c). The lowest energy state consists of F sites ordered FM and A sites ordered AF with a line of unsatisfied bonds along the shortest path connecting the two frustrated plaquettes. In this case, a preferred relative orientation (unidirectional anisotropy) is imposed upon, for instance, the FM order if the AF ordering has already taken place.

The last configuration we consider consists of an interface with randomly placed frustrated plaquettes, shown in Fig. 4.11(d). The two shortest ways of connecting these plaquettes with dual strings (A–B, C–D, E–F, *etc.* and B–C, D–E, F–G *etc.*) need not have the same energy, leading to unidirectional anisotropy. However, for a very long interface, the difference in energy associated with these two possible linkings becomes infinitesimally small, and the FM ordered F sites and AF ordered A sites are again decoupled, mimicking the model with $J_{FA} = 0$.

The examples considered here demonstrate that frustration at the interface of F/A clusters tends to either decouple the FM and AF ordering, Fig. 4.11(b,d), or to introduce unidirectional anisotropies, Fig. 4.11(c,d). This behavior will only occur if the dual strings which link frustrated plaquettes reside near the interface, and do not pass through the volume of the cluster. However, if we constrain our interest to percolating F/A clusters, the density of frustration at the interface is large ($\sim 25\%$) so that the total length of the associated dual strings linking the frustrated plaquettes

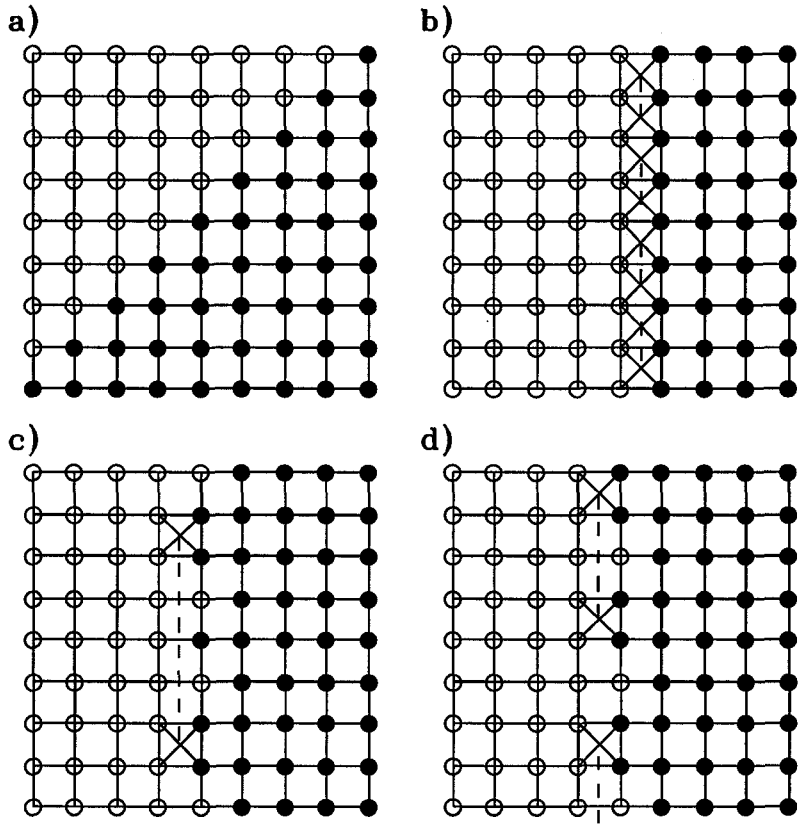

Figure 4.11: Two dimensional square lattices showing various possible interfaces between F and A sites where frustration occurs. (a) Flat (1 1) interface, no frustration. (b) Flat (1 0) interface, infinite number of frustrated plaquettes (crosses) on interface. (c) Two frustrated plaquettes separated by a finite distance, energy is proportional to the length of the dual string (broken line) linking them. (d) Rough (1 0) interface, random linear distribution of frustration. Only one of the two shortest linkings is shown.

will be minimized by using short elements traversing the interface. Equivalently, bonds which compose the volume of a percolating cluster, $\propto L^d$, are satisfied at the expense of the bonds at the interface of the percolating cluster, $\propto L^{d-1}$ leading to the conclusion that percolating clusters of F or A sites order FM or AF, identical to the respective pure models. Decoupling of the FM and AF ordered clusters will then occur when the number of satisfied and unsatisfied bonds at the interface are equal so that the ordered clusters are free to take any possible orientation.

Given the configuration of bonds in Fig. 4.11(b) where for Ising spins there is a decoupling of the AF and FM order, it can be imagined that for Heisenberg spins the energy of the system can be further reduced: If the AF and FM ordering directions are chosen to be mutually perpendicular, there is a net reduction in the interface energy if the AF ordered spins near the interface cant either up ($J_{FA} = +1$) or down ($J_{FA} = -1$) with respect to the FM order, minimizing exchange energy from the J_{FA} bonds at the expense of the J_{AA} bonds. This net energy change would then give rise to mutually perpendicular FM and AF order[59]. The perpendicular nature of the FM and AF order is shown in Fig. 4.12, where we depict the parallel and perpendicular components of m_{st} with respect to m_f for both the frustrated and non-frustrated models. The situation is analogous to isotropic antiferromagnets in a uniform external field[113] where the AF ordering is transverse to the applied field, with the moments canting upwards along the applied field in order to minimize the total energy.

4.2.2 The site frustrated model on fcc lattices: A spin glass?

Within our picture, site frustrated Heisenberg models on bipartite lattices cannot account for the spin glass ordering occurring in site frustrated materials since in the model, a pure spin glass phase without long range periodic order is not realized at any composition. This lack of a spin glass phase is due in part to insufficient frustration in the model on bipartite lattices. Increasing the concentration of frustration, and

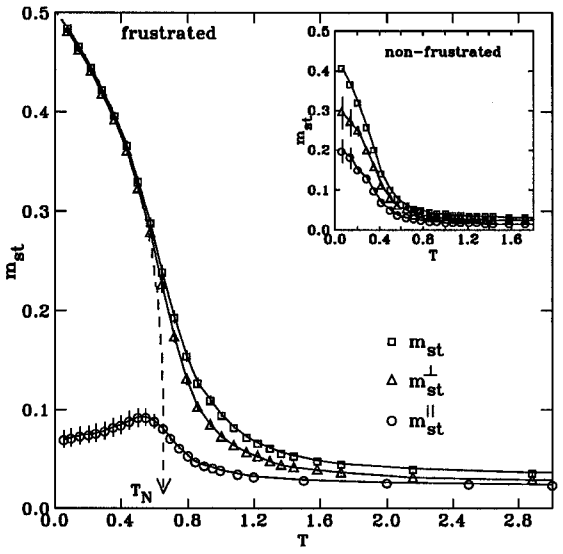

Figure 4.12: Parallel ($m_{st}^{\parallel}$) and perpendicular ($m_{st}^{\perp}$) components of the total staggered magnetization (m_{st}) relative to the magnetization (m_f) for the site frustrated Heisenberg model with x=0.45 for a sc lattice with $L = 10$. The total staggered magnetization is also shown. Inset shows the same data for the non-frustrated model ($J_{FA} = 0$). It is evident that the effect of the J_{FA} bonds is to orient the AF order transverse to the FM order in the mixed phase. Here we have used up to 5×10^6 MCS's to obtain the averages as we must exceed the sample independence times for the vector quantities $\vec{m}_f$ and $\vec{m}_{st}$.

moving the frustration into the interior of the percolating cluster of A sites can be accomplished by considering a non-bipartite lattice such as the fcc lattice.

In the case of Ising spins, site dilute fcc models have been reported to undergo a transition from the ordered AF phase to a spin glass phase[114] with as little as 20% dilution (around $x \sim 0.8$ in Fig. 4.2). Furthermore, the transition to the spin glass phase is accompanied by a change in the nature of the transition; a first order transition for $0.8 < x \leq 1$ changes to a second order transition for $0.2 < x < 0.8$. Beyond x=0.2 no transition is observed which corresponds to the site percolation threshold for A sites in the fcc lattice.

It seems likely that a similar situation exists for the site frustrated Heisenberg model as well. This opinion is based on two observations: (i) the overall similarity between phase diagrams with $J_{FA} = \pm 1$ and those corresponding to dilute magnetism with $J_{FA} = 0$ and (ii) that the pure Heisenberg fcc antiferromagnet orders at finite temperatures[102] $T_N \sim 0.223$. Together with the low value of T_N at (x=1) compared to T_C at $x = 0$ for fcc Heisenberg models, along with the results for the dilute fcc Ising antiferromagnet, we conjecture that the site frustrated Heisenberg model on fcc lattices has a phase diagram as illustrated in Fig. 4.13.

4.2.3 Experimental consequences

The primary motivation for this work was our experimental study of the amorphous alloy a-$(Fe_{1-x}Mn_x)$G[23, 24]. In this alloy, Fe moments couple to neighboring Fe moments ferromagnetically and Mn moments couple to both Fe and Mn antiferromagnetically, hence our choice $J_{FA} = -1$. The magnetic response of this alloy, therefore, may be considered prototypical of a site-frustrated magnet. An important difference between the model and the alloy is the disorder inherent to the glass structure. Despite this difference, many important details of the a-$(Fe_{1-x}Mn_x)$G phase diagram can be understood based upon the model discussed here. For small x the material remains ferromagnetic, and the small concentration of Mn moments order antipar-

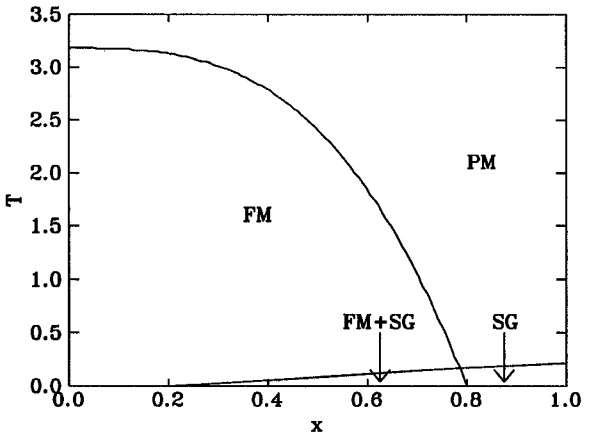

Figure 4.13: A conjectured phase diagram for the fcc site frustrated Heisenberg model. The two end point at x=0 and x=1 corresponding to the pure models are drawn to scale.

allel to the Fe dominated FM order. Beyond a concentration of Mn sites $x \sim 0.2$, spin glass like ordering transverse to the magnetization occurs which is dominated by Mn moments. This concentration corresponds to site percolation of Mn moments for an amorphous alloy[115] with 12 nearest neighbors. Due to structural disorder, the percolating cluster of Mn moments cannot order as a periodic AF and orders as a spin glass.

The transverse nature of the FM and AF order appears to be the only significant consequence of coupling the two types of sites together via J_{FA}. The FM and AF ordering is in no way weakened or destroyed by the frustrated coupling between the two types of sites. This result stands in stark contrast to claims that the ordering behavior of iron-rich a-Fe_xZr_{100-x} alloys is due to competition between finite AF clusters embedded in a FM matrix[29, 30, 31], and that ordering of the AF clusters destroys the pre-existing FM order. While there is now strong experimental evidence against this view[26], the model studied here actually has this specific structure. For compositions where only FM order occurs (x <0.31 for the sc lattice), the model describes a FM matrix with finite AF clusters. The presence of these finite AF clusters, however, does not destroy the pre-existing FM order nor do the AF clusters

order at all.

A similar conclusion holds for models of a-Fe_xZr_{100-x} which claim that finite FM clusters embedded in a FM matrix order randomly at T_{xy}[32, 33, 34, 35, 36, 37, 38, 39], and that the coupling between the clusters and the matrix is frustrated. For compositions where only FM order occurs in our site frustrated model, the model possesses finite AF clusters provided $x > 0$. All of the finite AF cluster may be transformed into a FM cluster by a suitable gauge transformation of the spins on one of the two sublattices of the AF cluster. Such a transformation will change our site frustrated model with finite AF clusters embedded in a FM matrix into a model of finite FM clusters embedded in a FM matrix. The couplings at the interface of the gauge transformed finite FM clusters and the FM matrix will remain frustrated. As we have already seen, these finite FM clusters do not order and so the model cannot explain the ordering observed at T_{xy}.

4.3 Conclusions

We have used Monte Carlo methods to investigate the ordering of Heisenberg spins on sc, bcc and fcc lattices for a site frustrated model. At all concentrations the system forms at least one percolating networks of F or A sites, and in the mixed phase both F and A sites percolate. When both F and A sites percolate on bipartite lattices, they both order as one would expect if the frustration were removed, a fact readily apparent from the similarity between Fig. 4.1 and Fig. 4.2. In the case of the fcc lattice, AF ordering of A sites likely occurs for $0.2 < x < 1$ and so we expect that a tetracritical point should occur here as well. The resulting phase diagrams for frustrated (Fig. 4.1) and non-frustrated models (Fig. 4.2) are closely related, sharing similar, if not the same, critical concentrations. The universality class of the transitions remain in the three dimensional Heisenberg universality class, in agreement with the Harris criteria. The J_{FA} bonds coupling the A and F sites lead only to minor changes in the

ordering:

(i) The transition temperatures are slightly increased (see Fig. 4.8).

(ii) The F and A clusters have mutually perpendicular ordering directions (see Fig. 4.12)

For bipartite lattices, there is a tetracritical point at $x = \frac{1}{2}$ where FM and AF order develop simultaneously in the infinite percolating F and A clusters. The presence of long ranged periodic order at all concentrations allows us to rule out spin glass ordering in these models for bipartite lattices. In the case of fcc lattices we have attempted to detect the ferromagnetic transition only. However by analogy with the sc and bcc lattices we expect that the percolating A cluster undergoes the ordering characteristic of the fully frustrated fcc model.

Chapter 5

Results and discussion for the ±J bond frustrated model

In this chapter we present the phase diagram of the three dimensional ±J bond frustrated model on the simple cubic lattice which results from our Monte Carlo simulations. We begin with the presentation of the zero field phase diagram. We then discuss how we obtain the ferromagnetic phase boundary, $T_C(x)$, followed by the spin glass phase boundary, $T_{SG}(x)$, and then the transverse spin freezing phase boundary, $T_{xy}(x)$. Having established the form of the zero field phase diagram, we apply a magnetic field and follow the dependence of T_{xy} at increasing field.

5.1 Zero field phase diagram

The phase diagram found[11] for the ±J bond frustrated Heisenberg model is shown in Fig. 5.1. The phase diagram is remarkably similar to the mean field phase diagram of Gabay and Toulouse[28]. In contrast to the phase diagrams of site frustrated models, T_C for bond frustrated models declines much more rapidly with increasing x. For instance, at $x = 0.15$ for the bond frustrated model we have $T_C = 0.870(4)$ while at $x = 0.15$ for the site frustrated model on sc lattices we have $T_C \sim 1.38$ (interpolated).

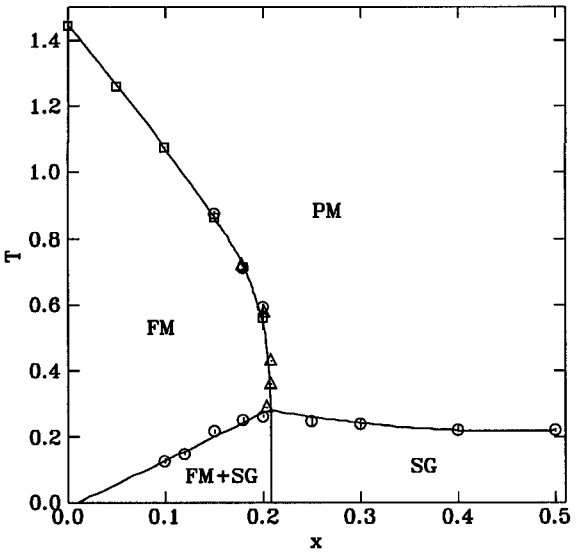

Figure 5.1: Phase diagram of the ±J bond frustrated Heisenberg model. PM is the paramagnetic phase, FM the ferromagnetic phase, and SG the spin glass phase. FM+SG phase is the phase containing ferromagnetic order co-existing with transverse spin glass order. The FM and FM+SG phases are separated by T_{xy}.

The difference can be attributed to there being much more frustration in the bond frustrated model over the site frustrated model at fixed composition; at $x = 0.15$ for the site frustrated model the density of frustrated plaquettes is $x_f^{bond} \sim 0.38$ and at $x = 0.15$ for the site frustrated model $x_f^{site} \sim 0.06$. Long range ferromagnetic order is lost[101] by $x_C = 0.208(2)$, consistent with other estimates[81].

Below T_C we find transverse spin glass order below a finite T_{xy} at all five compositions studied[11]. This phase, like the ferromagnetic phase, is marked by a divergence of the correlation length. The magnetization is not destroyed upon crossing T_{xy}, and continues to increase with decreasing T. The two phases meet at $x \sim 0.21$ and with $T \sim 0.29$, consistent with $x_C = 0.208(2)$. We find that T_{xy} is linear in x and has an intercept at the origin.

For $x > x_C$ we find spin glass order at all four compositions studied. There is a clear but small composition dependence[11] of T_{SG}. At $x = 0.5$, $T_{SG} = 0.220(5)$ which rises to $T_{SG} = 0.246(13)$ at $x = 0.25$. Fitting the data to a parabolic form centered at

$x = 0.5$ shows that the spin glass transition meets the ferromagnetic phase boundary by about $x \sim 0.21$ and $T \sim 0.27$. We estimate that the multi-critical point where T_{SG}, T_{xy} and T_C meet is located approximately at $[T_{cri}, x_{cri}]$=[0.21(1), 0.29(1)] based upon several types of fits. Since the functional form of the three phase boundaries are unknown, we only quote the location of the multi-critical point as an estimate; it is *not* a precise calculation but instead is reasonable estimate given the data shown in the phase diagram. We have drawn a vertical phase boundary below the multi-critical point separating T_{SG} and T_{xy} but we are unable to prove it. Equilibrating a Monte Carlo simulation which measures the ferromagnetic correlation length near x_c and below T_{SG} and T_{xy} is found to be exceedingly difficult and we quickly fall out of equilibrium. However, it is clear that for $T < T_C$ and for $x < x_c$ the ferromagnetic correlation length is divergent while for $T < T_{SG}$ and $x > x_C$ it is not.

5.1.1 The ferromagnetic phase boundary

The pure ($x = 0$) 3d Heisenberg model is among the best understood models of a ferromagnetic material. While it cannot be solved exactly, a wealth of Monte Carlo data exists[82, 83, 99, 116, 117]. The model undergoes a second order phase transition[83] at $T_C = 1.4430(2)$ with $\alpha = -0.11(2)$, $\beta/\nu = 0.514(5)$, $\gamma/\nu = 1.975(4)$, and $\nu = 0.704(6)$. Since $\alpha < 0$, Harris's criteria for weak disorder[73] is satisfied and disorder should not change the values taken by the critical exponents. Our simulations for the pure model[109] at $T_C(0) = 1.4430$ with $L \leq 64$ yield critical exponent ratios of $\beta/\nu = 0.519(8)$ and $\gamma/\nu = 1.965(26)$ in good agreement with precision estimates[83, 82].

We follow the change in T_C that occurs with the random substitution of antiferromagnetic bonds by measuring the location of the crossing of the Binder cumulant (Eqn. 3.17), the maximum slope of the Binder cumulant, the peak in the susceptibility (Eqn. 3.15), and the crossing of the ξ/L curves.

If a second order phase transition occurs at T_C, then we expect $\xi \propto L^{5/2}$ for

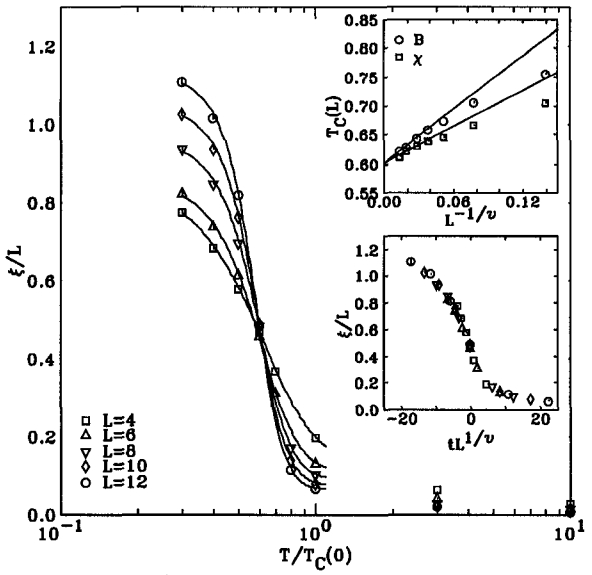

Figure 5.2: The crossing of ξ/L for $x = 0.15$ using $L \leq 12$ as a function of $T/T_C(0)$, with $T_C(0)$ the transition temperature of the pure model. Inset (top) shows the pseudo-transition temperatures as a function of $L^{-1/\nu}$, with $\nu = 0.704$ for the Heisenberg universality class. Inset (bottom) shows the collapse of the ξ/L curves using $T_C(x = 0.15) = 0.867(4)$, obtained from a weighted average of the two intercepts in the top inset, and ν of the Heisenberg universality class. The collapse is surprisingly good for the small system sizes used.

$T \ll T_C$, $\xi \propto L$ for $T = T_C$, and ξ constant for $T \gg T_C$[15]. In Fig. 5.2 we show the crossing of the ξ/L curves. The curves cross at $T_C/T_C(0) = 0.608(5)$, a value obtained by averaging the six locations of the crossing which occur for $L = 6, 8, 10$ and 12 (the $L = 4$ data appear to suffer from L being too small). That there is *no* apparent system size dependence of the crossing point for $L > 4$ can be convincingly demonstrated by measuring T_C in a way which contains large, resolvable L dependent shifts in the pseudo-transition temperatures $T_C(L)$.

In the top inset to Fig. 5.2 we show the peak location of χ_f^c and the maximum slope of the Binder cumulant B_f, both of which scale according to Eqn. 3.33. Here we use $\nu = 0.704$ appropriate for the Heisenberg universality class[82, 83]. We have necessarily used larger system sizes ($L \leq 20$) for these measurements since the data for

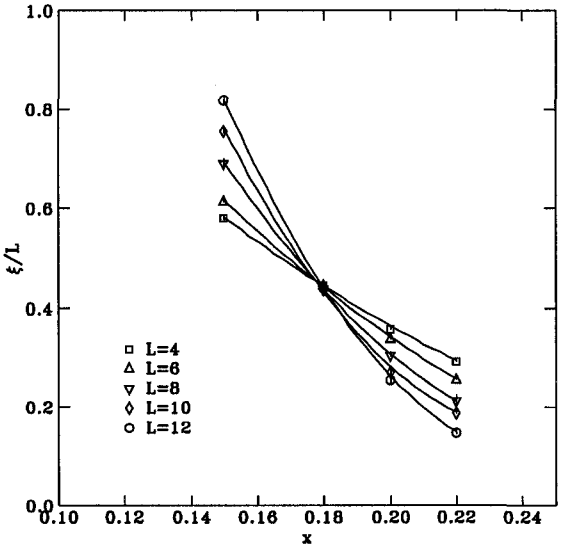

Figure 5.3: The crossing of ξ/L for $T/T_C(0) = 0.5$ using $L = 4, 6, 8, 10, 12$. A clear crossing is observed at $x_C = 0.197(1)$. This estimate should be compared to $T_C(x = 0.18)/T_C(0) = 0.497(1)$ determined from the scaling of the pseudo-transition temperatures and $T_C/T_C(0) = 0.495(2)$ determined from the crossing of the ξ/L data at fixed x.

$L < 10$ obviously suffer from scaling corrections; they do not fall onto a straight line. For $L \geq 10$ both sets of data fall onto two different straight lines with intercepts at T_C. A weighted average of the two intercepts give $T_C/T_C(0) = 0.601(3)$. The agreement between T_C determined by scaling the pseudo-transition temperatures and T_C determined from the crossing of ξ/L, where we neglected any possible L dependence, serves to demonstrate that any finite size shifts in the ξ/L crossing are small.

To construct the ferromagnetic phase boundary shown in Fig. 5.1 we include the following data: (1) T_C determined from the scaling of the pseudo-transition temperatures for $L = 10, 12, 16, 20$, with $x = 0.05, 0.1, 0.15, 0, 18$ and 0.2 (2) the average temperature point at which the ξ/L curves cross with constant x for $L = 6, 8, 10, 12$, with $x = 0.15, 0.18$ and 0.2 and (3) the average concentration point at which the ξ/L curves cross with constant T for $L = 6, 8, 10, 12$, with $T/T_C(0) = 0.5, 0.4, 0.3, 0.25, 0.2$. Method #3 is analogous to the crossing of ξ/L at T_C at constant x shown in Fig. 5.2

Table 5.1: Critical temperatures $T_C(x)/T_C(0)$ as determined in the two methods. Method #1 refers to the scaling of the pseudo-transition temperatures $T_C(L)$ for $L = 10, 12, 16, 20$. Method #2 refers to the crossing of the ξ/L curves for $L = 6, 8, 10, 12$.

	x =0.05	0.10	0.15	0.18	0.20
T_C (Method #1)	0.874(1)	0.745(2)	0.601(3)	0.497(1)	0.390(25)
T_C (Method #2)	–	–	0.608(5)	0.495(2)	0.414(6)

Table 5.2: Critical concentrations x_c determined from the crossing of ξ/L at constant $T/T_C(x = 0)$ (Method #3).

	$T/T_C(0)$ =0.5	0.4	0.3	0.25	0.2
x_C (Method #3)	0.179(1)	0.201(1)	0.208(1)	0.208(1)	0.203(3)

except we take the data at fixed T and find a crossing at x_C as shown in Fig. 5.3. The critical temperatures $T_C(x)$ for methods #1 and #2 are summarized in Table. 5.1 and the critical concentrations from method #3 are summarized in Table. 5.2. Note that at $x = 0.18$ we find from method #1 and method #2, $T_C = 0.497(1)$ and $T_C = 0.495(2)$ respectively (near $T = 0.5$). For method #3 at $T = 0.5$ we find $x_C = 0.179(1)$ (near $x = 0.18$) demonstrating the consistency between the various methods.

Prior to moving on, a discussion of the errors appearing in Tables 5.1 and 5.2 is in order. T_C determined from method #1 is obtained from a weighted average of the two straight line fits through the $T_C(L)$ data, using $L = 10, 12, 16, 20$, as shown in the top inset to Fig. 5.2. T_C determined using method #2 is obtained from a weighted average of the six crossings found for $L = 6, 8, 10, 12$. The temperatures at which the ξ/L data cross are found by fitting ξ/L to a hyperbolic tangent which describe the data appearing in Fig. 5.2 well. This is a three parameter fit to the form

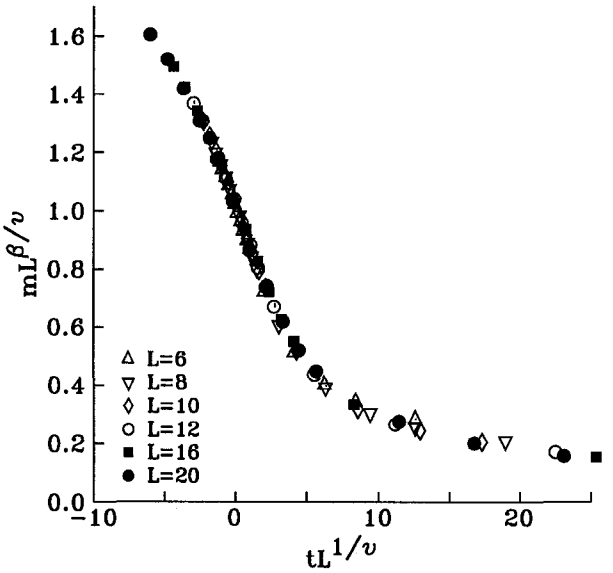

Figure 5.4: Finite size scaling collapse of the magnetization at $x = 0.15$ using exponents of the Heisenberg universality class and $T_C = 0.601 T_C(x = 0)$

$a + b\tanh[c(T - T_C)]$ with T_C determined from Method #1. As the crossing is close to T_C, we linearize about $T - T_C$, propagating the errors on the fitted parameters using standard methods. T_C is determined from method #3 from the crossing of the ξ/L curves for four data points, $x = 0.15, 0.18, 0.20, 0.22$. However, the ξ/L curves, as shown in Fig. 5.3, have significant curvature, and to fit them well we use a second order polynomial $(a + bx + cx^2)$. Clearly, the error on the parameters (a, b, c) are all infinite since we have four data points and we use a three parameter fit. We estimate the errors on each of the six crossing (we neglect the $L = 4$ data) by eye and final errors are determined by an average of the six crossings. Thus, the errors in Table 5.2 are best viewed as estimates rather than calculated errors. The agreement between estimates of x_C determined with Method #3 at $T/T_C(0) = 0.5$ ($x_C = 0.179(1)$) and the estimates of T_C at $x = 0.18$ ($T_C(x = 0.18)/T_C(0) = 0.497(1)$ and $T_C(x = 0.18)/T_C(0) = 0.495(2)$) serves to emphasize that while the error obtained for method #3 is an estimate only, the error estimate is of the correct magnitude.

The phase transition which occurs at T_C is expected to belong to the Heisenberg universality class according to the Harris criteria[73]. As was the case for the site frus-

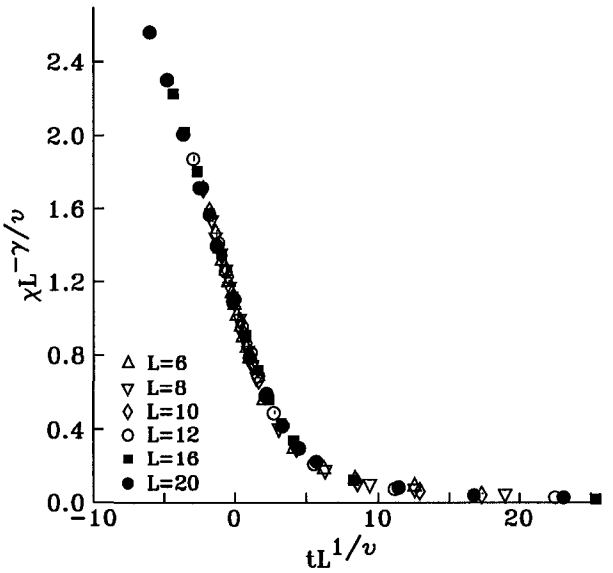

Figure 5.5: Finite size scaling collapse of the susceptibility χ_f^d at $x = 0.15$ using exponents of the Heisenberg universality class and $T_C = 0.601 T_C(x = 0)$

trated model, we are unable to directly measure the critical exponents with sufficient precision to prove this point as the precision required of the transition temperatures would need to be improved by between one and two orders of magnitude. However, scaling plots of m_f (Fig. 5.4) and χ_f^d (Fig. 5.5), along with the scaling plots shown in the insets of Fig. 5.2, and several others not shown, give strong support that this is the case, and the ferromagnetic transition remains in the Heisenberg universality class.

5.1.2 The spin glass phase boundary

To determine the zero field spin glass phase boundary, we have measured the spin glass correlation length ξ_{SG}, a method which has proved the most convincing for Heisenberg spin glass models[7, 8, 9, 10, 11]. As mentioned in Chapter 3, we have not measured the sample independence time for ξ and so we begin with a demonstration that our results are in equilibrium and characteristic of the limit $t \to \infty$. In Fig. 5.6 we show $\xi(T, MCS)$ for the canonical $\pm J$ Heisenberg spin glass ($x = 0.5$) with $L = 10$. This is the smallest size lattice for which we observed a lack of equilibration[10]. At high

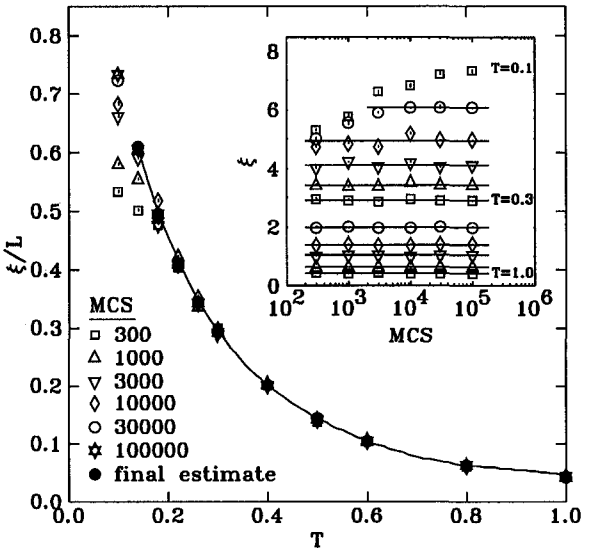

Figure 5.6: ξ/L *vs.* T for different numbers of MCS's used both prior to, and during thermal averaging at $x = 0.5$, $L = 10$. Inset shows ξ *vs.* MCS at various T. Horizontal lines in the inset show the regions used to determine our final averages. No time dependence is observed for $T \geq 0.18$. Where error bars are not apparent, they are smaller than the symbol size.

temperatures ξ is independent of the number of MCS's. Only at low temperatures, $T < 0.18$, do we observe any dependence on the number of MCS's in our calculated ξ. The data at $T = 0.14$ are obviously not equilibrated for either $MCS = 300$ or $MCS = 1000$, but are equilibrated for $MCS \geq 3000$. The lack of equilibration at $T = 0.14$ for small MCS is revealed by the fact that the data remain correlated with the previous measurement at $T = 0.18$, and since the correlation disappears with longer simulations. At $T = 0.1$ we do not observe a clear convergence of ξ; instead ξ continues to increase with increasing simulation time. We compute average values of ξ only for those results which have converged, indicated in the inset of Fig. 5.6 by solid lines. Our final estimates are shown in Fig. 5.6.

As with the case of the ferromagnetic phase boundary, if a second order spin glass phase transition occurs we expect the ξ/L curves to cross at the T_{SG}. We have previously shown for the ferromagnetic transition that T_C found from the crossing of

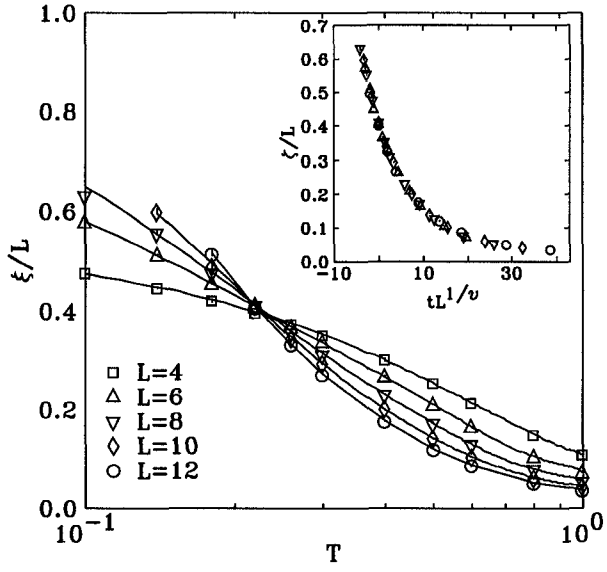

Figure 5.7: Correlation length divided by system size, ξ/L, *vs.* T for different L at $x = 0.5$. A clear crossing is observed at $T_{SG} = 0.220(5)$. Inset shows the scaling of ξ/L with $\nu = 1.04$, and a reduced temperature $t = (T - T_{SG})/T_{SG}$ with $T_{SG} = 0.22$. Where error bars are not apparent, they are smaller than the symbol size.

ξ/L curves agrees with other, more established, methods[68] such as the crossing of the Binder cumulant or the scaling of the pseudo-transition temperatures. Our results for the canonical $\pm J$ Heisenberg spin glass ($x = 0.5$) are shown in Fig. 5.7 and a clear crossing is observed at $T_{SG} = 0.220(5)$. The crossing does not exhibit a noticeable shift with increasing L, except at $L = 4$. This lack of large scaling corrections is not unexpected since, in the case of a Gaussian distribution of bonds, T_{SG} determined[7] with $L \leq 12$ was found to agree with T_{SG} determined using much larger systems[8, 9], $L \leq 32$. A fit to $\log(\xi)$ *vs.* $\log(L)$ at $T = 0.22$, omitting the $L = 4$ data point, yields a slope $s = 1.012(15)$ demonstrating that at $T = 0.22$ we have $\xi \propto L$ as shown in Fig. 5.8, confirming our assignment of T_{SG}.

Our estimate, $T_{SG} = 0.220(5)$, is in agreement with other estimates of finite T_{SG}, namely $T_{SG} = 0.19(2)$[5] and $T_{SG} = 0.22^{+0.01}_{-0.04}$[6] both of which used less established methods than we use here. In the inset to Fig. 5.7 we show the collapse of ξ/L *vs.* T, with the expected finite size scaling form with $\nu = 1.04$. We estimate ν by fitting

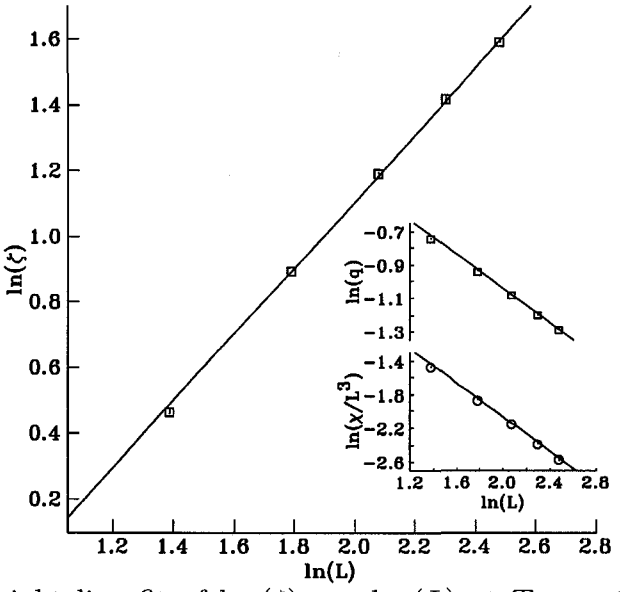

Figure 5.8: Straight line fit of $\log(\xi)$ *vs.* $\log(L)$ at $T_{SG} = 0.22$. The slope is $s = 1.012(15)$, demonstrating that at $T = 0.22$ we have $\xi \propto L$. Inset (a) shows a scaling plot of $\log(q)$ *vs.* $\log(L)$ and inset (b) shows a scaling plot of $log(\chi/L^3)$ *vs.* L. Straight line fits yield estimates $\beta/\nu = 0.509(8)$ and $\gamma/\nu = 1.990(33)$.

the slope of $\xi(L)/L$ at $T_{SG} = 0.22$, omitting the $L = 4$ data point. Our estimate, $\nu = 1.04(6)$, is also consistent with those of the $\pm J$ distribution[5, 6] and for the Gaussian distribution[7] for the same range of system sizes.

At a second order phase transition, we expect that the spin glass order parameter q and the spin glass susceptibility χ_{SG} will behave as

$$q = aL^{-\beta/\nu} \tag{5.1}$$

$$\chi_{SG} = bL^{\gamma/\nu} \tag{5.2}$$

with β, γ, and ν standard critical exponents of the Heisenberg *spin glass* universality class. A fit of $\log(q)$ *vs.* $\log(L)$ at $T_{SG} = 0.22$ yields an exponent ratio $\beta/\nu = 0.509(8)$ while a fit of $\log(\chi_{SG}/N)$ *vs.* $\log(L)$ yields a slope $-1.010(33)$, or $\gamma/\nu = 1.990(33)$ as shown in the insets to Fig. 5.8. The two estimates, however, are very sensitive to the location of T_{SG} and so cannot be considered definitive. Indeed, in the case of the Heisenberg ferromagnet using such small system sizes will yield incorrect exponents[82, 83].

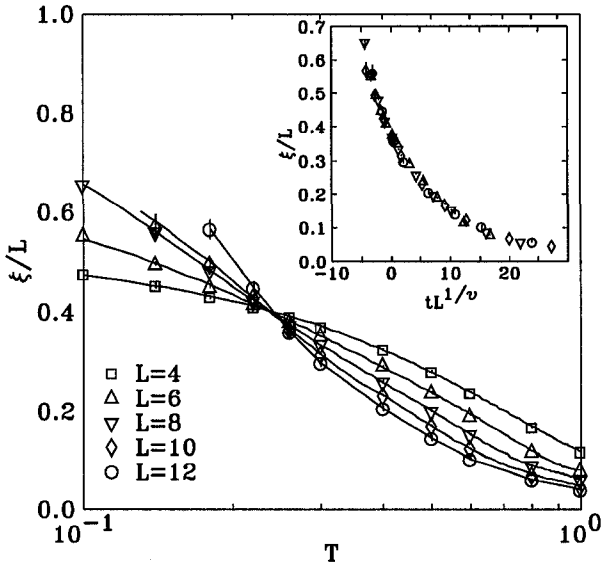

Figure 5.9: Same as Fig. 5.7 except at the concentration $x = 0.25$. A clear crossing is still observed, but it occurs at temperatures slightly above $T_{SG}(x = 0.5) = 0.22$, namely $T_{SG}(x = 0.246) = 0.25(13)$. Inset shows the scaling of ξ/L with $\nu = 1.04$, and a reduced temperature $t = (T - T_{SG})/T_{SG}$ with $T_{SG} = 0.246$. Where error bars are not apparent, they are smaller than the symbol size.

As we decrease the amount of frustration, moving left across the phase diagram towards the FM phase, we find that T_{SG} increases; by $x = 0.25$ it is clear that $T_{SG}(x = 0.25) > T_{SG}(x = 0.5)$. To demonstrate this point we calculate the slope s of $\log(\xi)$ *vs.* $\log(L)$ at $T = 0.22$ for different x. At $x = 0.4$ we get $s = 1.025(25)$, which remains consistent with $T_{SG} = 0.22$. However, at $x = 0.3$ we get $s = 1.049(30)$, and at $x = 0.25$ we get $s = 1.055(13)$. This increase in s with decreasing x at $T = 0.22$ (T_{SG} for $x = 0.4, 0.5$) indicates that $T_{SG}(x)$ is also increasing. In fact, the crossing point in the curves of ξ/L show that by $x = 0.25$ T_{SG} has moved to 0.246(13), as shown in Fig. 5.9.

The spin glass transition temperatures are again determined from a weighted average of the six crossings observed for $L \geq 6$. We determine the crossing by fitting ξ/L to a quadratic equation $(a + bx + cx^2)$ which describes the data in the vicinity of the crossing well. Typically we use between 5 and 6 points from $0.18 \leq T \leq 0.3$. Error

Table 5.3: T_{SG} determined from a weighted average of the six observed crossings, ignoring the $L = 4$ data.

	x=0.25	0.3	0.4	0.5
T_{SG}	0.246(13)	0.241(14)	0.223(8)	0.220(5)

estimates for each crossing are determined by standard error propagation techniques. The resulting transition temperatures are are plotted in the phase diagram in Fig. 5.1 and appear in Table. 5.3

5.1.3 The transverse spin glass phase boundary

Turning to the transverse spin glass phase existing below the ferromagnetic phase boundary, we show $\xi_{xy}(T, MCS)$ at $x = 0.15$ with $L = 10$ in Fig. 5.10. Unlike the pure spin glass, we find no time dependence in ξ_{xy}, except for $L = 12$ and $T < \frac{3}{4}T_{xy}$. Other quantities such as the internal energy, $[< |q_{xy}| >]$ and $[< m >]$, in addition to having no MCS dependence, also show much smaller compositional fluctuations than ξ_{xy}. As was the case with for the spin glass, we make final estimates of ξ_{xy} by averaging the data at a particular T as indicated by solid lines in the inset to Fig. 5.10.

In Fig. 5.11 we show the crossing obtained for $x = 0.15$, for $L \geq 6$. We have determined the crossing point by fitting the data to a quadratic polynomial $(a + bx + cx^2)$, as was the case for the spin glass phase existing for $x > x_c$. The solid lines show the fits, and a clear and unambiguous crossing is observed just below $T = 0.22$. Similar crossings are observed for the other compositions. The critical temperatures obtained for each of the five compositions are listed in Table 5.4.

In Fig. 5.12 we show the crossing of ξ_{xy}/L for the five compositions studied here. The crossing point in ξ_{xy}/L, which we ascribe to the ordering of the transverse spin glass at T_{xy} (*ie.* the GT line), has a much more significant x dependence than that

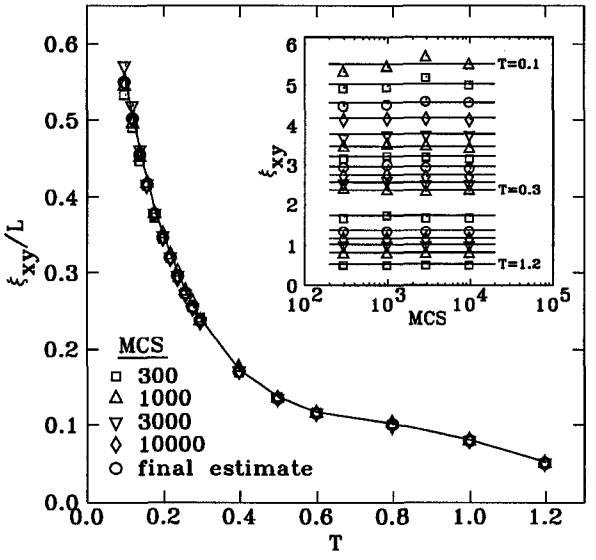

Figure 5.10: ξ_{xy}/L *vs.* T for different numbers of MCS's used both prior to, and during thermal averaging at $x = 0.15$, $L = 10$. Inset shows ξ_{xy} *vs.* MCS at various T. Horizontal lines in the inset show the regions used to determine our final averages. No time dependence is observed, even for as few as 300 MCS's. Where error bars are not apparent, they are smaller than the symbol size.

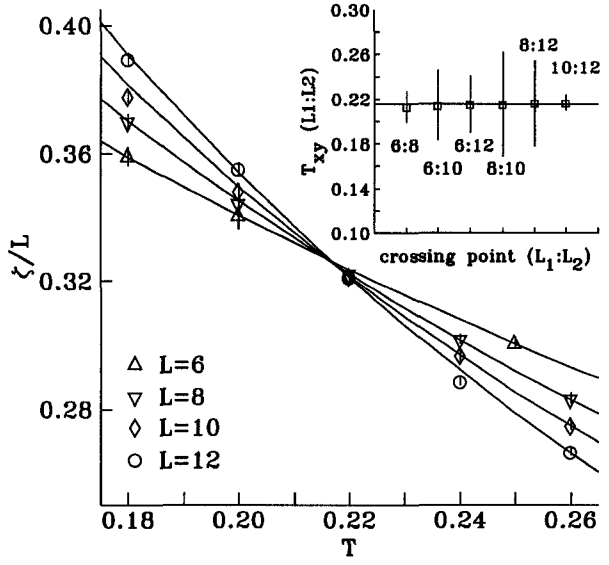

Figure 5.11: The crossing of ξ_{xy}/L at $x = 0.15$ for $L \geq 6$. A clear crossing is observed just below $T = 0.22$. As shown in the inset, the crossing point for different L_1 and L_2 pairs do not appear to suffer from any noticeable scaling corrections; all of the data cross at a single temperature, T_{xy}=0.216(5), within error as shown by the solid line.

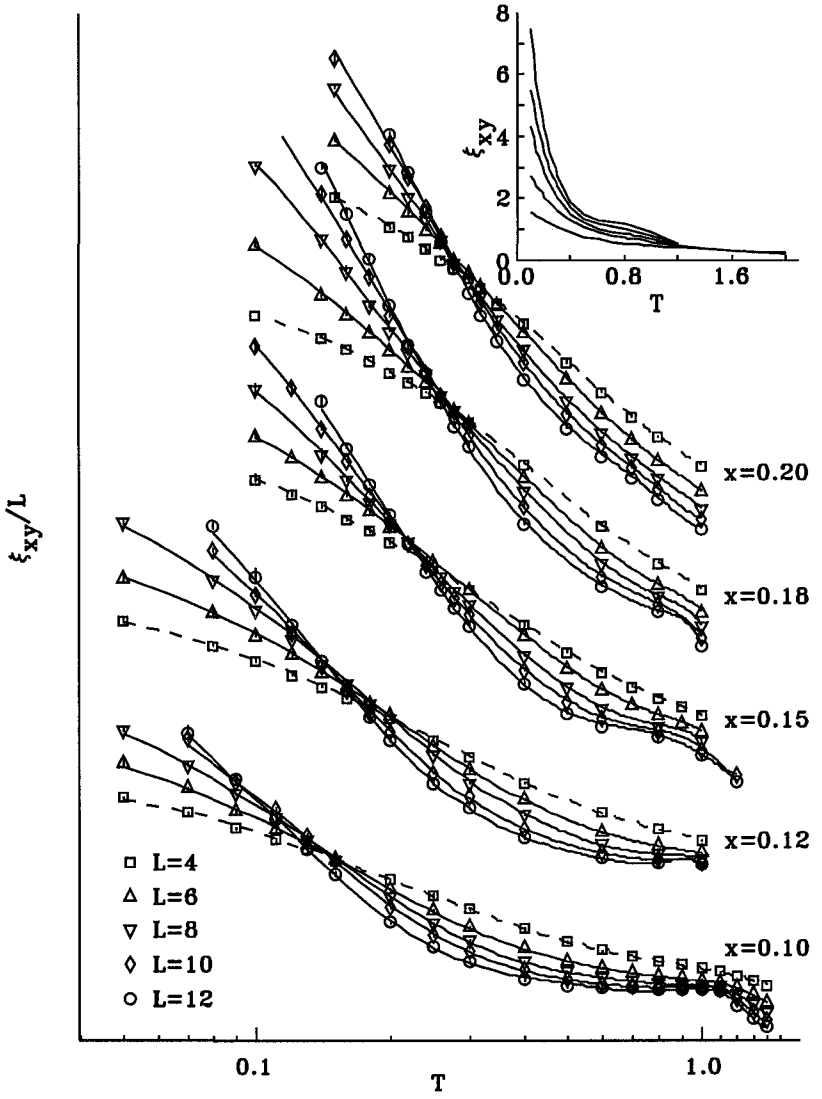

Figure 5.12: Crossing of the ξ_{xy}/L curves for $L = 4, 6, 8, 10$ and 12 for concentrations $x = 0.20, 0.18, 0.15, 0.12$ and $x = 0.10$ (curves have been shifted to fit plotting area). Solid lines through $L > 4$ data show clear crossings, while the dashed line through the $L = 4$ data cross at higher T. Inset shows ξ_{xy} for $x = 0.15$, which shows a non-divergent increase at T_C prior to T_{xy}. Where error bars are not apparent, they are smaller than the symbol size.

Table 5.4: T_{xy} determined from a weighted average of the six observed crossings, ignoring the $L = 4$ data.

x=	0.10	0.12	0.15	0.18	0.20
T_{xy}	0.128(7)	0.150(4)	0.216(5)	0.251(7)	0.262(5)

of T_{SG}. To an excellent approximation T_{xy} is *linear* in x and passes through the origin. A fit to the form $T_{xy} = a + bx$ yields $a = 0.01(3)$ and $b = 1.4(2)$, consistent with T_{xy} vanishing at $x = 0$. Furthermore, as shown in the inset to Fig. 5.12, there is a notable increase in ξ_{xy} upon crossing T_C, due to a softening of the transverse ferromagnetic modes. It is important to note that while there is a rapid increase in $[< q_{xy} >]$ below T_{xy}, we do *not* observe *any* loss of ferromagnetic order: The spin glass and ferromagnetic order co-exist below T_{xy}.

In Fig. 5.13 we show the development of the spin glass order $[< q_{xy} >]$, which shows behavior typical of an order parameter on passing through a finite temperature phase transition. For temperatures above T_{xy}, $[< q_{xy} >]$ scales with increasing L to zero. For temperatures below T_{xy}, $[< q_{xy} >]$ scales with increasing L to a non-zero value. That $[< q_{xy} >]$ is non-zero for $T < T_{xy}$ is clearly observed at the lowest temperature shown in Fig. 5.13 where $[< q_{xy} >]$ is in fact increasing with increasing L, and is almost saturated by $L = 12$. At T_{xy} we observe the same $L^{-\beta/\nu}$ scaling of $[< q_{xy} >]$ as was observed for the pure spin glass at $x = 0.5$. We show in the inset to Fig. 5.13 the scaling of the transverse spin glass order parameter using the same exponents which were found for the pure spin glass at $x = 0.5$, namely $\beta/\nu = 0.509$ and $\nu = 1.04$. However, we again stress that with the small system sizes used in our simulations, the estimates of the critical exponents for the spin glass transitions may not be characteristic of the thermodynamic limit.

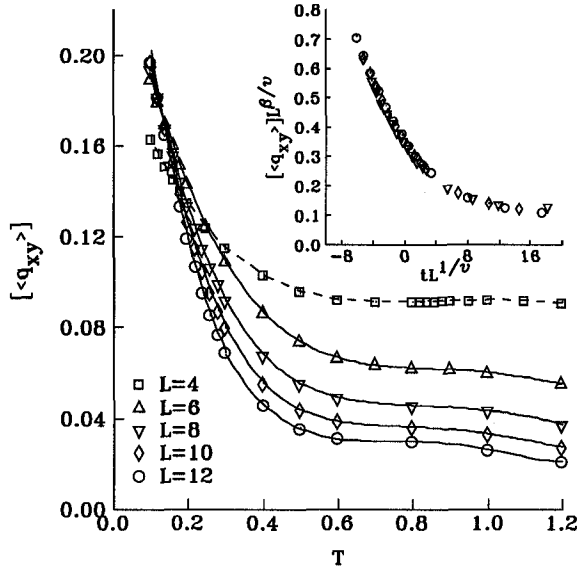

Figure 5.13: Transverse spin glass order parameter $[< q_{xy} >]$ *vs.* temperatures T at $x = 0.15$. Note that at $T = 0.1$, $[< q_{xy} >]$ is increasing with increasing L demonstrating that in the thermodynamic limit, $[< q_{xy} >]$ is finite below $T_{xy} = 0.216(5)$. The inset shows the scaling of $[< q_{xy} >]L^{\beta/\nu}$ *vs.* $tL^{1/\nu}$, with $\beta/\nu = 0.509$ and $\nu = 1.04$. The data for $L = 4$ is excluded from the plot.

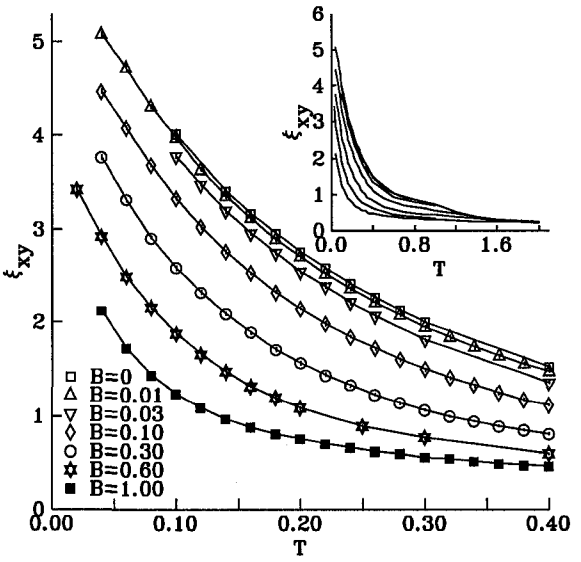

Figure 5.14: Main plot shows the changes in ξ_{xy}(T) with increasing B at $x = 0.15$ with $L = 8$. The inset shows the same data over a wider range of temperatures. At high temperatures ξ_{xy} is a constant, independent of B. At low temperatures ξ_{xy} is reduced with increasing B. Where errors are not apparent, they are smaller than the symbol size.

5.2 The dependence of T_{xy} on an externally applied magnetic field

To determine the dependence of T_{xy} on an externally applied magnetic field B, we have measured ξ_{xy}/L for six fields spanning $0 \leq B \leq 1$ for a concentration $x = 0.15$. The presence of a magnetic field removes the ferromagnetic phase transition entirely, but the transverse spin glass phase transition at T_{xy} is expected to remain at finite temperatures since the order parameter is transverse to the applied field. The situation is expected to be similar to Heisenberg antiferromagnets in an applied field[113], where a finite temperature transition at T_N remains at all fields, and $T_N \rightarrow 0$ with $B \rightarrow \infty$. This is opposite of the case with Ising antiferromagnets[103] where there is a critical field B_c beyond which $T_N = 0$.

In Fig. 5.14 we show ξ_{xy} with increasing B at a concentration $x = 0.15$ with

$L = 8$. The data shown is typical for all L studied. At high temperatures the spin system does not feel the effects of the magnetic field; thermal disorder dominates and ξ_{xy} is a constant. With decreasing temperature we observe an increasing ξ_{xy} for all fields, although the temperature where ξ_{xy} begins to rise rapidly is pushed to lower temperatures. ξ_{xy} is clearly suppressed with increasing field strength.

The increase in ξ_{xy} observed around T_C in zero field is eliminated with only moderate fields at $L = 8$, even though there is no ferromagnetic phase transition. With larger L, this increase in ξ_{xy} near the zero field T_C is eliminated with progressively smaller fields, demonstrating that for finite B this feature is an artifact of using finite lattices. The reason we still observe an increase in ξ_{xy} around the zero field ferromagnetic phase transition with $B \neq 0$, despite the fact that with $B \neq 0$ T_C is technically non-existent, can be understood as follows: In the limit $L \rightarrow \infty$, the ferromagnetic correlation length grows with decreasing T but is strictly finite. When the ferromagnetic correlation length of the infinite lattice becomes larger than our finite lattice size L, the spin system behaves as if a ferromagnetic transition has occurred. Therefore, this feature in ξ_{xy} associated with the zero field T_C disappears with increasing L as observed.

In Fig. 5.15 we show the crossing of the ξ_{xy}/L data for B =0, 0.01, 0.03, 0.1, 0.3, 0.6 and 1. The crossing points are clearly occurring at lower temperatures as B increases. We again determine T_{xy} by fitting ξ_{xy}/L data for different L in the vicinity of T_{xy} to a second order polynomial. Unlike the zero field data, we find that the crossing point is shifted towards higher temperatures not only for $L = 4$, but also for $L = 6$. For $L = 8$, 10, and 12 the crossings do not shift in a systematic way with increasing L. This behavior is shown in Fig. 5.16 for $B = 0.3$, where a clear crossing for $L = 8$, 10, and 12 is observed at $T_{xy} = 0.085(3)$. The transition temperatures derived from the ξ_{xy}/L crossings are summarized in Table 5.5. We emphasize that the data appearing in the Table may change as we have yet to obtain all 500 disorder configurations for the larger lattices with $L = 10$ and $L = 12$, as was explained in

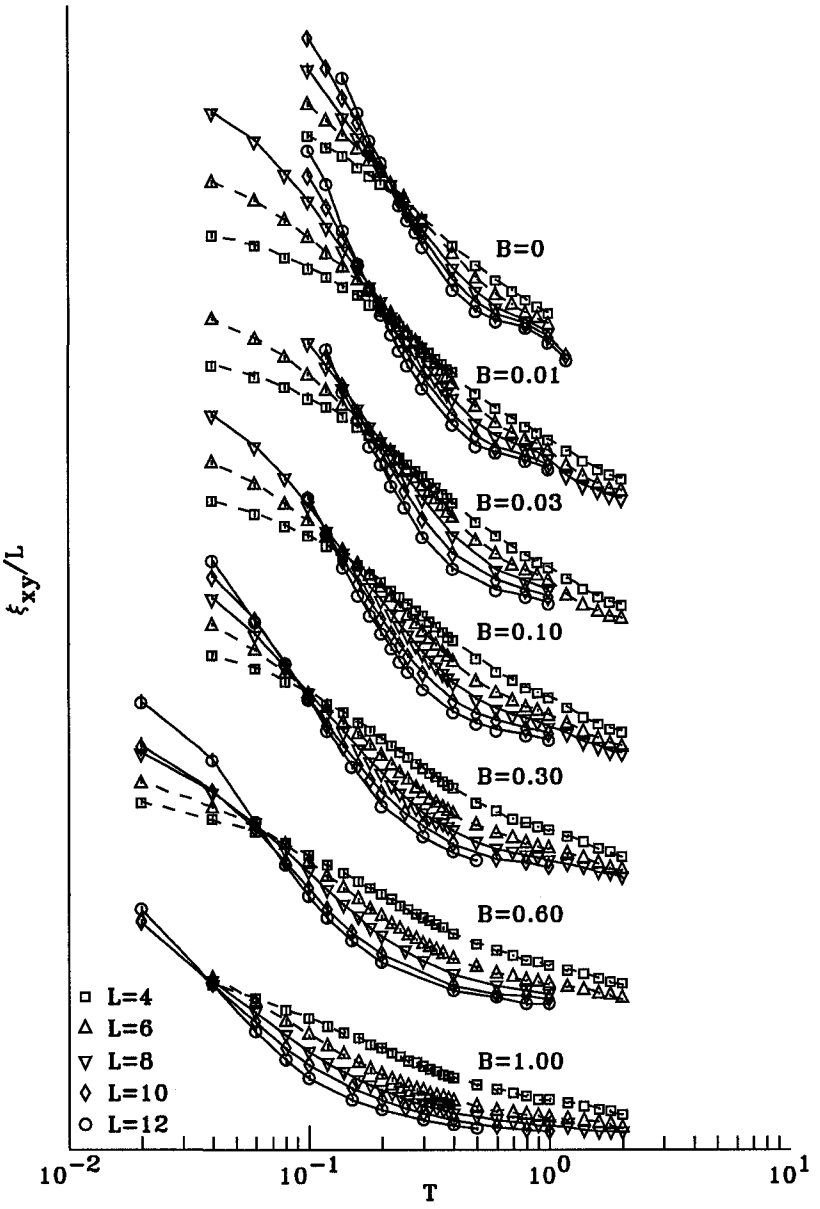

Figure 5.15: Crossing of the ξ_{xy}/L data for $L = 4, 6, 8, 10$ and 12 for a concentration x =0.15, with magnetic fields B =0, 0.01, 0.03, 0.1, 0.3, 0.6 and 1 (data have been shifted to fit plotting area). Solid lines through $L > 6$ data show clear crossings, while the dashed line through the L =4 and L =6 data cross at higher T. Where error bars are not apparent, they are smaller than the symbol size.

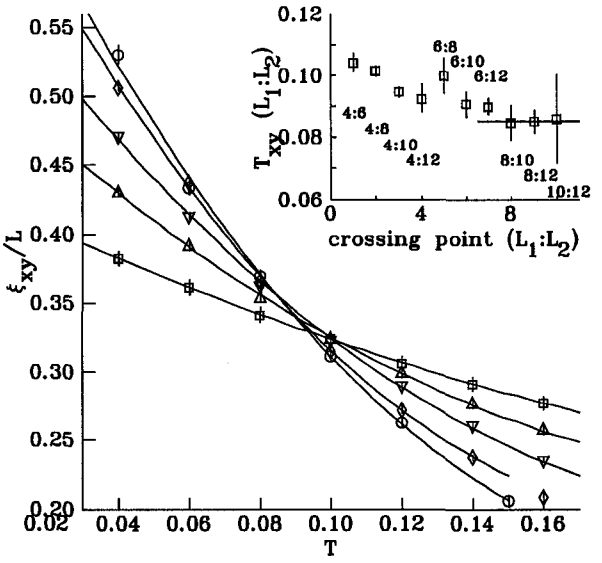

Figure 5.16: Main plot shows the changes in ξ_{xy}(T) with increasing B at $x = 0.15$ with $L = 8$. The inset shows the same data over a wider range of temperatures. At high temperatures ξ_{xy} is a constant, independent of B. At low temperatures ξ_{xy} is reduced with increasing B.

Table 5.5: T_{xy} *vs.* B at $x = 0.15$ determined from a weighted average of the three ξ_{xy}/L crossings observed for L =8,10, and 12.

B=	0.01	0.03	0.10	0.30	0.60	1.00
T_{xy}	0.184(5)	0.164(8)	0.122(4)	0.085(3)	0.055(6)	0.030(15)

Chapter 3, and noted in Table 3.2.

In Fig. 5.17 we have plotted the crossing temperatures from Table 5.5 along with a fit to the form $T_{xy}(B) = T_{xy}(0)\left(1 - \frac{B}{B+J}\right)$, (Eqn. 1.4). This is the same equation which was found to successfully describe the behavior of T_{xy} in a magnetic field in our experiments. None of the mean field predictions describes our data as well as Eqn. 1.4. In particular, Eqn. 1.1 is concave down and so cannot describe our data which is concave up. Eqn. 1.2 is concave up, but the function is not steep enough to account for our observations. The mean field behavior at high fields, Eqn. 1.3

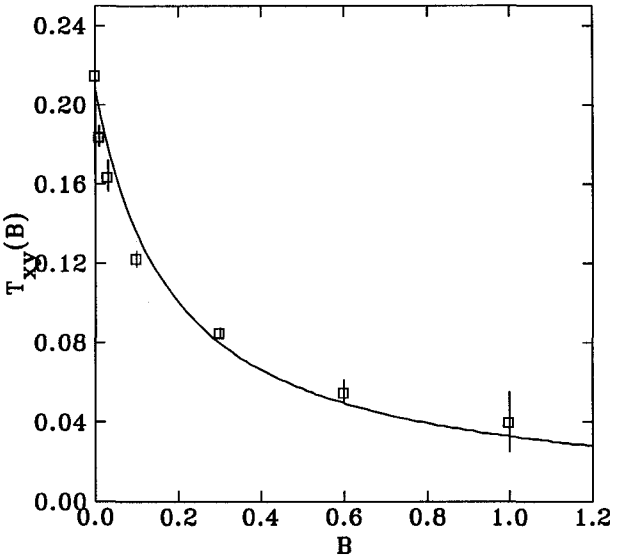

Figure 5.17: T_{xy} as a function of magnetic field B at $x = 0.15$ determined from the crossing of the ξ_{xy}/L data. The straight line is a fit to Eqn. 1.4.

does not even come close to fitting the data. Only Eqn. 1.4 is found to fit the data acceptably.

5.3 Discussion

Our findings for the zero field phase diagrams are in qualitative agreement with mean field theory with regards to the bulk phases found. For low levels of frustration we find a ferromagnetic phase below T_C. T_C decreases with increasing amounts of frustration, and by $x_c \sim 0.21$ ferromagnetism is lost entirely. For all concentrations $0 < x < x_c$ we observe spin glass order in the plane perpendicular to the ferromagnetic order. This results suggests that for any finite amount of bond frustration, a ferromagnet should possess a low temperature transverse spin glass phase. For $x > x_c$ we find a finite temperature T_{SG}. Our phase diagram (Fig. 5.1) does not possess the AT line found in the mean field phase diagram (Fig. 1.4). However, we have not attempted to determine whether replica symmetry breaking occurs. All of the transitions observed in bond frustrated materials, T_c, T_{xy}, and T_{SG}, are found to occur at finite

temperatures in our simulations of the bond frustrated Heisenberg model.

While our results indicate a finite T_{SG} for the bond frustrated Heisenberg model in three dimensions with $\pm J$ interactions, based on the fact that ξ/L crosses at a finite T_{SG}, recent work on very large ($L \leq 32$) lattices for the Heisenberg spin glass model with Gaussian interactions suggests that the transition may in fact be more exotic[8]. It was shown that with increasing L one could not rule out a situation where $1/\nu = 0$ in the limit $L \rightarrow \infty$, and that a transition akin to the Kosterlitz-Toulouse (KT) transition[118] occurring in the two dimensional xy ferromagnet may also occur at T_{SG}. In this scenario, the Heisenberg spin glass in three dimensions is proposed to be exactly at its lower critical dimension d_l, yet T_{SG} remains *finite*[8, 9, 119]. If so, one expects that the crossing we observe for ξ/L will, with larger L, become a merger[8, 15] in which case ξ/L is a constant for all $T < T_{SG}$. Further work[9] demonstrates that using system sizes $L \leq 32$, one cannot distinguish unambiguously between a situation where the Heisenberg spin glass is just above its lower critical dimension ($d_l < 3$), in which case ξ/L crosses, or if the model is exactly at its lower critical dimension ($d_l = 3$), in which case ξ/L merges below a finite T_{SG}. The situation remains unresolved.

The possibility that a KT like transition occurs and $d_l = 3$ has important consequences for both the theoretical study of the model and for the interpretation of experiments. As far as theory is concerned, the existence of a KT like transition at finite T_{SG} implies that $1/\nu = 0$. If $1/\nu = 0$, it would explain the lack of scaling corrections we observe in the crossing of ξ/L since the temperature shift of the crossing point with increasing L should scale like $L^{-1/\nu}$. The fact that T_{SG} determined with $L \leq 12$[7] is in agreement with T_{SG} with $L \leq 32$[8, 9] for the Heisenberg spin glass model with Gaussian interactions serves to demonstrate that a shift in T_{SG} with increasing L is either small ($1/\nu$ is small and $d_l < 3$) or non-existent ($1/\nu$ is zero and $d_l = 3$). From an experimental standpoint, a KT like transition may explain the lack of a divergent fluctuation peak at both T_{SG} and T_{xy}. However, it is not clear what

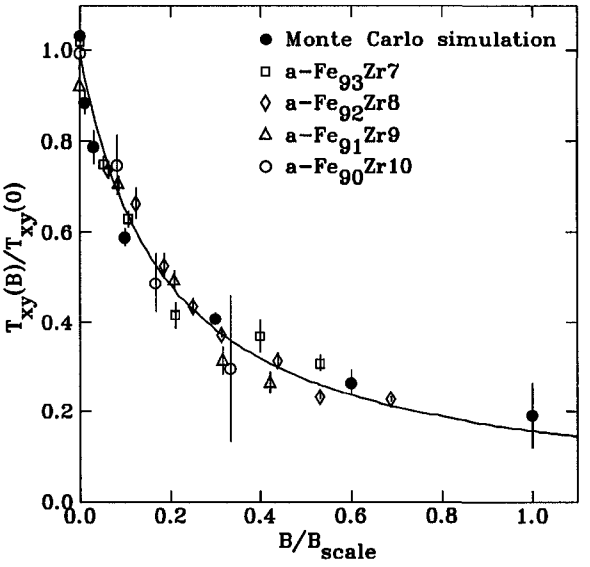

Figure 5.18: A comparison of the $T_{xy}(B)$ obtained from our Monte Carlo simulations and $T_{xy}(B)$ obtained from our experiments on a-$Fe_{100-x}Zr_x$.

the fluctuation peak observed in μSR experiments should look like were the materials exactly at their lower critical dimension with respect to spin glass order.

Our results for the for magnetic field dependence of T_{xy} are also in good agreement with our experiments on a-$Fe_{100-x}Zr_x$. We find that T_{xy} for both the model and the material are well described by a $1/B$ functional form. Our results are not in agreement with any of the mean field predictions, which is unsurprising. The fit of the $T_{xy}(B)$ Monte Carlo data to the $1/B$ form, however, is not perfect. It appears, at present, that T_{xy} determined from our Monte Carlo simulations at small B is slightly below the fitted line while at large B the data is slightly above the fitted line. The simulation data, however, is not yet entirely complete, and our results for $T_{xy}(B)$ may change slightly and bring our data closer to the $1/B$ scaling we have found for real materials. Alternatively, we can not rule out the possibility that the correct functional form for $T_{xy}(B)$ may be different than Eqn. 1.4, and that the $1/B$ form is just an excellent approximation to a different and more complex functional form. Indeed, this possibility seems quite likely.

The data is, however, in remarkably good agreement with our experiments inde-

pendent of the precise functional form of $T_{xy}(B)$. We show this agreement in Fig. 5.18 where we have plotted our Monte Carlo data along with the experimental data for a-$Fe_{100-x}Zr_x$. In the plot we have normalized the simulation data and the experimental data to coincide at $B = 0$, while we have also scaled the magnetic fields in the experimental data so that the fitted curves to $T_{xy}(B)$ agree. The excellent agreement between the experimental data and the simulation data provides strong evidence that the ordering taking place in the material is a consequence of bond randomness and frustration only, as these are the only two ingredients included in the model.

5.4 Conclusions

In summary, we have studied the phase diagram of the $\pm J$ Heisenberg spin glass model in three dimensions with nearest neighbor interactions. We find all of the bulk phases predicted by GT, including the mixed phase where spin glass order and ferromagnetism co-exist. We find that T_{SG} is composition dependent, contrary to the mean field prediction. Our results indicate that T_{xy} extrapolates to zero at $x = 0$, which implies that for even infinitesimal amounts of frustration, the model has two transitions, namely ferromagnetic and transverse spin glass transitions. We have located the multi-critical point where T_C, T_{SG}, and T_{xy} merge. Furthermore, we have measured the field dependence of T_{xy} and we find perfect agreement between the behavior of the model and the behavior of real materials. Our phase diagram for a realistic spin glass model with short range interactions demonstrates that the phases found in the mean field theory of Gabay and Toulouse survive at finite temperatures in three dimensions, and that the behavior observed in experiments on partially frustrated ferromagnets is found in a simple spin glass model.

Chapter 6

Conclusions

We have investigated the phase diagrams of site frustrated and bond frustrated Heisenberg models in three dimensions with short range interactions. Our results show that for the site frustrated models, spin glass order is not realized for bipartite lattices. We have found that ferromagnetic order occurs whenever ferromagnetic sites percolate, and that antiferromagnetic order occurs whenever antiferromagnetic sites percolate for bipartite lattices. For fcc lattices we conjecture that the geometrically frustrated percolating cluster of antiferromagnetic sites orders as a spin glass with sufficient randomness, as seen for dilute Ising fcc antiferromagnets.

Our studies of the model help to explain the ordering which occurs in our experimental phase diagram for a-$(Fe_{1-x}Mn_x)_{78}Si_8B_{14}$. For small x, ferromagnetic order occurs and the magnetization decreased proportional to the Mn moment. At $x \sim 0.17$ and beyond, antiferromagnetic Mn sites percolate and order as a spin glass because the glass structure of the material cannot support antiferromagnetic order. The loss of ferromagnetic order at $x \sim 0.31$ cannot be explained by our model. The most likely reason ferromagnetic order is lost well before the expected concentration $x \sim 0.87$ is that the Fe sites have a concentration dependent magnetic moment which is lost at $x \sim 0.31$.

In the case of bond frustrated models we find spin glass order occurs at a finite

transition temperature T_{SG} for the simple cubic lattice. We also find transverse spin glass order at finite transition temperature T_{xy}. The transverse spin glass phase coexists with ferromagnetism which occurs below T_C. The three bulk ordered phases we find are the same as those predicted within mean field theory. We have not attempted to measure the AT line where replica symmetry breaking occurs.

The phase diagrams of the bond frustrated model has all of the phases found in experiments on bond frustrated materials. To further test the applicability of the model to the materials we have measured the magnetic field dependence of T_{xy} in a-$Fe_{100-x}Zr_x$ for four different concentrations. The agreement between $T_{xy}(B)$ determined in our experiments and $T_{xy}(B)$ determined in our Monte Carlo simulations is striking, and serves to emphasize that the only physics governing the phase diagrams of these magnetic materials is randomness and bond frustration.

6.1 Further work

While we have resolved many of the issues regarding the phase diagrams of bond and site frustrated models and materials, two important questions remain unanswered: (i) For site frustrated models, does the percolating cluster of antiferromagnetic sites for fcc lattices order as a spin glass? (ii) For bond frustrated models, are the finite temperature transitions at T_{xy} and T_{SG} similar to KT transitions in two dimensional xy ferromagnets, and if so is this fact revealed by the non-divergent peak in λ observed in our μSR experiments? In both cases, Monte Carlo simulations will play a large role along with experiments. The first question, if answered in the affirmative, begs for more experiments and simulations on site frustrated materials and models which measure $T_{xy}(B)$ and $T_{SG}(B)$ in order to determine whether the spin glass transition observed in the models is applicable to the study of real materials, similar to the demonstration given here for the bond frustrated model and materials. The second issue requires simulations on larger lattices in order to unambiguously determine what

the lower critical dimension of the model is. In addition, it is important to determine how the μSR fluctuation peak should behave were three dimensional Heisenberg spin glasses at their lower critical dimension with a finite temperature transition.

Bibliography

[1] H. Kawamura and M. Tanemura, Phys. Rev. B **36**, 7177 (1987).

[2] H. Kawamura, Phys. Rev. Lett. **80**, 5421 (1998).

[3] K. Hukushima and H. Kawamura, Phys. Rev. E **61**, R1008 (2000).

[4] F. Matsubara, T. Shirakura, and S. Endoh, Phys. Rev. B **64**, 092412 (2001).

[5] S. Endoh, F. Matsubara, and T. Shirakura, J. Phys. Soc. Jpn. **70**, 1543 (2001).

[6] T. Nakamura and S. Endoh, J. Phys. Soc. Jpn. **71**, 2113 (2002).

[7] L. W. Lee and A. P. Young, Phys. Rev. Lett. **90**, 227203 (2003).

[8] I. Campos *et al.*, Phys. Rev. Lett. **97**, 217204 (2006).

[9] L. W. Lee and A. P. Young, Phys. Rev. B **76**, 024405 (2007).

[10] A. D. Beath and D. H. Ryan, J. Appl. Phys. **101**, 09D506 (2007).

[11] A. D. Beath and D. H. Ryan, Phys. Rev. B **76**, 064410 (2007).

[12] D. H. Ryan, in *Recent Progress in Random Magnets*, edited by D. H. Ryan (World Scientific, Singapore, 1992), pp. 1–40.

[13] K. H. Fischer, *Spin Glasses* (Cambridge University Press, New York, 1993).

[14] K. Binder and A. P. Young, Reviews of Mod. Phys. **58**, 801 (1986).

[15] H. G. Ballesteros *et al.*, Phys. Rev. B **62**, 14237 (2000).

[16] A. T. Ogielski, Phys. Rev. B **32**, 7384 (1985).

[17] J. Mydosh, *Spin Glasses: An experimental introduction* (Taylor & Francis, Washington, 1993).

[18] P. Granberg, L. Lundgren, and P. Norblad, J. Magn. Magn. Mater. **92**, 228 (1990).

[19] G. H. Wannier, Phys. Rev. **79**, 357 (1950).

[20] J. M. Luttinger, Phys. Rev. **81**, 1015 (1950).

[21] A. D. Beath and D. H. Ryan, Phys. Rev. B **73**, 214445 (2006).

[22] D. H. Ryan, Z. Tun, and J. M. Cadogan, J. Magn. Magn. Mater. **177–81**, 57 (1998).

[23] D. H. Ryan *et al.*, Phys. Rev. B **67**, 104404 (2003).

[24] A. Kuprin, D. Wiarda, and D. H. Ryan, Phys. Rev. B **61**, 1267 (2000).

[25] H. Ren and D. H. Ryan, Phys. Rev. B **51**, 15885 (1995).

[26] D. H. Ryan, J. M. Cadogan, and J. van Lierop, Phys. Rev. B **61**, 6816 (2000).

[27] D. H. Ryan, J. M. Cadogan, and J. van Lierop, Phys. Rev. B **62**, 8638 (2000).

[28] M. Gabay and G. Toulouse, Phys. Rev. Lett. **47**, 201 (1981).

[29] H. Hiroyoshi and K. Fukamichi, J. Appl. Phys. **53**, 2226 (1982).

[30] N. Saito, H. Hiroyoshi, K. Fukamichi, and Y. Nakagawa, J. Phys. F: Met. Phys. **16**, 911 (1986).

[31] D. A. Read, G. C. Hallam, and M.Chirwa, J. Magn. Magn. Mater. **82**, 83 (1989).

[32] S. N. Kaul, J. Phys. F: Met. Phys. **18**, 2089 (1988).

[33] S. N. Kaul, J. Phys.: Cond. Matter **3**, 4027 (1991).

[34] S. N. Kaul, C. Bansal, T. Kumaran, and M. Havalgi, Phys. Rev. B **38**, 9248 (1988).

[35] V. Siruguri, S. N. Kaul, G. Rajaram, and G. Chandra, An. Fis. Ser. B **86**, 181 (1990).

[36] S. N. Kaul, J. Appl. Phys. **61**, 451 (1987).

[37] S. N. Kaul and V. Siruguri, An. Fis. Ser. B **86**, 70 (1990).

[38] S. N. Kaul, J. Phys.: Cond. Matter **4**, 505 (1992).

[39] S. N. Kaul, J. Phys.: Cond. Matter **3**, 4027 (1991).

[40] D. H. Ryan *et al.*, Phys. Rev. B **35**, 8630 (1987).

[41] D. H. Ryan, in *Magnetic Properties of Amorphous Metals*, edited by A. Hernando, V. Madurga, M. Sanchez-Trujillo, and M. Vazquez (Elsevier, Amsterdam, 1987).

[42] D. H. Ryan, J. O. Ström-Olsen, R. Provencher, and M. Townsend, J. Appl. Phys. **64**, 5787 (1988).

[43] J. van Lierop and D. H. Ryan, Phys. Rev. Lett. **86**, 4390 (2001).

[44] D. H. Ryan *et al.*, Phys. Rev. B **63**, 140405 (2001).

[45] D. H. Ryan, J. M. Cadogan, and J. van Lierop, Phys. Rev. B **65**, 176402 (2002).

[46] J. R. Banavar and M. Cieplak, Phys. Rev. Lett. **48**, 832 (1982).

[47] W. L. McMillan, Phys. Rev. B **31**, 342 (1985).

[48] J. A. Olive, A. P. Young, and D. Sherrington, Phys. Rev. B **34**, 6341 (1986).

[49] I. Mirebeau *et al.*, Hyp. Int. **104**, 343 (1997).

[50] S. F. Edwards and P. W. Anderson, J. Phys. F: Met. Phys. **5**, 965 (1975).

[51] E. Marinari, G. Parisi, and J. J. Ruiz-Lorenzo, Phys. Rev. B **58**, 14852 (1998).

[52] D. Iñiguez, G. Parisi, and J. J. Ruiz-Lorenzo, J. Phys. A **29**, 4337 (1996).

[53] R. N. Bahtt and A. P. Young, Phys. Rev. B **37**, 5606 (1998).

[54] M. Palassini and X. Caracciolo, Phys. Rev. Lett. **82**, 5128 (1999).

[55] B. A. Berg and W. Janke, Phys. Rev. Lett. **80**, 4771 (1998).

[56] N. Kawashima and A. P. Young, Phys. Rev. B **53**, R484 (1996).

[57] J. M. Luttinger, Phys. Rev. Lett. **37**, 778 (1976).

[58] M. Nielsen, D. H. Ryan, H. Guo, and M. Zuckermann, Phys. Rev. B **53**, 343 (1996).

[59] F. Matsubara, T. Tamiya, and T. Shirakura, Phys. Rev. Lett. **77**, 378 (1996).

[60] S. Bekhechi and B. W. Southern, Phys. Rev. B **70**, 020405 (2004).

[61] C. L. Chien *et al.*, J. Appl. Phys. **52**, 1750 (1981).

[62] H. Keller, K. V. Rao, P. G. Debrunner, and H. S. Chen, J. Appl. Phys. **52**, 1753 (1981).

[63] I. Mirebeau *et al.*, J. Magn. Magn. Mater. **54–57**, 99 (1986).

[64] J. A. Geohegan and S. M. Bhagat, J. Magn. Magn. Mater. **25**, 17 (1981).

[65] G. Aeppli *et al.*, J. Appl. Phys. **55**, 1628 (1984).

[66] K. Heinemann, C. Michaelsen, M. Fieber, and K. Baerner, J. Magn. Magn. Mater. **82**, 204 (1989).

[67] T. Miyazaki, I. Okamoto, Y. Ando, and M. Takahashi, J. Phys. F: Met. Phys. **18**, 1601 (1988).

[68] A. D. Beath and D. H. Ryan, J. Appl. Phys. **97**, 10A511 (2005).

[69] A. D. Beath and D. H. Ryan, J. Appl. Phys. **95**, 6980 (2004).

[70] A. Aharony, Phys. Rev. Lett. **34**, 590 (1975).

[71] S. Fishman and A. Aharony, Phys. Rev. B **19**, 3776 (1979).

[72] A. D. Beath and D. H. Ryan, J. Appl. Phys. **93**, 8188 (2003).

[73] A. B. Harris, J. Phys. C **7**, 1671 (1974).

[74] S. N. Kaul and P. D. Babu, Phys. Rev. B **45**, 295 (1991).

[75] K. Balakrishnan and S. N. Kaul, Phys. Rev. B **65**, 134412 (2002).

[76] P. D. Babu and S. N. Kaul, J. Phys.: Cond. Matter **9**, 7189 (1997).

[77] P. D. Babu and S. N. Kaul, Phys. Rev. B **52**, 10637 (1995).

[78] R. Reisser, M. Fähnle, and H. Kronmüller, J. Magn. Magn. Mater. **75**, 45 (1988).

[79] N. Goldenfeld, *Lecture Notes on phase transitions and the renormalization group* (Addison-Wesley, Reading, Mass, 1992).

[80] J. R. Thomson *et al.*, Phys. Rev. B **45**, 3129 (1992).

[81] F. Matsubara, T. Iyota, and S. Inawashiro, J. Phys. Soc. Jpn. **60**, 4022 (1991).

[82] K. Chen, A. M. Ferrenberg, and D. P. Landau, Phys. Rev. B **48**, 3249 (1993).

[83] C. Holm and W. Janke, Phys. Rev. B **48**, 936 (1993).

[84] A. G. Maddock, *Mössbauer spectroscopy: principles and applications* (Horwood Publications, Chichester, England, 1997).

[85] G. Schatz and A. Weidinger, *Nuclear condensed matter physics: Nuclear methods and applications* (John Wiley & Sons, New York, 1995).

[86] P. D. de Réotier and A. Yaouanc, J. Phys.: Cond. Matter **9**, 9113 (1997).

[87] D. H. Ryan, J. van Lierop, and J. M. Cadogan, J. Phys.: Cond. Matter **16**, S4619 (2004).

[88] A. Kuprin, D. Wiarda, and D. H. Ryan, Phys. Rev. B **61**, 1267 (2000).

[89] R. L. Mössbauer, Z. Phys. **151**, 124 (1958).

[90] B. Window, J. Phys. E: Sci. Instrum. **4**, 401 (1971).

[91] R. Kubo and T. Toyabe, in *Magnetic Resonance and Relaxation*, edited by R. Blinc (North-Holland, Amsterdam, 1967), p. 810.

[92] R. Kubo, Hyp. Int. **8**, 731 (1981).

[93] R. S. Hayano *et al.*, Phys. Rev. B **20**, 850 (1979).

[94] R. B. Stinchcombe, in *Phase Transitions and Critical Phenomenon, Vol. 7*, edited by C. Domb and M. S. Green (Academic Press, London, 1983).

[95] J. Brewer, private communication.

[96] D. P. Landau and K. Binder, *A Guide to Monte Carlo Simulations in Statistical Physics* (Cambridge University Press, Cambridge, 2000).

[97] *Topics in Applied Physics Vol. 71: The Monte Carlo Method in Condensed Matter Physics*, edited by K. Binder (Springer, New York, 1995).

[98] H. Müller-Krumbharr and K. Binder, J. Stat. Phys. **8**, 1 (1973).

[99] R. G. Brown and M. Ciftan, Phys. Rev. B **54**, 15860 (1996).

[100] M. Creutz, Phys. Rev. D **36**, 515 (1987).

[101] A. D. Beath and D. H. Ryan, J. Appl. Phys. **97**, 10A506 (2005).

[102] J. L. Alonso *et al.*, Phys. Rev. B **53**, 2537 (1996).

[103] A. D. Beath and D. H. Ryan, Phys. Rev. B **72**, 014455 (2005).

[104] A. D. Beath and D. H. Ryan, Phys. Rev. B **73**, 174416 (2006).

[105] A. D. Beath and D. H. Ryan, J. Appl. Phys. **101**, 09G102 (2007).

[106] D. Stauffer, *Introduction to Percolation Theory* (Taylor & Francis, London, 1985).

[107] G. Toulouse, Commun. Phys **2**, 115 (1977).

[108] E. Fradkin, B. A. Huberman, and S. H. Shenker, Phys. Rev. B **18**, 4789 (1978).

[109] A. D. Beath and D. H. Ryan, IEEE Trans. Mag. **43**, 2902 (2007).

[110] M. Nielsen, D. H. Ryan, H. Guo, and M. Zuckermann, Phys. Rev. B **53**, 343 (1996).

[111] A. Ghazali, P. Lallemand, and H. T. Diep, Physica A **134**, 628 (1986).

[112] J. R. Thomson *et al.*, Phys. Rev. B **45**, 3129 (1992).

[113] L. Neél, Ann. Phys. (Paris) **18**, 5 (1932).

[114] C. Wengel, C. L. Henley, and A. Zippelius, Phys. Rev. B **53**, 6543 (1996).

[115] M. Ahmadzadeh and A. Simpson, Phys. Rev. B **25**, 4633 (1982).

[116] A. A. Caprica, A. Bunker, and D. P. Landau, Phys. Rev. B **62**, 9458 (2000).

[117] M. Campostrini *et al.*, Phys. Rev. B **65**, 144520 (2002).

[118] J. M. Kosterlitz and D. J. Thouless, J. Phys. C: Solid State Phys. **6**, 1181 (1973).

[119] I. Campos *et al.*, Phys. Rev. Lett. **99**, 019702 (2007).